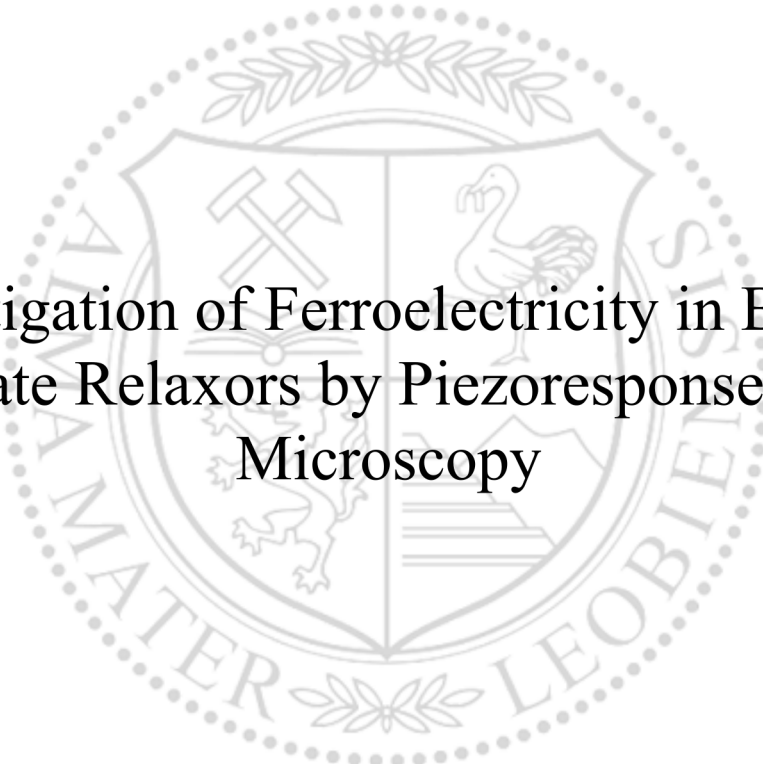




Chair of Physics

Master's Thesis



Investigation of Ferroelectricity in Barium
Titanate Relaxors by Piezoresponse Force
Microscopy

Philipp Münzer, BSc

August 2023



EIDESSTATTLICHE ERKLÄRUNG

Ich erkläre an Eides statt, dass ich diese Arbeit selbständig verfasst, andere als die angegebenen Quellen und Hilfsmittel nicht benutzt, und mich auch sonst keiner unerlaubten Hilfsmittel bedient habe.

Ich erkläre, dass ich die Richtlinien des Senats der Montanuniversität Leoben zu "Gute wissenschaftliche Praxis" gelesen, verstanden und befolgt habe.

Weiters erkläre ich, dass die elektronische und gedruckte Version der eingereichten wissenschaftlichen Abschlussarbeit formal und inhaltlich identisch sind.

Datum 25.08.2023

Unterschrift Verfasser/in
Philipp Münzer

Signiert von:	Philipp Münzer
Datum:	25.08.2023 19:07:01
<p>Dieses Dokument ist digital signiert! Dieses mit einer qualifizierten elektronischen Signatur versehene Dokument hat gemäß Art. 25 Abs. 2 der Verordnung (EU) Nr. 910/2014 vom 23. Juli 2014 ("eIDAS-VO") die gleiche Rechtswirkung wie ein handschriftlich unterschriebenes Dokument.</p>	
<small>Prüfinformation: Informationen zur Prüfung der elektronischen Signatur finden Sie unter www.a-trust.at/pdf</small>	

Acknowledgements

First, I want to thank my main supervisor Univ.-Prof. Dr. Christian Teichert for the excellent support throughout my thesis and for allowing me to freely pursue my work. Furthermore, I am thankful for his unconditional support in extracurricular activities which helped me to have a first glance into the scientific community. The next person who deserves my highest regard is my mentor and second supervisor Dr. Markus Kratzer. Thank you for your patience and open ear whenever I needed advice on the complex topic of Piezoresponse Force Microscopy. Moreover, I would like to thank my third supervisor, Priv.-Doz. Dr. Marco Deluca, for giving me the opportunity to do this work as part of his project: Polarization Decorrelation Regions in Perovskite Relaxors (POLDERS), with project number I4581-N and funded by the Austrian Science Fund (FWF). I am well aware of the leap of faith you gave me at the beginning of this work and I hope I was able to keep up with your expectations. In addition, I want to thank all members of the POLDERS project for integrating me so well into their team. The virtual as well as physical meetings with you were always fruitful, and they significantly strengthened my confidence in presenting and defending my work in front of a professional scientific community. I also want to thank all my colleagues from the Chair of Physics for the numerous, deeply scientific discussions we had together and for the possibility of using their high-end equipment for my measurements. What must not be left out, is the vast support from the Chair of Structural and Functional Ceramics, especially the aid from Univ.-Prof. Dr. Raúl Bermejo, DI Irina Kravela, and ao. Univ.-Prof. Dr. Peter Supancic. Their expertise in sample preparation, characterization and mechanics of technical ceramics was of essential value for the successful conduction of my thesis.

Next, I want to thank my parents, Andrea Zmugg and Josef Münzer, who supported me throughout my studies, financially and mentally. Without you, all this would not have been possible. I also want to acknowledge the support from my two siblings, Killian and Julia Münzer, who always had an open ear for my scientific excursions. I want to thank my long-time friend Michael Pölzl as well, for the advice he gave me on Python programming. There are two more members of my family, who invaluablely contributed to my personal development, my passed grandparents Aloisia and Johann Zmugg. Thank you for all the support, I miss you so dearly.

Finally, I want to thank my fiancée Tanja Fahler for her patience and warmth. Throughout my demanding studies, you always stood by my side, no matter the turbulence. I love and admire you for that and I will never forget it.

Abstract

Substituted barium titanate counts among the best-performing lead-free perovskite relaxor ferroelectric materials. It is suitable for application as actuators, sensors, and electrical energy storage systems in microelectronics due to its thermal stability, high permittivity, and low coercivity. One way to induce relaxor ferroelectric (short: relaxor) behaviour is replacing the central B-site Ti^{4+} ion with foreign ions like Zr^{4+} (homovalent), Nb^{5+} (heterovalent), or simultaneous substitution of both species (co-substitution). Homovalent substituents impede a collective displacement of the O–Ti–O chains via the introduction of random elastic fields, whereas in heterovalent substitution a perturbation is caused by random electric fields as a consequence of local charge imbalance. Even though relaxors have been investigated for more than half a century, numerous fundamental questions about their unique behaviour among dielectrics remain unanswered. This master’s thesis comprehensively investigates the influence of homovalent, heterovalent, and co-substitution on the ferroelectric properties of polycrystalline barium titanate. A suitable tool for this investigation is Piezoresponse Force Microscopy (PFM), a special mode conducted by an Atomic Force Microscope. Single Frequency PFM enables the mapping of the ferroelectric domain structure, which can be used to infer the effectiveness of substituents in perturbing the long-range correlation between the polarization vectors in the material. In addition, local poling experiments, where a bias is applied to the conductive tip of the Atomic Force Microscope, can be conducted to probe the ferroelectric switchability of the material and the long-term stability of newly formed domains. An even more sophisticated method, Switching Spectroscopy PFM, gives insight into the local polarization switching dynamics in the zone underneath the conductive tip, for the active-field and field-free case. Multiple measurements of this type within a defined temperature interval, combined with a semi-automated algorithm for correction, cleaning, and evaluating the generated data, provide information about the temperature-dependent local polarization switching dynamics in ferroelectrics and relaxors. The results reveal that co-substitution is most effective in disrupting ferroelectric long-range order, followed by heterovalent Nb^{5+} substitution and Zr^{4+} substitution as the least effective means. The transition from ferroelectric to relaxor behaviour occurs between 20%–30% homovalent Zr substitution. In the heterovalent case, a Nb concentration between 5%–7% is already sufficient to cause the same effect. In the case of co-substitution, a concentration of 2.5% Nb and 20% is sufficient to effectively disrupt any ferroelectric long-range order. In general, the measurements imply that even though the highest substituted systems can be considered as being in the fully disordered relaxor state with ergodic polar nanodomains, traces of classical ferroelectric behaviour in the form of hysteresis loops recorded by PFM can still be obtained. Furthermore, charge-balancing vacancies significantly influence image acquisition by PFM in systems with heterovalent substitution, leading to non-negligible, non-piezoelectric signal contributions and even material swelling on the surface upon poling. This thesis corroborates that PFM is an effective method for determining the ferroelectric properties of relaxors, provided that it is complemented by additional experimental methods like Raman/dielectric spectroscopy, X-ray diffraction or electric Polarisation-Field loop measurements.

Kurzfassung

Aufgrund seiner thermischen Stabilität, hohen Permittivität, sowie niedrigen Koerzitivität zählt substituiertes Bariumtitanat zu den vielversprechendsten bleifreien Relaxorferroelektrika auf Perovskitbasis. Es findet Anwendung in Aktoren, Sensoren und elektrischen Energiespeichern in der Mikroelektronik. Der Austausch des zentralen Ti^{4+} Ions durch Fremdionen wie Zr^{4+} (homovalent), Nb^{5+} (heterovalent), oder simultanes Einbringen beider Spezies, stellt eine Möglichkeit dar um Relaxorferroelektrisches (kurz: Relaxor) Verhalten hervorzubringen. Homovalente Substitution erschwert die kollektive Verschiebung der O–Ti–O Ketten durch die Einbringung von zufallsverteilten elastischen Feldern, wohingegen in der heterovalenten Substitution diese Störung durch zufallsverteilte elektrischen Felder, eine Konsequenz von einem lokalen Ungleichgewicht elektrischer Ladungen, verursacht wird. Obwohl Relaxoren seit mehr als einem halben Jahrhundert untersucht werden, bleiben noch viele fundamentale Fragen über ihr einzigartiges Verhalten unter den Dielektrika offen. Unter Zuhilfenahme von Piezoresponse Force Microscopy (PFM), einer speziellen Methode eines Rasterkraftmikroskops, widmet sich diese Masterarbeit der umfassenden Untersuchung von homovalenten, heterovalenten, und simultan substituiertem polykristallinen Bariumtitanat sowie die Einflüsse der Substituenten auf die ferroelektrischen Eigenschaften. Single Frequency PFM ermöglicht die Abbildung der ferroelektrischen Domänenstruktur, über die man auf die Wirksamkeit der Substituenten bei der Störung weitreichender Korrelationen zwischen den Polarisationsvektoren im Material schließen kann. Zusätzlich kann die lokale Schaltbarkeit und langfristige Stabilität neugeformter Domänen im Material durch das Anlegen einer Spannung an der leitfähigen Spitze des Rasterkraftmikroskops festgestellt werden. Eine noch anspruchsvollere Methode, Switching Spectroscopy PFM, gewährt Einblick in die Dynamik der Polarisationsumkehrung in der Zone unterhalb der Spitze für den feldaktiven und feldfreien Fall. Zahlreiche Messungen dieser Art innerhalb eines definierten Temperaturintervalls, kombiniert mit einem halbautomatischen Algorithmus zur Korrektur, Selektion und Auswertung der generierten Daten, liefern Informationen über die lokale temperaturabhängige Dynamik der Polarisationsumkehrung in Ferroelektrika und Relaxoren. Die Ergebnisse dieser Messungen zeigen, dass simultane Substitution am wirksamsten ist, gefolgt von der heterovalenten Nb^{5+} Substitution und Zr^{4+} Substitution als die am wenigsten wirksame Variante. Der Übergang von klassischem ferroelektrischen Verhalten zu Relaxorverhalten setzt im Intervall zwischen 20% und 30% homovalenter Zr Substitution ein. Im heterovalenten Fall genügt bereits eine Nb Konzentration zwischen 5% und 7% um dieselbe Wirkung zu erzielen. Wenn simultan substituiert wird, reicht bereits eine Konzentration von 2,5% Nb und 20% Zr aus, um die langreichweitige ferroelektrische Ordnung zu unterdrücken. Obwohl im generellen jene Systeme mit dem höchsten Grad an Substitution als völlig ungeordnete Relaxoren mit ergodischen polaren Nanodomänen angesehen werden können, ist es trotzdem noch möglich Spuren von klassischem ferroelektrischen Verhalten in der Form von Hystereseschleifen in PFM zu messen. Des Weiteren beeinflussen Leerstellen zur Ladungsbilanzierung die PFM-Messungen wesentlich und können sogar zum irreversiblen Anschwellen des Materials beim Polen führen. Diese Masterarbeit belegt, dass PFM eine effektive Methode zur Feststellung der ferroelektrischen Eigenschaften in Relaxoren ist, vorausgesetzt dass sie mit komplementären Messmethoden, wie z.B. Raman/dielektrische Spektroskopie, Röntgendiffraktion oder elektrische Polarisations-Feld Schleifenmessungen, kombiniert wird.

List of abbreviations

2D	Two-Dimensional
3D	Three-Dimensional
AC	Alternating Current
AD	Amplitude Distribution
AFM	Atomic Force Microscope
AmpOff	Remanent Piezoresponse
AmpOn	Active-field Piezoresponse
BT	Barium Titanate
BZT	Barium Zirconium Titanate
BNT	Barium Niobium Titanate
BNZT	Barium Niobium Zirconium Titanate
C-AFM	Conductive Atomic Force Microscopy
DART	Dual AC Resonance-Tracking
DC	Direct Current
DPT	Diffuse Phase Transition
EESS	Electrical Energy Storage Systems
ER	Ergodic Relaxor
ESM	Electrochemical Strain Microscopy
FE	Ferroelectric
InvOLS	Inverse Optical Lever Sensitivity
LIA	Lock-In Amplifier
OM	Optical Microscopy
NR	Nonergodic Relaxor
PD	Phase Distribution
PE	Paraelectric
P-E	Polarisation-Field
PFM	Piezoresponse Force Microscopy
PNR	Polar Nanoregion
PT	Phase Transition
PZT	Lead Zirconate Titanate
RD	Response Distribution
RF	Relaxor Ferroelectric
RT	Room Temperature
SF-PFM	Single Frequency Piezoresponse Force Microscopy
SS-PFM	Switching Spectroscopy Piezoresponse Force Microscopy
XRD	X-Ray Diffraction

Contents

1	Introduction	1
2	Theoretical background	3
2.1	Electroelasticity	3
2.1.1	(Inverse) Piezoelectric effect	3
2.1.2	Electrostriction	4
2.1.3	Pyroelectricity	5
2.1.4	Flexoelectricity	5
2.2	(Multi-) Ferroic materials	6
2.2.1	Ferroelectricity	6
2.2.2	Ferroelasticity	8
2.2.3	Relaxor-Ferroelectricity	8
2.3	The $\text{BaZr}_x\text{Nb}_y\text{Ti}_{1-x-5y/4}\text{O}_3$ system	9
2.3.1	Barium titanate: The model FE material	9
2.3.2	Zr/Nb substituted barium titanate	11
2.4	Piezoresponse Force Microscopy	13
2.4.1	Contrast formation in PFM	13
2.4.2	Single Frequency PFM	14
2.4.3	Dual AC Resonance Tracking	15
2.4.4	Local polarization switching with an AFM	15
2.4.5	Switching Spectroscopy PFM	16
3	Experimental methods and data evaluation	18
3.1	Sample synthesis	18
3.2	Sample preparation	18
3.3	Optical microscopy (OM) inspection	19
3.4	PFM measurements	20
3.4.1	Imaging spontaneous polarization with PFM	20
3.4.2	Local polarization switching by applying a DC-bias to the tip	21
3.4.3	Probing the local switching dynamics utilizing SS-PFM	21
3.5	Data evaluation	21
3.5.1	SF-PFM evaluation	21
3.5.2	SS-PFM evaluation	23
4	Results and discussion	28
4.1	BT-System	28
4.1.1	Microstructure	28
4.1.2	Domain structure	28
4.1.3	Polarization switching	32
4.1.4	SS-PFM	33
4.2	BZT-System	35
4.2.1	Microstructure	35

4.2.2	Domain structure	36
4.2.3	Polarization switching	43
4.2.4	SS-PFM	47
4.3	BNT-System	49
4.3.1	Microstructure	49
4.3.2	Domain structure	49
4.3.3	Polarization switching	55
4.3.4	SS-PFM	60
4.4	BNZT-System	63
4.4.1	Microstructure	63
4.4.2	Domain structure	64
4.4.3	Polarization switching	69
4.4.4	SS-PFM	73
4.5	Conclusions derived from the measurements	75
5	Summary and outlook	79
	References	81

1 Introduction

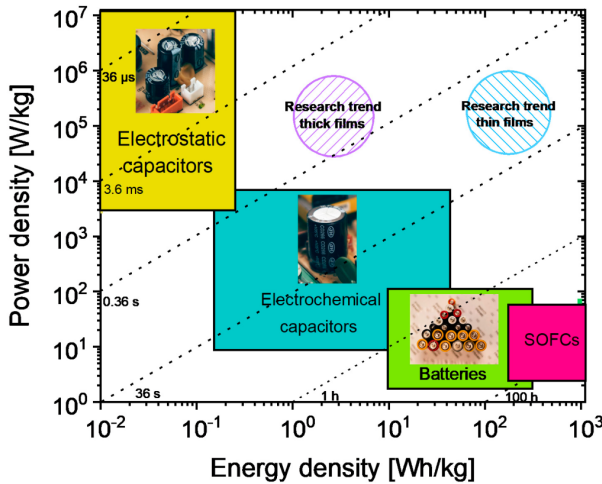


Figure 1.1: Ragoneplot of power and energy density covering different electrical energy storage systems (Figure taken from [1]; License: Creative Commons Attribution 4.0 International).

With the ongoing implementation of integrated microelectronics in almost all branches of industry and society, unprecedented demand for sustainable and long-life electrical energy storage systems (EESS) arises [2]. Apart from well-known EESS like batteries, which can store high amounts of energy, low energy density systems like capacitors are crucial elements in most microelectronic systems due to their extraordinary power density [3]. The Ragone plot [4] displayed in figure 1.1 reveals a general trend that holds for all established EESS: There is always a trade-off between high power density and high energy density, and these limitations arise from physical principles. For example, batteries rank among the EESS with the highest energy density, but due to their charge storage mechanism, which is electrochemical, they are limited in their power density. Electrostatic capacitors, on the other hand, rank among the EESS with the highest power density owing it to their exclusive electrostatic charge storage mechanism. However, the total storable electrical energy is lower by at least several orders of magnitude compared to batteries and electrochemical capacitors. At first glance, this suggests that electrostatic capacitors are inferior candidates for EESS. However, this alleged drawback can be neglected when considering their high operating voltages, high thermal stability, lower fabrication cost, long cyclic lifetime, and high tunability with respect to operating temperature [5]. Currently, research on dielectrics focuses on the development of novel sustainable dielectric materials with the aforementioned properties and significantly higher energy densities in addition, ideally leading to the emergence of a new generation of high power/energy density EESS.

The established materials for electrostatic capacitors are linear dielectrics, ferroelectrics (FE), and relaxor ferroelectrics (RF). The latter two are a core part of this thesis and will be explained in more detail in the upcoming chapters. The decisive performance parameters for dielectrics are high permittivity, high saturation polarization, low remanent polarization and high breakdown strength, which are corresponding to high polarizability, high charge storage, low energy losses, and high operating voltages, respectively. Linear dielectrics (cf. figure 1.2) exhibit negligible energy losses but also low permittivity, thus limiting their capability as high-performance EESS [6]. FEs, on the other hand, exhibit an exceptionally high permittivity originating from their inherent spontaneous and reversible polarization. However, energy losses can be considerably high due to the motion of FE domain walls and their interactions with defects in the material [7]. The third material class, RFs, can be considered as a means of overcoming the drawbacks that the latter two classes exhibit. RFs are FEs with a disturbed domain structure as a consequence of the introduction

of foreign atoms in the system. This leads to low losses while maintaining high permittivity, making them the material of choice for most high energy density electrostatic capacitors [8, 9].

The major drawback of these materials is that most RF systems in use are lead-based [10], which could pose a threat to the environment and health of individuals. In particular, extraction, processing, and disposal are possible sources of lead contamination [11]. Consequently, contemporary research on novel RF materials is focused on cost-effective and lead-free alternatives. Among the most promising candidates for lead-free RFs are systems based on substituted barium titanate [1]. The introduced foreign atoms can either be of same (homovalent substitution) or different valency (heterovalent substitution). The FWF-Project "Polarization Decorrelation Regions in Perovskite Relaxors" (project number: I4581-N), short: POLDERS, of Dr. Marco Deluca investigates the synthesis, modelling and characterization of lead-free barium titanate RFs, with Zr and Nb as substituent atoms. Besides the well-understood dielectric and FE properties on the macroscale, obtained via Polarisation-Field (P-E) loop measurements [12], the arrangement of FE domains on the micro- and nanoscale still remains an open question to be investigated in these systems.

A reliable method for measuring FE domains at the nanoscale is Piezoresponse Force Microscopy (PFM), a special operating mode in an Atomic Force Microscope (AFM) that examines the local electromechanical coupling between a sharp tip and a surface, revealing the FE structure of a material. This thesis focuses on the investigation of ferroelectricity in homovalent, heterovalent, and co-substituted lead-free barium titanate RFs, ranging from low to high substitution amounts. The thesis will address the following three questions, which can all be answered by the careful conduction of sophisticated PFM experiments:

1. Do the systems exhibit a spontaneous polarization which can be probed by PFM?
2. Is the polarization reversible and stable?
3. How do the dynamics of the polarization switching process behave locally on the nanoscale?

This thesis will attempt to deliver a consistent and comprehensive picture of ferroelectricity in these systems by comparing the results to other experimental data and results from computational modelling. In addition, recommendations for improvements of experiments of similar type in this field will be provided.

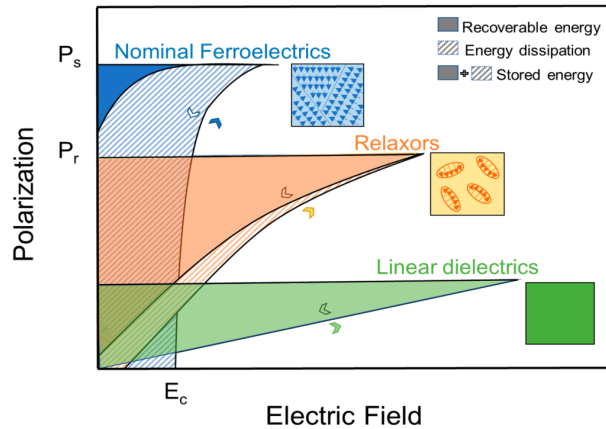


Figure 1.2: Polarization versus electric field for FEs, RFs and linear dielectrics (Figure taken from [1]; License: Creative Commons Attribution 4.0 International).

2 Theoretical background

2.1 Electroelasticity

Electroelasticity describes the link between an electric field and mechanical deformation in matter, also known as electromechanical coupling [13]. Electroelastic materials are broadly utilized in microelectronic devices as actuators, transducers, resonators, and acoustic wave sensors. In general, all dielectrics exhibit at least the most primitive electroelastic interaction, namely electrostriction. With decreasing crystal symmetry, more complex effects like piezoelectricity, pyroelectricity or even ferroelectricity may occur.

2.1.1 (Inverse) Piezoelectric effect

The term piezoelectricity describes the linear relation between mechanical deformation and electric polarization. It was discovered by the Curie brothers in 1880 on Quartz and Rochelle [14]. The possible emergence of piezoelectricity is restricted to 20 of the 32 crystallographic point groups, which do not possess a centre of symmetry, or in other words, which do not exhibit inversion symmetry [15]. It must be highlighted, that the absence of a centre of symmetry does not automatically entail a polar axis in the crystal, which gives rise to additional effects like pyroelectricity.

The direct piezoelectric effect describes the occurrence of electric polarization by the application of mechanical stress or strain in a crystal and is computed by the following four tensor equations:

$$D_i = d_{ikl} T_{kl} + \epsilon_{ik}^T E_k \quad \text{or} \quad D_i = e_{ijk} S_{jk} + \epsilon_{ij}^S E_j \quad (2.1)$$

$$E_i = -g_{ikl} T_{kl} + \beta_{ik}^T D_k \quad \text{or} \quad E_i = -h_{ikl} S_{kl} + \beta_{ik}^S D_k. \quad (2.2)$$

The equations can be interpreted as the cause of an electric field or dielectric displacement induced by mechanical stress or strain, respectively. Due to symmetry considerations, the converse mechanism must occur in piezoelectrics as well, known as the inverse piezoelectric effect. It was predicted by Lippmann and experimentally approved by the Curie brothers in 1881 [16, 17]. Equivalent to the direct effect, it can be computed by four related tensor equations:

$$T_{ij} = c_{ijkl}^D S_{kl} - h_{kij} D_k \quad \text{or} \quad T_{ij} = c_{ijkl}^E S_{kl} + e_{kij} E_k \quad (2.3)$$

$$S_{ij} = s_{ijkl}^D T_{kl} + g_{kij} D_k \quad \text{or} \quad S_{ij} = s_{ijkl}^E T_{kl} + d_{kij} E_k. \quad (2.4)$$

Similar to their direct counterparts, these equations can be interpreted as the cause of mechanical strain or stress induced by an electric field or dielectric displacement, respectively. The dielectric displacement \mathbf{D} and electric field \mathbf{E} are tensors of rank 1, also known as 3-dimensional vectors. The dielectric permittivity ϵ and impermeability β as well as the mechanical stress \mathbf{T} and strain \mathbf{S} are tensors of rank 2 but can be reduced to a vector with 6 dimensions due to symmetry. The piezoelectric coefficients \mathbf{d} , \mathbf{e} , \mathbf{g} and \mathbf{h} are tensors of rank 3 and can also be reduced to a 6 x 3 or 3 x 6 matrix, respectively. Finally, the two rank 4 tensors, which are the elastic modulus \mathbf{c} and elastic compliance \mathbf{s} can be reduced to a 6 x 6 matrix [13]. In figure 2.1, the connections between

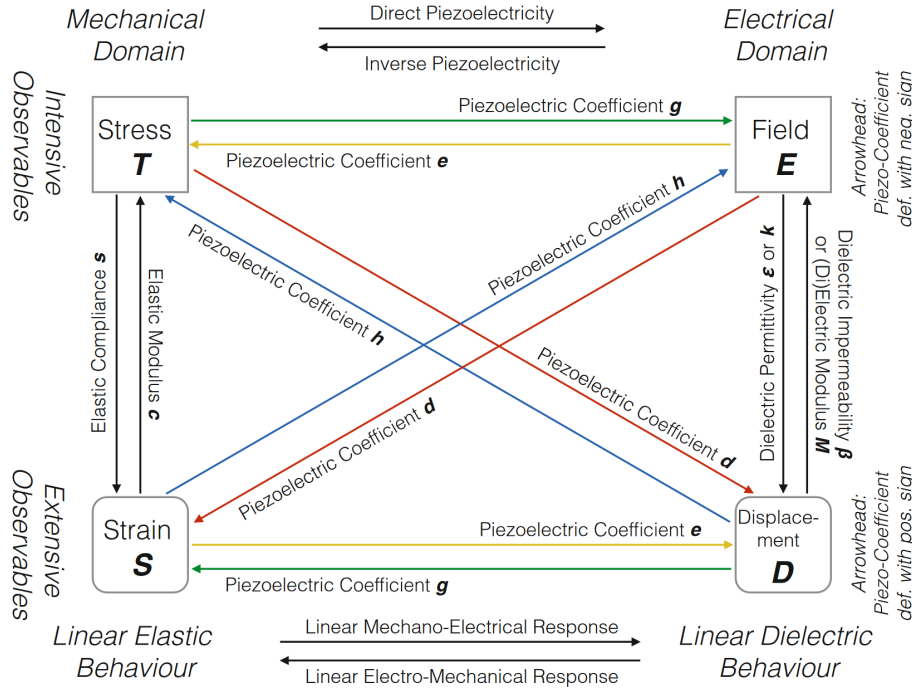


Figure 2.1: Relations between stress, strain, electric field, and dielectric displacement in linear electroelasticity (Figure taken from [18]).

the electrical and mechanical domains in piezoelectricity are summarized graphically. Typical materials which exhibit piezoelectricity are quartz, BaTiO_3 , ZnO and even some polymers or collagen [18]. The magnitude of the inverse piezoelectric effect can be as high as $6 \cdot 10^{-10} \text{m/V}$ for some materials such as lead zirconate titanate (PZT) [19].

2.1.2 Electrostriction

In contrast to piezoelectricity, electrostriction is observed in all dielectrics, even in those with inversion centres. This nonlinear electromechanical coupling effect can be measured as an induced strain caused by an unipolar electric field in a material [19, 20]. The magnitude is dependent on the square of the electric field or polarization and can be computed by the following tensor equation:

$$S_{ij} = M_{ijkl} E_k E_l = Q_{ijkl} P_k P_l. \quad (2.5)$$

The equation can be read as the strain \mathbf{S} caused by the square of the electric field \mathbf{E} or polarization \mathbf{P} , respectively. \mathbf{M} and \mathbf{Q} are the electrostriction tensors with rank 4 and can be converted via the field-polarization relationships in linear dielectrics [21]. However, in many FEs and RFs, electrostriction is not a function of the squared electric field due to the saturation of polarization and strain. Hence, it is often feasible to use the polarization definition, which is correct even in the saturation regime. Electrostrictive materials find application as active optic systems for the attenuation of vibrations and atmospheric turbulence. Typical values for \mathbf{Q} range from $10^{-2} \text{m}^4/\text{C}^2$ for RFs to $10^6 \text{m}^4/\text{C}^2$ for soft polymers [22].

An inverse effect like in piezoelectricity is not possible, since stress creates a bipolar axis and cannot induce an electric dipole moment in centrosymmetric crystals [15]. However, there is a related effect known as dielectrostriction, which is the dependence of the permittivity on strain or stress. At optical frequencies, this effect is also known as birefringence [18].

2.1.3 Pyroelectricity

As already mentioned in section 2.1.1, pyroelectricity requires a nonvanishing polarization (i.e. a polar axis) at zero stress and strain in the crystal [15]. This condition is fulfilled for 10 of the 20 crystallographic point groups which also exhibit piezoelectricity [22]. Pyroelectricity is the change of polarization due to a homogeneous temperature change in the material. An ideally electrically insulated pyroelectric will accumulate surface charges when heated or cooled, which decay approximately within the timeframe of the electrical time constant of the material [23].

Mathematically, it can be described by the following equation for the zero electric field case:

$$P_i = D_i = p_i \delta T \quad (2.6)$$

with \mathbf{P}_i and \mathbf{D}_i being the change of polarization or dielectric displacement due to a change in temperature δT . p_i is a polar tensor of rank 1. Depending on how the pyroelectric coefficients are measured, a distinction must be made between the primary and secondary pyroelectric effect, which excludes or includes the contribution of thermal expansion. The pyroelectric coefficient is temperature-dependent and significantly decreases towards lower temperatures due to a drastic decrease in thermal motion. The highest values can be obtained near the Curie temperature due to the rapid change of polarization arising from the ferroelectric-paraelectric phase transition (cf. section 2.2.1). Typical values for the pyroelectric coefficient range from $-268 \mu\text{C}/\text{m}^2\text{K}$ in PZT to $+86.3 \mu\text{C}/\text{m}^2\text{K}$ in $\text{Li}_2\text{SO}_4 \cdot 2\text{H}_2\text{O}$ at room temperature (RT). Pyroelectric materials are used as sensors in burglar alarms, fire detectors and infrared systems [22].

2.1.4 Flexoelectricity

The flexoelectric effect is a higher-order linear electromechanical phenomenon, which can, in contrast to piezoelectricity, occur even in materials exhibiting centrosymmetry. When a centrosymmetric structure like the one shown in figure 2.2 is exposed to a strain gradient such as bending strain, an electric dipole moment occurs due to local symmetry breaking in the crystal. This relation between strain gradient and polarization is linear and therefore the inverse effect must also exist, known as the converse flexoelectric effect, which describes the linear strain response to a polarisation gradient. The flexoelectric effect can be described by the following tensor equation:

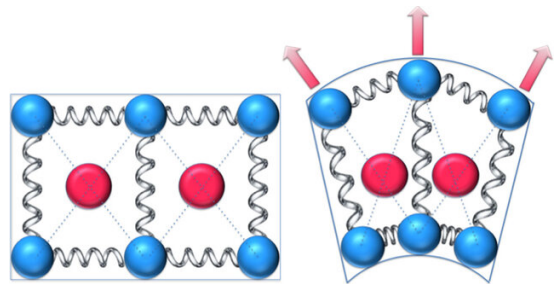


Figure 2.2: Figure of the general principle of flexoelectricity. A centrosymmetric crystal exhibits polarization when exposed to a strain gradient (Figure taken from [24]).

$$P_i = \chi_{ij} E_j + e_{ijk} S_{jk} + u_{klj} \frac{\partial S_{kl}}{\partial x_j}. \quad (2.7)$$

The first two terms in equation 2.7 represent the dielectric and piezoelectric response (note that the dielectric permeability tensor ϵ was replaced by the dielectric susceptibility tensor χ to directly yield the polarization) and the third term describes the flexoelectric effect with the spatial derivative of the strain $\partial \mathbf{S} / \partial \mathbf{x}$ and the fourth rank flexoelectric tensor \mathbf{u} . Flexoelectricity can strongly influence the behaviour of domain walls of FEs [25].

2.2 (Multi-) Ferroic materials

Ferroic materials share the characteristic that they exhibit intrinsic long-range ordering of at least one physical property like magnetization, polarization, or mechanical strain. The extent of this ordering is usually several orders of magnitude larger than the scales of their irreducible representation, e.g. the electric dipoles of individual unit cells can exhibit ordering along several microns in an FE crystal. The spatial extent of this ordering is usually limited by the excess energy that arises from it. As a consequence, the material arranges in regions of alternating orientation of the ordered property, known as domains, to reduce excess energy from the ordering. The interface that separates adjacent domains is called a domain wall. The size of the domains is determined by the energy that arises from the creation of the domain walls as well as the energy arising from the ordering in the bulk. The domain size that yields the lowest energy determines the equilibrium configuration. By far the most characteristic

feature of ferroics is their hysteric behaviour of the ordered property when exposed to an alternating field that can interact with it. Figure 2.3 displays the general shape of a hysteresis loop, albeit the shape can be greatly influenced by several properties like the kind of order or microstructure. Typical examples of ferroic effects are ferromagnetism, ferroelectricity and ferroelasticity [26]. If materials simultaneously exhibit more than one ferroic effect, they are called multiferroics, e.g. magnetoelectric materials, which exhibit FE and ferromagnetic behaviour [27].

2.2.1 Ferroelectricity

In crystalline solids, ferroelectric materials can be classified as a subgroup of pyroelectrics. They contain a non-vanishing polarization in the absence of an electric field (i.e. spontaneous polarization), and the individual electric dipoles exhibit order far beyond their unit cell, i.e. they form domains of equal polarization orientation. The domains themselves arrange in antiparallel polarization to reduce the electrostatic energy. The polarization is locally or globally reversible by the application of an electric field, also known as poling. This mechanism is possible because an FE's polar structure can be viewed as a slightly distorted nonpolar structure [28]. Apart from this functional definition, a structural definition exists as well (similar to pyroelectrics), which is derived from the relation of two symmetries: An FE exhibits a structural phase transition from a high-symmetry phase, also called the parent or simply paraelectric (PE) phase, into a lower symmetry phase (or polar phase). In the polar phase, the pyroelectric coefficient vector attains new nonzero components which were zero in the parent phase. In other words, the polar phase acquires the new vector components by the loss of symmetry operations which were present in the parent phase. For example, the central ion of the cubic perovskite FE PbTiO_3 is displaced from its centre position when it undergoes the phase transition, which results in a tetragonal distortion and consequently, the loss of inversion symmetry of the cubic parent phase, giving rise to ferroelectricity [29].

The temperature of the PE-FE phase transition is known as the Curie temperature T_C . At T_C ,

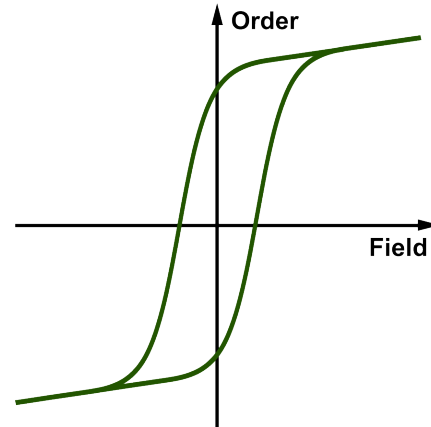


Figure 2.3: Hysteresis loop behaviour in ferroic materials. The materials exhibit a coercive field and saturation of order in the high-field regime. The shape can vary significantly for different materials and ferroic effects.

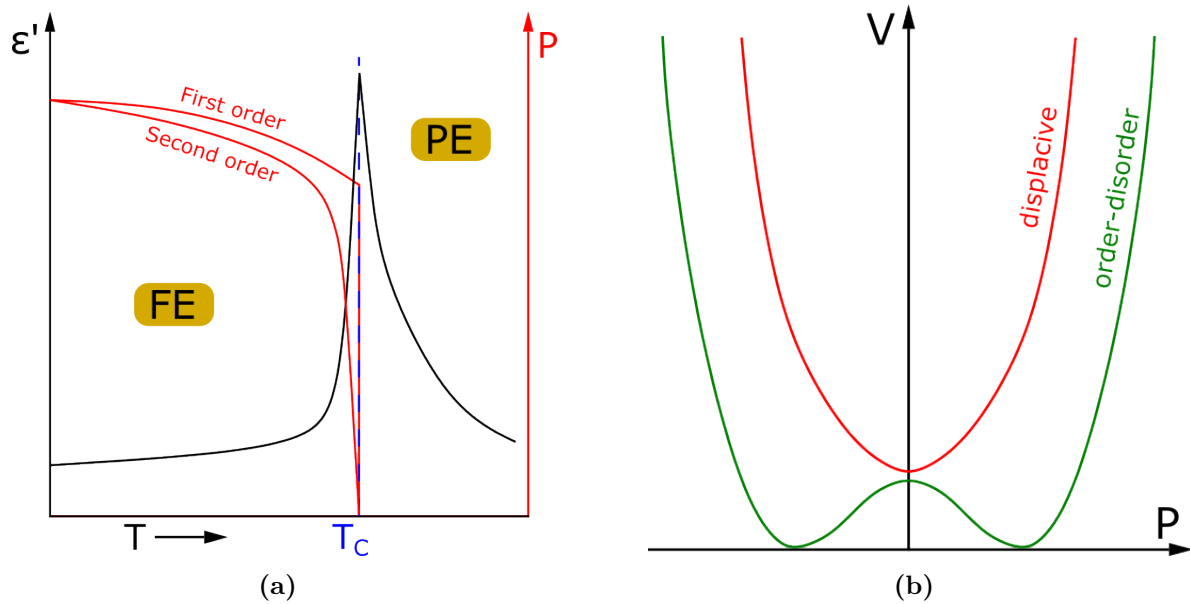


Figure 2.4: Temperature-dependent permittivity and polarization of FEs in the vicinity of the Curie temperature (a) and polarization-dependent potential above T_C of an FE with order-disorder or displacive phase transition (b).

the FE exhibits a sharp peak in its dielectric permittivity, which is illustrated in figure 2.4a. The phase transition can be first- or second-order, with a sharp drop or diffuse declination of the polarization in the vicinity of T_C . The mechanism of the phase transition can be either of displacive or order-disorder type (cf. figure 2.4b). In the former type, the electric dipoles vanish above T_C ; in the latter type, the electric dipoles remain but they lose their orientation order and macroscopically cancel each other out. In reality, the actual mechanism is a mixture of both cases [26]. The behaviour discussed above implies that any forced polarization in an FE can be "erased" by heating above T_C and subsequent cooling, which must be taken into account when designing an FE for the operation in the high-temperature range.

The mutual arrangement of domains and their domain walls have a significant influence on the mechanical, electrical, and electromechanical behaviour of an FE. The pattern and size of domains are dependent on the crystal size in polycrystalline FEs and can be classified into three sections separated by two critical grain size values g_1 and g_2 , as illustrated in figure 2.5. If the grain size is above g_2 , a complex, multi-domain herringbone structure is observed, where the domain width depends on the cube root of the grain size. Between g_1 and g_2 , the pattern reduces to a simpler lamellar domain structure of alternating 180° or 90° domains. The width of these domains is dependent on the square root of the grain size. If the grain size is below g_1 , the crystals exhibit single-domain polarization. For

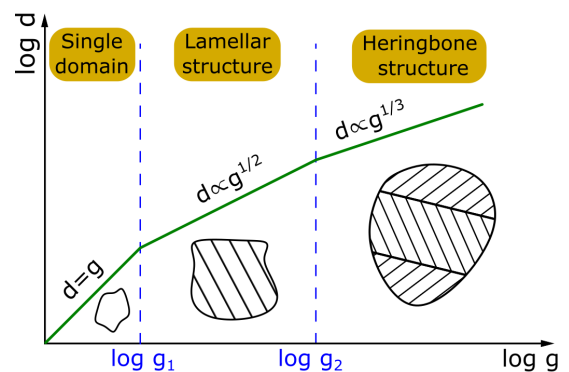


Figure 2.5: Relation between grain size g and domain width d in FEs. The characteristic grain sizes g_1 and g_2 mark the transition from single domain crystals to lamellar structure and finally to herringbone structure.

BaTiO₃, typical values for \mathbf{g}_1 and \mathbf{g}_2 are 40 nm and 4.7 μm , respectively. Formally defined, an FE domain wall is the quasi-2D interface between adjacent domains of different polarization orientations. They exhibit enhanced or reduced conductivity compared to the bulk and strongly interact with defects in the crystal. The poling behaviour of FEs can be greatly influenced by the introduction or removal of defects in the crystal, since domain wall movement is a major mechanism in domain switching, besides domain nucleation. Domain wall widths ranging between 1 nm and 6 nm were reported by TEM studies in several FE materials [30, 31].

FE effects can arise from several crystal structure groups like the tungsten-bronze, pyrochlore, or bismuth layer-structure group, but by far the most important is the oxygen octahedral group. BT, PZT and their derivatives are also members of this group and find broad application as transducers, capacitors, and electrooptics [2].

2.2.2 Ferroelasticity

Ferroelasticity was long believed to be a side effect of ferroelectricity or ferromagnetism. However, this effect can also exist on its own, e.g. in the form of martensitic phase transitions. In ferroelastics, a spontaneous strain occurs when the material has undergone a phase transition and a stress-strain hysteresis can be obtained [26]. If an FE is also ferroelastic, the polarization can be switched by both the electric field and the mechanical stress, because the polarization and distortion are inherently linked. As a consequence of stress release, FEs which exhibit ferroelasticity form a domain pattern of antiparallel (180°) and 71°, 90°, or 109° domains (depending on the crystal structure). The former type reduces the energy arising from the electric field and the latter the energy arising from mechanical stress [30].

2.2.3 Relaxor-Ferroelectricity

Relaxor ferroelectrics, or short relaxors, is a material class which has been investigated for more than half a century but is not fully understood yet. The partial substitution of ionic sites with foreign atoms in an FE causes a disturbance in FE order. In lower substituted systems, the temperature-dependent permittivity exhibits a diffuse peak instead of a sharp one, thus they are called FE with a diffuse phase transition (DPT) [32]. In these systems, long-range FE order is still preserved. Upon higher substitution, the long-range FE order completely vanishes, and the system is in the full RF state. The substitute atoms can be of the same or different valency, resulting in a fragmented or disordered RF, respectively [1]. The elemental disorder in fragmented RFs leads to local breaking off of the collective ionic displacements, whereas in disordered RFs, random electric fields arising from local charge imbalance is the major cause for RF behaviour [1, 33]. Even though RFs appear to be fully disordered, their permittivity maximum remains sufficiently high for their application as electrostatic capacitor materials. This high permittivity is attributed to the local formation of clusters of the same chemistry which exhibit ferroelectricity. Such a cluster is often called a polar nanoregion (PNR) [34]. However, the true nature of PNRs is still actively discussed and not fully understood to this day [35]. Besides their slightly lower permittivity, energy dissipation is remarkably lower compared to FEs, due to their unstable, but highly polarizable PNRs. This is confirmed by their slim hysteresis loops as well (cf. figure 1.2).

RFs exhibit some unique properties among dielectrics. First, their temperature-dependent permittivity exhibits a frequency dispersion [36]. Higher frequencies of the stimulating electric

field shift the real part of the complex permittivity maximum towards higher temperatures and lower peak values (cf. figure 2.6a). RFs exhibit different phases depending on their temperature, which is displayed in figure 2.6b (red line). The PE phase occurs at high temperatures, where the permittivity follows the Curie-Weiss law: $\epsilon' = C/(T - T_C)$, thus behaving similarly to the PE phase of FEs. If the RF is cooled down below the Burns temperature T_B , it transforms into an ergodic relaxor (ER) with randomly distributed dynamic PNRs. Even though this is not considered a structural phase transition, the behaviour still changes significantly compared to the PE phase. Here, the permittivity can be described by a Lorenz-type relation. Upon further cooling, the permittivity rises until it reaches its (frequency-dependent) peak at T_m . Simultaneously, the PNRs become less dynamic until they eventually become static at T_f , commonly known as the freezing temperature. Below this temperature, the system is considered a nonergodic relaxor (NR). Some systems even exhibit a relaxor-to-ferroelectric phase transition at their Curie temperature T_C , as illustrated by the sharp drop (green line) in figure 2.6b. If a sufficiently high electric field is applied to an NR, it can be irreversibly transformed into the FE state [37].

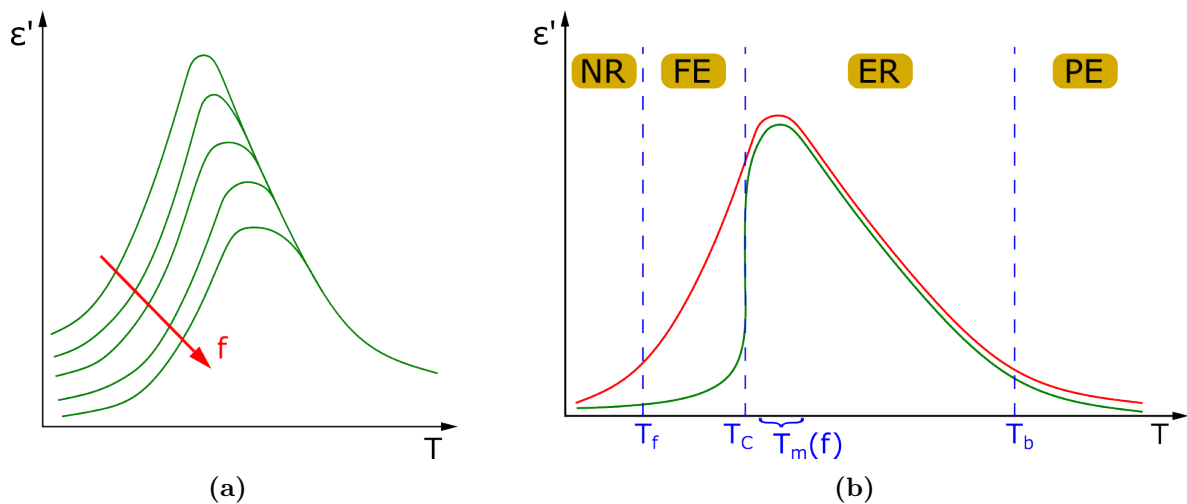


Figure 2.6: Frequency-dependent permittivity of an RF (a) and temperature-dependent evolution of the permittivity showing the different phases of an RF (b). The red line represents an RF with PNRs that freeze below T_f and the green line an RF with an FE phase transition below T_C .

2.3 The $\text{BaZr}_x\text{Nb}_y\text{Ti}_{1-x-5y/4}\text{O}_3$ system

2.3.1 Barium titanate: The model FE material

BT was the first material where FE behaviour was discovered. With an indirect band gap of 3.2 eV, it is practically considered an insulator [38]. However, proper doping can change the conductivity of BT significantly [39]. The crystal structure of BT is of the perovskite-type (ABO_3), as illustrated in figure 2.7a. The Ba^{2+} ions are located on the A-sites and the Ti^{4+} ions on the central B-sites of the lattice, with dodecahedral and octahedral O^{2-} coordination, respectively. The small size of the central Ti^{4+} ion enables a shift (~ 10 pm) from its centre position, giving rise to the system's ferroelectricity. For the tetragonal configuration at RT, values for the piezoelectric coefficients $d_{33} = 85.6$ pC/N, $d_{31} = -34.5$ pC/N and $d_{15} = 392$ pC/N were reported [22]. The domain structure of single crystalline or coarse-grained BT is of herringbone type (cf. figure 2.7b) with 180° and 90° domain walls. In smaller-grained BT the domains show lamellar

order with mainly 90° domain walls. If the grain size is smaller than 300 nm, the microstructure comprises predominantly single-domain grains [40].

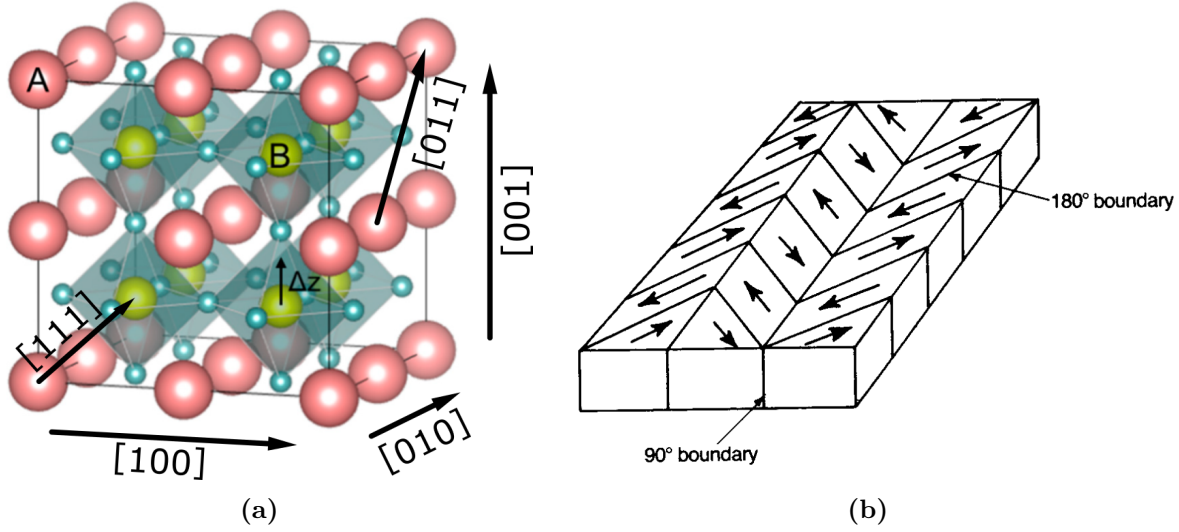


Figure 2.7: Perovskite crystal structure (a) and domain structure of coarse-grained BT (b). In BT, the small displacement of the central Ti^{4+} ion at the B-site results in the emergence of spontaneous polarization and the electric dipoles arrange in domains with 90° and 180° domain walls at RT (Figures taken from [1, 23]).

The temperature-dependent evolution of the lattice parameters, polarization, and relative permittivity is displayed in figures 2.8a, 2.8b, and 2.9. Above T_C , the system is in the PE phase with (pseudo-)cubic symmetry and the dielectric permittivity follows the Curie-Weiss law. Even though no net polarization is exhibited, small and randomly oriented residual electric dipoles are present in the system, since the FE-PE phase transition is not exclusively of displacive type, but of weak order-disorder type as well. Upon further cooling, the permittivity rises and exhibits a peak at $T_C = \sim 120\text{--}130^\circ\text{C}$, where the system exhibits a PE-FE phase transition. Spontaneous polarization and strain occur along the $\langle 001 \rangle$ directions. The tetragonal crystal has one long c -axis and two equally short a -axes. At $\sim 6\text{--}12^\circ\text{C}$, marked by another peak in relative permittivity, a displacive phase transition from the tetragonal to the orthorhombic symmetry

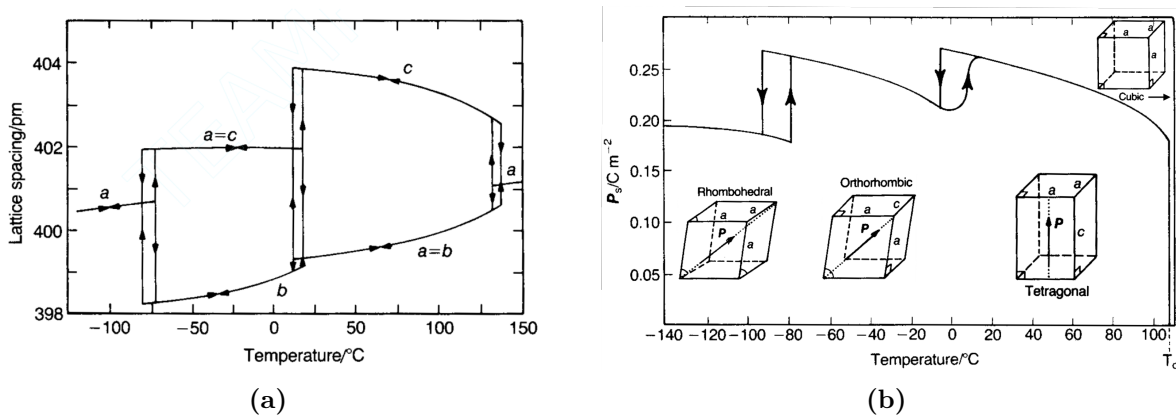


Figure 2.8: Temperature-dependent lattice parameters (a) and polarization (b) of BT. The inset figures in (b) represent the unit cells of the 4 phases of BT (Figure taken from [23]).

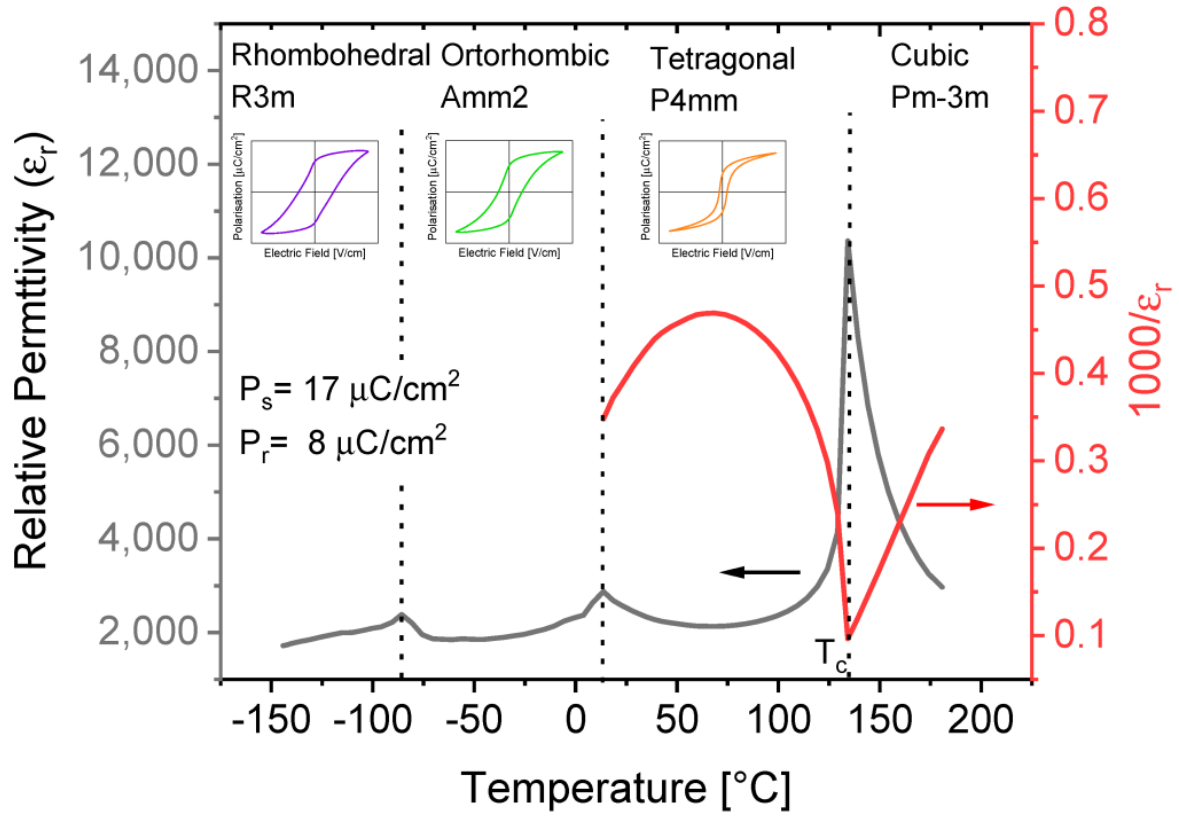


Figure 2.9: Temperature-dependent (inverse) relative permittivity of BT. The linear evolution of the inverse relative permittivity satisfies the Curie-Weiss law in the PE phase. The inset figures qualitatively describe the P-E hysteresis loops of the three FE phases. Note that P_s and P_r are the saturation and remanent polarization, respectively (Figure taken from [1]).

takes place. The polarization changes from the $\langle 001 \rangle$ to the $\langle 011 \rangle$ directions, and the crystal has now two long a-axes and one short c-axis. The last phase transition, again marked by a peak in relative permittivity, occurs at ~ -77 – (-92) °C. Here, the crystal symmetry changes to rhombohedral with polarization along the $\langle 111 \rangle$ directions. All axes are equally long, but the lattice angles fall below 90° [23, 40].

2.3.2 Zr/Nb substituted barium titanate

The FE order of BT can be disrupted by A- or B-site substitution. However, B-site substitution proves to be more effective, since the central Ti^{4+} ion is decisive for the formation of FE order. This thesis addresses only B-site substitution since both Zr^{4+} and Nb^{5+} substitute at the B-site. Typical elements which substitute on the A-site are Sr^{2+} and La^{3+} [1]. As illustrated in figure 2.10, a sufficiently high substitution should induce the (pseudo-)cubic RF state.

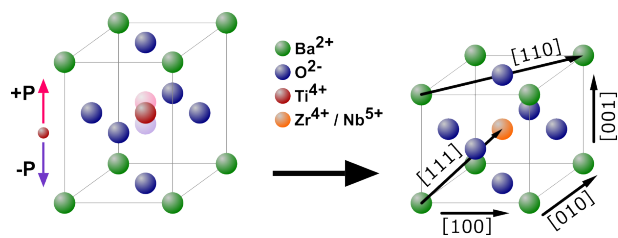


Figure 2.10: B-site substitution of BT. The crystal exhibits (pseudo-)cubic symmetry upon sufficient substitution.

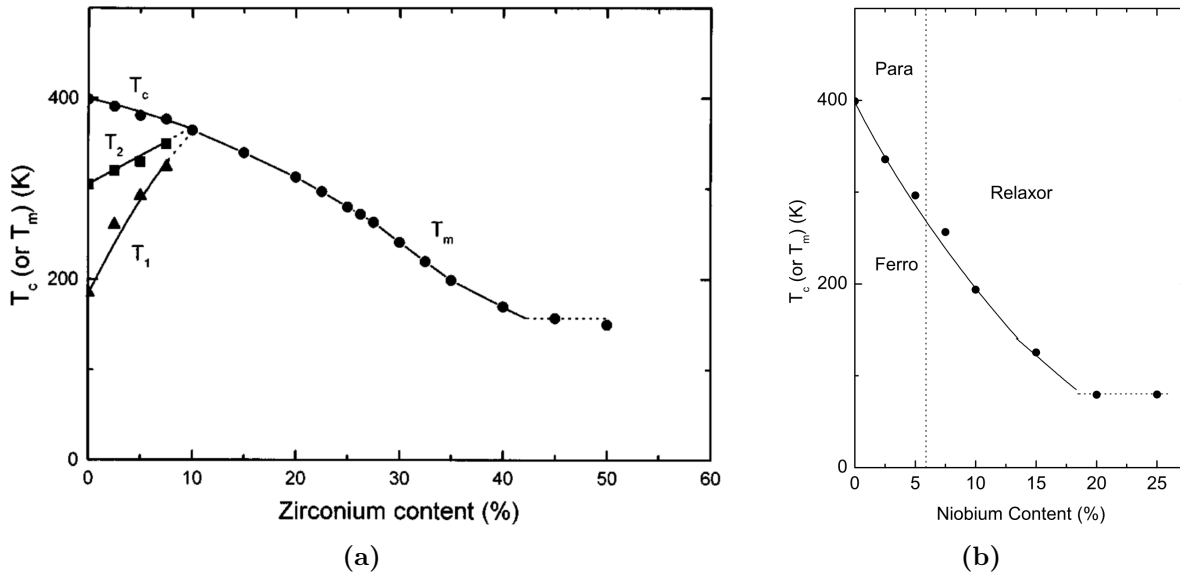


Figure 2.11: Phase diagram of BZT (a) and BNT (b). The BZT system exhibits 3 phase transitions up to the tricritical point at 10% Zr, in contrast to the BNT system which has only one diffusive PE-FE phase transition (Figures taken from [41, 42]).

In octahedral coordination, Zr^{4+} has an ionic radius of 72 pm in comparison to the smaller Ti^{4+} ion with 60.5 pm [43]. It exhibits the same valency, thus the introduction of the foreign Zr^{4+} ions will predominantly lead to random elastic fields in the system. Figure 2.11a displays the phase diagram of BZT. Up to the tricritical point at 10% of Zr, the system still exhibits classical FE behaviour with three phase transitions, accompanied by sharp peaks in the temperature-permittivity evolution. A further increase of the Zr concentration leads to the occurrence of only one phase transition with a diffuse peak in permittivity. In this state, the system behaves like an FE with a DPT and relaxor-like behaviour begins to gradually set in. If the Zr content surpasses 27%, full RF behaviour is observed, with a diffuse and frequency-dispersive phase transition [41]. It must be emphasized that the tricritical point was also reported to be at 15% of Zr substitution. This discrepancy originates most probably from different processing routes of the materials, which can greatly influence the behaviour of FEs and RFs [43–45].

In contrast to Zr^{4+} , the ionic radius of Nb^{5+} with 65 pm [43] is similar to that of the Ti^{4+} ion. Thus the contribution of the random elastic fields is low in comparison to the random electric fields, which emerge from the different valency of the Nb^{5+} ions in octahedral coordination. Due to the close packing of the perovskite lattice, the excess charge of the Nb^{5+} ions is predominantly compensated by either double-charged barium vacancies (V_{Ba}'') or quadruple-charged titanium vacancies (V_{Ti}''''). It was reported in literature that below 3.5% of substitution, V_{Ba}'' are the main source for charge compensation and above 3.5% of substitution, V_{Ti}'''' become increasingly dominant. Furthermore, the two types of vacancies lead to the emergence of two deeply trapped donor states in the band gap of the system, with an activation energy of 1.30 eV and 1.85 eV, respectively [46]. The phase diagram displayed in figure 2.11b reveals that the system behaves like an FE with a DPT, even at low niobium substitution. Above 6% substitution, the system exhibits the characteristic frequency dispersion of the permittivity and can therefore be considered an RF. Niobium substitution leads to inhibited grain growth for all concentrations up to the maximum solubility of 18% [42, 43].

Systems with simultaneous Zr and Nb substitution exhibit random elastic and electric fields, which leads to a very strong disruption of FE behaviour even at low substitution levels [47].

2.4 Piezoresponse Force Microscopy

Piezoresponse Force Microscopy (PFM) is a special method conducted in an AFM [49, 50]. An AFM scans a surface with an extremely sharp tip line by line. The tip is located at the end of a bendable cantilever and its deflection yields the height information. The deflection can be measured with various techniques, but the most prominent one is the use of a laser and position-sensitive photodiode. The measured lines are digitally processed by a controller, which yields a 3D image of a surface. The tip can be in permanent, intermittent, or no contact with the surface, depending on the type of measurement. Permanent contact usually leads to better resolution, whereas intermittent or no contact improves the longevity of the tip in use [51]. In PFM, which was first applied in 1992 by Gütthner and Dransfeld [52], a conductive

tip is scanned in permanent contact along the surface, similar to Conductive AFM (C-AFM) [53], where the local DC current between sample and tip is recorded. But in PFM, an AC bias is applied to the tip to read out the local piezoelectric response of the sample. The tip can also be used to switch the polarization of FEs locally via the application of a sufficiently high DC bias to the tip. This is commonly known as poling. If poling and measuring the piezoresponse are combined in a sophisticated manner, it is called Switching Spectroscopy PFM (SS-PFM). The individual techniques are explained in more detail below.

2.4.1 Contrast formation in PFM

When an AC bias is applied to a conductive tip, which is in contact with an electroelastic surface, a collective oscillation of probe and surface emerges. This electromechanical interaction is attributed to piezoelectricity and electrostriction and the displacement amplitude can be described by the following simplified equation:

$$A = d_{eff} V_{AC} + 2 Q_{eff} V_{DC} V_{AC} \quad (2.8)$$

where d_{eff} and Q_{eff} are the effective piezoelectric and electrostrictive coefficients. The electrostrictive component is usually significantly weaker than the piezoelectric one and usually vanishes in case of zero DC voltage [55]. With PFM, the orientation of the polarization can be read out locally as illustrated in figure 2.13. According to equation 2.4, the application of an electric field causes

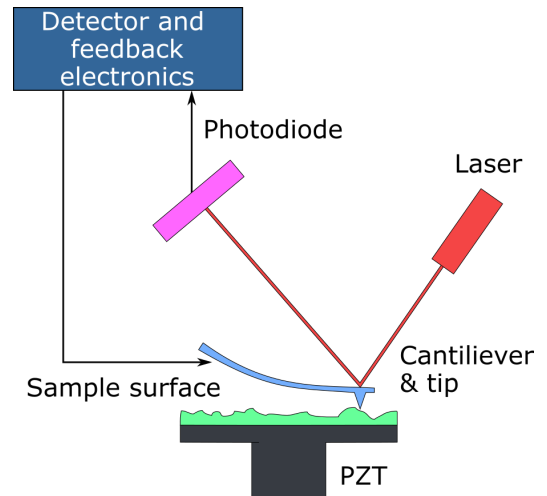


Figure 2.12: Simplified scheme of an AFM [48] (from Wikipedia: copyrighted, dedicated to the public domain by copyright holder without any conditions).

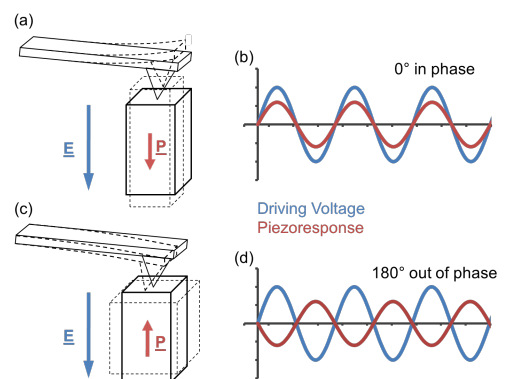


Figure 2.13: In-phase (a, b) and out-of-phase (c, d) vertical response in PFM [54] (from Wikipedia: "Diagram showing cantilever movements from mechanical deformation of piezoelectric domains" General Creative Commons Attribution; by Tertib64 is licensed under CC BY 3.0).

a contraction or elongation of a piezoelectric crystal, depending on their mutual arrangement. In the dynamic case, as a consequence of the AC field of the tip, the oscillation of the crystal is either in phase or out of phase, depending on the vertical orientation of the polarization vector. By that means, up and down domains can be unambiguously discriminated by the phase relation between the applied AC bias and the resulting collective oscillation of the surface, tip, and cantilever. The piezoresponse in PFM can be represented as a point in the complex plane $\mathbf{A} e^{i\phi}$, where \mathbf{A} is the amplitude and ϕ the phase of the oscillation. The signal is usually acquired with a Lock-In-Amplifier (LIA), which yields either the real and imaginary part of the signal or directly the phase and the amplitude. In reality, the piezoresponse is not exclusively directed in the vertical direction but also contains a lateral component. This emerges from the lateral contributions of the piezoelectric tensor of the probed crystal as well as from the arbitrary arrangement of domains in polycrystalline materials. As a consequence, the amplitude is usually not uniform in an image and changes depending on the orientation of the polarization vector [56, 57]. The lateral components of the piezoresponse can be read out by the torsion of the cantilever, and if they are combined with the vertical ones, a deterministic reconstruction of the local polarization vector is possible. This technique is known as Vector Piezoresponse Force Microscopy [58, 59]. In addition, flexoelectricity, electrostatic effects, and also electrochemical strain can give rise to an electromechanical response which can be confused with piezoresponse. Hence, careful evaluation of the obtained data is necessary to distinguish real from fake contrast [60, 61]. These influences will be treated in more detail in the discussion of the results of this thesis.

The amplitude and phase are dependent on the frequency of stimulation in PFM. At a certain frequency, which is determined by the cantilever stiffness and electromechanical properties of the stimulated material, resonance enhancement occurs [62]. This frequency is called contact resonance frequency, and if PFM is conducted at or near this frequency, a great enhancement of the amplitude and signal-to-noise ratio is observed [63]. The contact resonance curve as well as its simplified harmonic oscillator model are displayed in figure 2.14 [64, 65].

2.4.2 Single Frequency PFM

Single Frequency PFM (SF-PFM) can be regarded as the simplest way to measure the piezoresponse of a surface with an AFM. The material is stimulated at a fixed frequency during the scan. One can in general distinguish between three stimulation frequency regimes where SF-PFM can be operated (cf. figure 2.14). In standard PFM, the stimulation frequency is far below the contact resonance (10 kHz–100 kHz) to avoid any resonance effects, bringing up the opportunity for straightforward interpretation or even quantification of the images. High-frequency PFM (1 MHz–10 MHz) shares these advantages but enables faster scan speeds due to the significantly higher stimulation frequency. However, the equipment necessary for reliable operation in these frequency regimes is more expensive. The third frequency regime is near or at the contact resonance frequency, with significant improvement of the signal-to-noise ratio, but at the expense of straightforward quantifiability. The reasons for these difficulties are topographic crosstalk and arbitrary shifts in the contact resonance frequency arising from changes in tip-surface contact properties [61, 66].

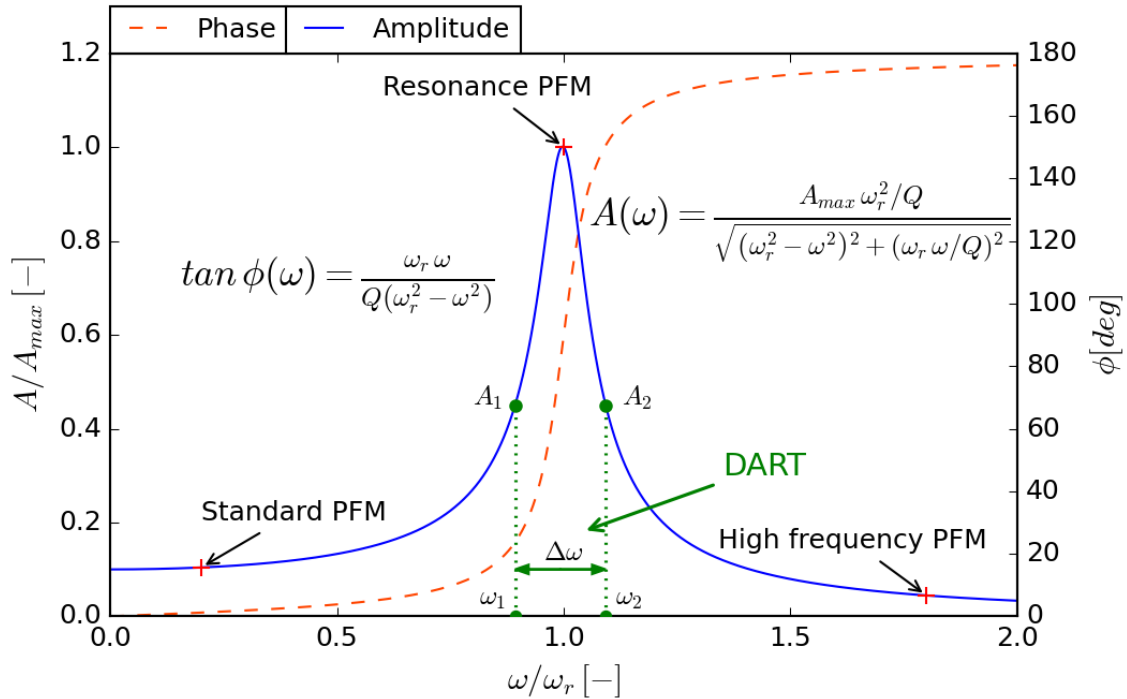


Figure 2.14: Contact resonance curve in PFM. The frequency-dependent amplitude and phase can be described by a model of a harmonic oscillator, where A_{max} , ω_r , and Q are the amplitude at resonance, (angular) resonance frequency, and quality factor of the oscillation, respectively.

2.4.3 Dual AC Resonance Tracking

Dual AC Resonance Tracking is a feedback mode in PFM that utilizes resonance enhancement while minimizing negative influences resulting from changes in the contact properties between tip and surface. These changes usually result in a shift of the (angular) resonance frequency, i.e. a significant change in phase and amplitude if the stimulation frequency is fixed. To overcome this, the (angular) resonance frequency is actively tracked by stimulating and measuring the piezoresponse at two (angular) frequencies, below and above the (angular) contact resonance frequency (cf. figure 2.14). The difference between these two (angular) frequencies $\Delta\omega$ is held constant and a feedback loop equalizes the two amplitudes by adjusting both (angular) frequencies. Provided that the shape of the resonance curve does not change abruptly during the scan, the (angular) contact resonance frequency can be effectively tracked and topographic cross-talk is minimized [67]. Even though neither of the two (angular) frequencies is directly at resonance, sufficient contrast enhancement can be made by choosing a narrow (angular) frequency window $\Delta\omega$. However, if $\Delta\omega$ is too narrow, the measurement becomes susceptible to loss of frequency tracking, resulting in inferior image quality. DART measurements deliver two amplitude signals, which should be identical in theory, as well as two phase signals and one centre frequency signal.

2.4.4 Local polarization switching with an AFM

The polarization of an FE can be locally reversed by applying a sufficiently high DC bias to the tip. By those means, patterns can be written into an FE surface. The spatial extent of switching is dependent on the voltage, the writing speed and the relative humidity on the surface [68]. Besides polarization switching, charges and defects may also be accumulated or even induced by the high electric field, resulting in fake PFM contrast in subsequent measurements [69].

2.4.5 Switching Spectroscopy PFM

Switching Spectroscopy PFM (SS-PFM) enables local probing of the polarization switching dynamics of FEs. It is a point spectroscopy mode, i.e. the tip is not scanned over the surface during the data acquisition. While the tip is in contact with the surface, a complex signal is applied to it. It comprises a low-frequency rectangular signal, with a triangularly ramped-up amplitude. A high-frequency sinusoidal signal is superimposed over the rectangular signal (cf. figure 2.15a). Both parts of the signal serve a different purpose. The low-frequency signal can practically be viewed as short pulses with changing amplitude. These pulses lead to domain nucleation and growth beneath the tip, i.e. the polarization is switched gradually. This gradual switching process can be monitored by utilizing the high-frequency signal, which is identical to the signal used in standard PFM measurements. The piezoresponse acquired during the pulse is referred to as the active-field response (AmpOn) and the piezoresponse in the field-free case (after the pulse) is called the remanent response (AmpOff). Especially the AmpOff curves are of great interest for the validation of FE behaviour, since it requires a spontaneous, reversible polarization in the absence of any DC bias. The AmpOn signal, on the other hand, can give insight into field-dependent dynamics as well as electrostrictive interaction [70, 71]. Figure 2.15b and 2.15c illustrate the typical AmpOff phase and amplitude evolution of an FE material. The switching process is illustrated in figure 2.15d. Note that besides the phase and amplitude representation of a switching experiment, real and imaginary parts are equally valid representations of the signal and are often used for the depiction of hysteresis loops in SS-PFM.

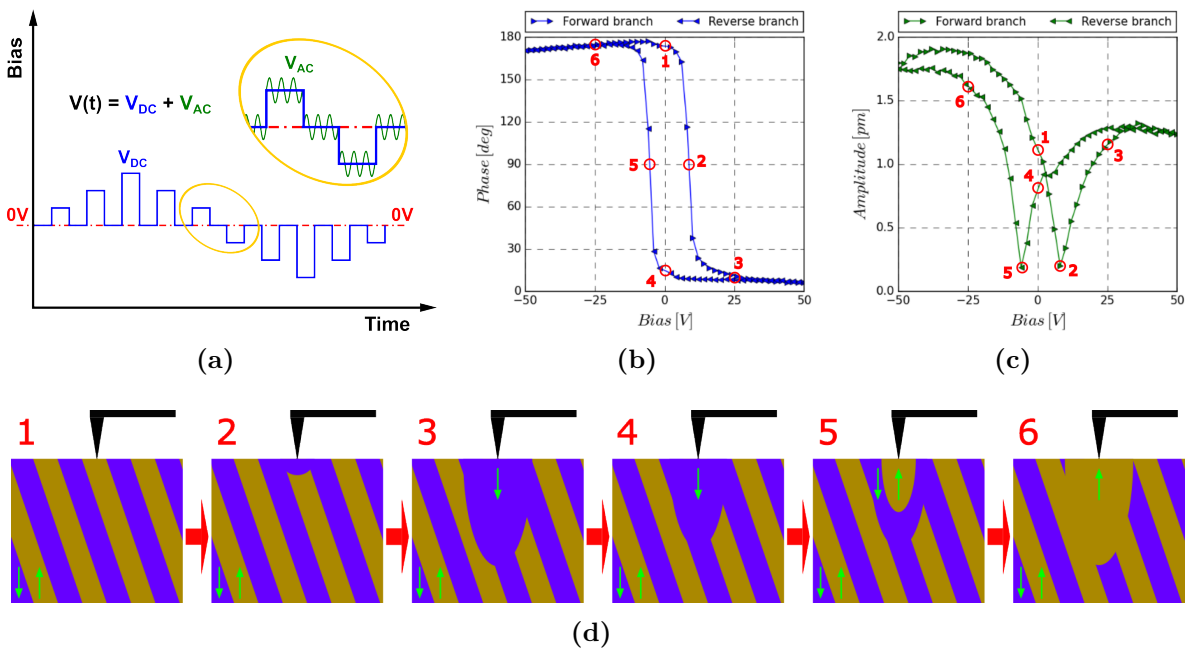


Figure 2.15: Stimulating bias (a), phase (b) and amplitude (c) in SS-PFM. Figure (d) illustrates the nucleation and growth of domains in a lamellar antiparallel domain structure during hysteresis acquisition. (1) shows the piezoresponse of the pristine lamellar structure. Raising the DC voltage leads to the nucleation (2), growth, and saturation (3) of a domain with opposite polarization. Releasing the bias leads to the equilibrium configuration of the newly formed domain (4). A new, antiparallel polarized domain nucleates upon the reverse of the DC bias (5) and it grows at the expense of the previously formed domain (6).

Besides ferroelectricity, other mechanisms on surfaces can give rise to PFM hysteresis loops as well, which can be confused with real ferroelectricity. For example, if the probed material is not a full insulator, Joule Heating can produce hysteresis loops in the AmpOn signal. Chemical dipoles, injected charges, field effect, and Vegard strain can even lead to hysteresis loops in the AmpOff signal. The latter involves the attraction of charged ions from the bulk, which gives rise to a strong electromechanical response, possibly more dominant than the contrast emerging from ferroelectricity. This effect led to the implementation of Electrochemical Strain Microscopy (ESM), an AFM method used to probe electrochemical activity in cathode and anode materials as well as semiconductors and oxides [72]. In general, a change in polarization, charge or concentration can give rise to AmpOff hysteresis loops in SS-PFM. However, true FE switching exclusively involves a change in polarization. Hence, careful inspection and evaluation of the data is necessary to distinguish real from fake PFM hystereses [69].

3 Experimental methods and data evaluation

3.1 Sample synthesis

The examined samples were synthesized, consolidated, and sintered at the Institute for Chemistry and Technology of Materials, Graz University of Technology. The powder for the synthesis of $\text{BaZr}_x\text{Nb}_y\text{Ti}_{1-x-y}\text{O}_3$ comprises the precursors BaCO_3 , TiO_2 , ZrO_2 , and Nb_2O_5 . The following steps are necessary to produce polycrystalline, high-quality and dense sample disks [73]:

1. Weighing the precursors according to the desired composition and mixing in a milling bowl.
2. Powder milling with a planetary mono mill. The balls are made of yttria-stabilized zirconia.
3. Drying and sieving of the milled powder.
4. Calcination of the powder at 1250 °C for 5 h in a chamber furnace.
5. X-ray diffraction to validate a complete reaction and the absence of secondary phases.
6. Milling of the calcinated powder to reduce the size of agglomerates and enhance sintering activity.
7. Drying and sieving.
8. Measurement of the grain size distribution with a laser particle size analyzer.
9. Introduction of the binder (polyethylene glycol).
10. Uniaxial pressing of the powder into disks.
11. Debinding of the green body at 450 °C for 30 min in a chamber furnace.
12. Sintering between 1360–1450 °C for 5 h in a chamber furnace.

Sample name	% Zr	% Nb
BT	0	0
BZT_10	10	0
BZT_20	20	0
BZT_30	30	0
BZT_40	40	0
BNT_2p5	0	2.5
BNT_5	0	5
BNT_7	0	7
BNT_10	0	10
BNT_15	0	15
BNZT_2p5_10	10	2.5
BNZT_2p5_20	20	2.5
BNZT_2p5_30	30	2.5
BNZT_2p5_40	40	2.5

Table 3.1: Synthesized samples.

Table 3.1 lists the samples which were synthesized for the PFM analysis. The relative sinter density, determined by the Archimedes method, is above 95% for all samples.

3.2 Sample preparation

Electromechanical probing with PFM requires a clean, flat, and tension-free surface. Hence, a top-quality polishing procedure is decisive for a successful characterization. To meet these requirements, the samples were polished using the semi-automated ceramic polisher **Tegramin-30** from the manufacturer **Struers**, with adjustable force and automated liquid suspension. The samples were embedded in a self-curing resin, **VersoCit-2** from **Struers**. The two active agents, a powder and liquid, have to be mixed in volume fractions of 2:1. The most critical property for reliable PFM measurements on FEs is a tension-free surface. The reason is that BT is ferroelastic and residual strain on the surface can result in ferroelastic switching, which also changes the upper surface layer's polarisation, disguising the real domain pattern underneath. A solution for that problem is the use of Oxide Polishing Suspensions (OP-S) at the end of polishing, which

releases residual strain caused by the deformations from preceding polishing steps [74]. Table 3.2 lists the applied polishing steps and their most important parameters.

Nr	Disc	Liquids	F[N]	Time[min]	f_D [rpm]	f_H [rpm]
1	MD-Piano 220	H ₂ O	30	1:00	300	150
2	MD-Plan	DP-S 9 μm & LUB	30	3:00	150	150
3	MD-Plan	DP-S 9 μm & LUB	15	3:00	150	150
4	MD-Dur	DP-S 6 μm & LUB	30	3:00	150	150
5	MD-Dur	DP-S 6 μm & LUB	15	3:00	150	150
6	MD-Dac	DP-S 3 μm & LUB	30	3:00	150	150
7	MD-Dac	DP-S 3 μm & LUB	15	3:00	150	150
8	MD-Dur	DP-S 1 μm & LUB	20	5:00	180	150
9	MD-Dur	DP-S 1 μm & LUB	10	5:00	180	150
10	MD-Chem	OP-S NonDry	15	1:30	150	150

Table 3.2: Polishing steps for the sample preparation. Note that f_D , f_H , F, DP-S and LUB stand for disk rotation speed, head rotation speed, contact force, diamond polishing suspension and lubricant, respectively.

3.3 Optical microscopy (OM) inspection

Polycrystalline ceramics usually contain pores as a result of their processing route. In PFM, large pores should be avoided since they often contain debris from the polishing. This debris can be picked up by the tip, causing an abrupt change in electromechanical contrast and leading to inferior or even disturbed image quality. Hence, pore-free spots are of particular interest for PFM investigations. However, pores can also serve as characteristic details, facilitating the targeting of a desired spot with the internal (and often inferior) microscope of an AFM. Therefore, the search for spots was conducted using a **Zeiss Axio Optical Microscope**. In figure 3.1, a characteristic pore is marked by the red circle and a promising pore-free spot by the blue circle.

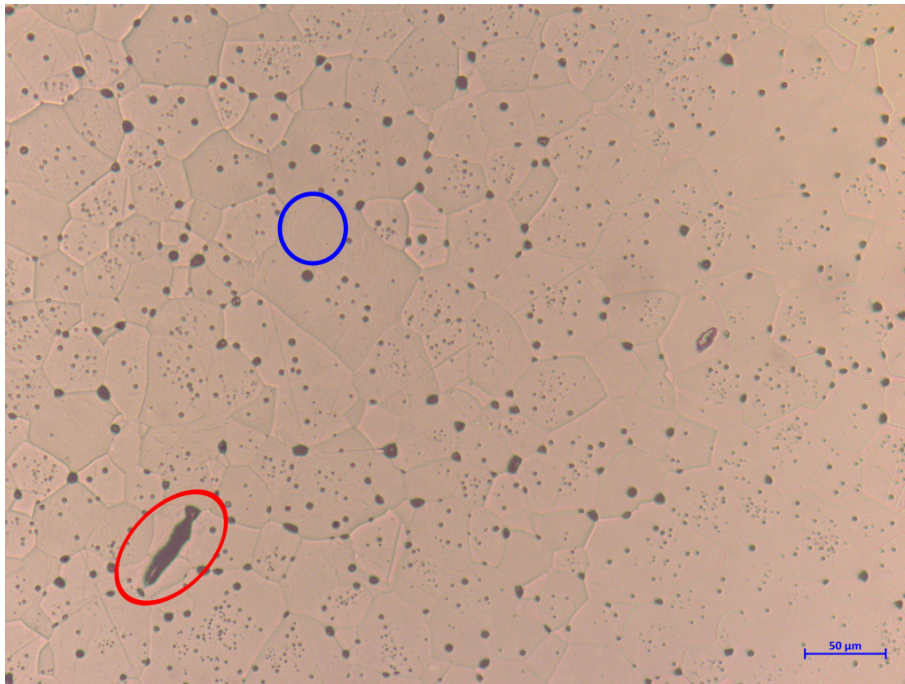


Figure 3.1: OM picture of an interesting spot (blue) close to a characteristic pore (red).

3.4 PFM measurements

The PFM measurements are conducted using an **Asylum Research MFP-3D** AFM in combination with an external LIA of the type **SR830** from **Stanford Research Systems** and an external voltage amplifier **F10A** from **Acquitek** (10 times amplification with max. output voltage of ± 100 V). A detailed description of the wiring and settings in the asylum software can be found elsewhere [75].

The samples are mounted in the heater cell of the AFM to enable temperature-dependent PFM measurements. They are placed on thin glass slides, and a heat-conducting paste was spread between the slide-heater interface to maximize thermal conductivity. The samples are electrically grounded using a thin wire and conductive silver paste. In addition, a thermocouple (type T) is also immersed in the silver paste to measure the sample temperature (cf. figure 3.2).

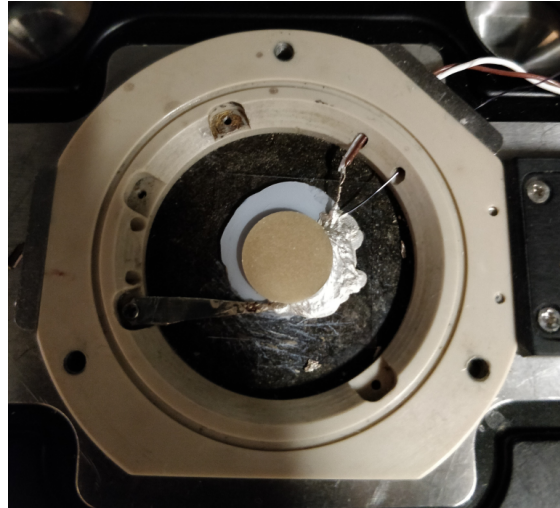


Figure 3.2: Mounted sample (beige) on a glass slide and heat-conducting paste (grey) beneath. The electrical grounding wire (black) and thermocouple (brown and white) are connected to the sample with silver paste.

In PFM measurements, probes with an electrically conductive tip are necessary. In order to minimize electrostatic contributions, probes with a high cantilever stiffness were used [61]. Table 3.3 lists the used probe types for the PFM measurements. The first probe type was used for SF-PFM imaging and polarization switching; the other three for the SS-PFM experiments. The cantilever’s virtual deflection, inverse optical lever sensitivity (InvOLS) as well as spring constant (thermal sweep method) were calibrated before first use according to the Imaging and Spectroscopy Applications Guide from Asylum Research [76].

Manufacturer	Probe name	Tip coating	Tip radius [nm]	f_R [kHz]	k [N/m]
NT-MDT	NSG30/Pt	Pt	35	240–440	22–100
NT-MDT	NSG10/TiN	TiN	20–30	140–390	3.1–37.6
NT-MDT	HA_NC/W2C	W ₂ C	<35	140–235	3.5–12
NT-MDT	NSG10/Pt	Pt	35	140–390	3.1–37.6

Table 3.3: Probes used in the PFM measurements. f_R and k are the resonance frequency and cantilever force constant.

3.4.1 Imaging spontaneous polarization with PFM

The first measurement conducted on a freshly polished sample is SF-PFM with the external LIA and voltage amplifier. The domain structure of at least three interesting spots is imaged. The square-shaped scan areas range between 10 μm and 25 μm in size and if necessary, smaller scans are also conducted. However, it must be mentioned that reducing the image size to arbitrarily small values does not result in the resolution of ever smaller domains, since the theoretical lateral resolution limit in PFM is tied to the tip curvature radius as well as to the elastic, dielectric and surface properties of the material [77]. The amplitude of the stimulating signal is 1 V–6 V with a drive frequency between 10 kHz and 12 kHz. The proportionality factor of the LIA is adjusted according to the measured response and the time constant is set between 1 ms–10 ms.

3.4.2 Local polarization switching by applying a DC-bias to the tip

Before polarization switching, the domain structure is measured using SF-PFM. Afterwards, a smaller ($5\ \mu\text{m} \times 5\ \mu\text{m}$ or $10\ \mu\text{m} \times 10\ \mu\text{m}$) square area is scanned in the centre of the previous image, with a DC bias of $\pm 50\ \text{V}$ applied to the tip. In the ideal case, this should lead to the creation of a square-shaped domain with uniaxial polarization. Then, two SF-PFM scans are conducted, one immediately after switching and one after at least 12 h to estimate the stability of the induced domain(s).

3.4.3 Probing the local switching dynamics utilizing SS-PFM

The SS-PFM measurements have been conducted in DART mode to enhance the contrast during the switching experiments. Only the external voltage amplifier was used for the measurements while the external LIA was disconnected. Instead, the system's internal LIA was employed. The spectroscopy experiments were conducted on a total of 36 points, preferably covering several grains of the microstructure to get good statistics, as illustrated in figure 3.3. These point maps were measured in steps of $5\ ^\circ\text{C}$ between $30\ ^\circ\text{C}$ and $180\ ^\circ\text{C}$. The time for the thermal equilibration before a measurement was at least five minutes.

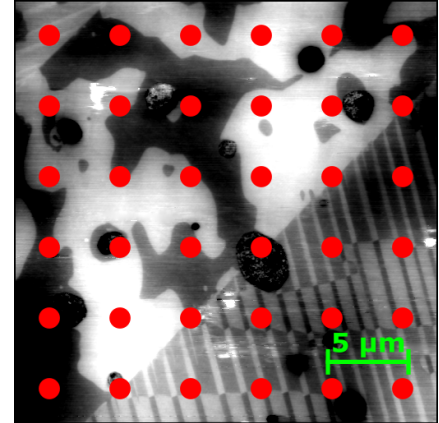


Figure 3.3: Representation of the probed points in an SS-PFM experiment. Every red dot marks the location of an SS-PFM measurement.

The parameters of the stimulating signal were as given: The amplitude and frequency of the sinusoidal part were $1\ \text{V}$ – $6\ \text{V}$ and $1\ \text{MHz}$ – $2\ \text{MHz}$, respectively. The pulse time of the rectangular signal was $50\ \text{ms}$ with a maximum amplitude of ± 50

V . The enveloping triangular signal had a frequency of $0.2\ \text{Hz}$ and had two full cycles. The DART frequency window Δf was between $10\ \text{kHz}$ and $25\ \text{kHz}$ (corresponding to a $\Delta\omega$ range of $62 \cdot 10^3\ \text{1/s}$ to $157 \cdot 10^3\ \text{1/s}$), depending on the shape of the contact resonance curve. The quality factor of the oscillation was adopted from the AFM system's internal calculation.

3.5 Data evaluation

The measurements performed in this thesis yielded a total of 160 PFM images and more than 50,000 phase and amplitude curves from the SS-PFM experiments. This large quantity of data, particularly the 50,000 curves from SS-PFM, necessitates a semi-automated, computer-aided evaluation. The PFM pictures were evaluated using the software Gwyddion [78] and the programming language Python 3 [79]. The SS-PFM experiments were evaluated with the programming language R [80] as well as Python 3. The code can be accessed via GitHub: <https://github.com/muephy11/POLDERS-PFM>.

3.5.1 SF-PFM evaluation

The topographic information of the SF-PFM scans is levelled by mean plane subtraction, and the scan rows are aligned using the median of differences method. If necessary, horizontal scars are removed using the algorithm from Gwyddion. The LIA acquires the piezoresponse in xy-mode corresponding to the real and imaginary parts of the signal. An example of the individual data points of a PFM scan in the complex plane is displayed in figure 3.4. Ideally, the PFM data points

should only lie on the positive as well as the negative real axis, corresponding to either 0° or 180° phase values with varying amplitudes. However, in reality, the data points deviate from this line due to random noise, electrostatic contributions, and capacitive influences from the instruments. The first leads to random scattering, the second to a vertical and horizontal shift of all data points in the complex plane, and the third to a global phase shift. While the correction of deviations of the first or second type involves sophisticated calibration, the latter necessitates smaller efforts. Consequently, the PFM data correction is limited to the phase correction in this thesis.

An individual data point P_j in the complex plane is described mathematically by:

$$P_j = \text{Re}(P_j) + i \text{Im}(P_j) = A_j \cdot e^{i\phi_j} \quad (3.1)$$

where $\text{Re}(P_j)$, $\text{Im}(P_j)$, A_j , and ϕ_j are the real part, imaginary part, amplitude and phase of the complex point, respectively. On average, the noisy data points lie on a straight line, as illustrated in figure 3.4 by the blue point cloud. Hence, the average correlation between the real and imaginary part of all points P can be described by the following linear equation:

$$\text{Im}(P) = k \cdot \text{Re}(P) + d \quad (3.2)$$

where k and d are the slope and intercept of the line. The fit of the data points is conducted by using the least squares algorithm `linalg.lstsq` from the Python package Numpy [81]. The angle θ between the linear fit and the real axis can be determined by the relation $\theta = \arctan(k)$. Now the phase-corrected piezoresponse can be calculated as follows:

$$P_{j,corr} = P_j \cdot e^{-i\theta} \cdot \text{InvOLS} \cdot f_{LIA} \cdot f_{DA}. \quad (3.3)$$

The multiplication of the first two factors results in a rotation of the signal in the complex plane by the angle θ , as illustrated by the dotted lines in figure 3.4. The multiplication with the `InvOLS` transforms the signal from LIA voltage to PFM signal units (i.e. volts to picometers). The variable f_{LIA} is the amplification correction from the LIA and f_{DA} is a scaling factor that corrects the different drive amplitudes used in the measurements by scaling the piezoresponse as if it was stimulated by 1V of drive amplitude ($f_{DA} = 1V/\text{drive amplitude}$), with the intention to make the SF-PFM scans of different samples more comparable. The complex number of the phase-corrected piezoresponse has the unit [pm]. The amplitude, phase and response of the signal can be obtained by extracting the magnitude, angle and real part of the complex data points. The response image (\mathbf{R}) can be viewed as a superposition of the information contained in the phase and amplitude images ($\mathbf{R} = \mathbf{A} \cdot \cos(\phi)$). It is often used as a compact alternative to the amplitude and phase image combination (cf. figures 3.5a, 3.5b, and 3.5c).

In addition to the images, statistical data of the piezoresponse in the form of discrete distributions was calculated as well. The normalized distributions were calculated using Gwyddion and they

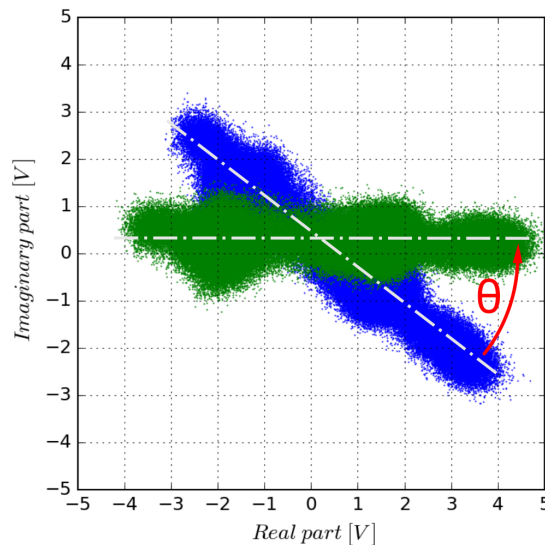


Figure 3.4: Raw data points (blue) and phase-corrected data points (green) in SF-PFM.

fulfil the following conditions:

$$\int_0^{\infty} \rho(A) dA = \int_{-\pi}^{\pi} \rho(\phi) d\phi = \int_{-\infty}^{\infty} \rho(R) dR = 1. \quad (3.4)$$

An example of the amplitude (AD), phase (PD), and response (RD) distribution of a model FE is illustrated in figures 3.5d, 3.5e, and 3.5f. Note that the amplitude of antiparallel domains can be unequal due to electrostatic contributions.

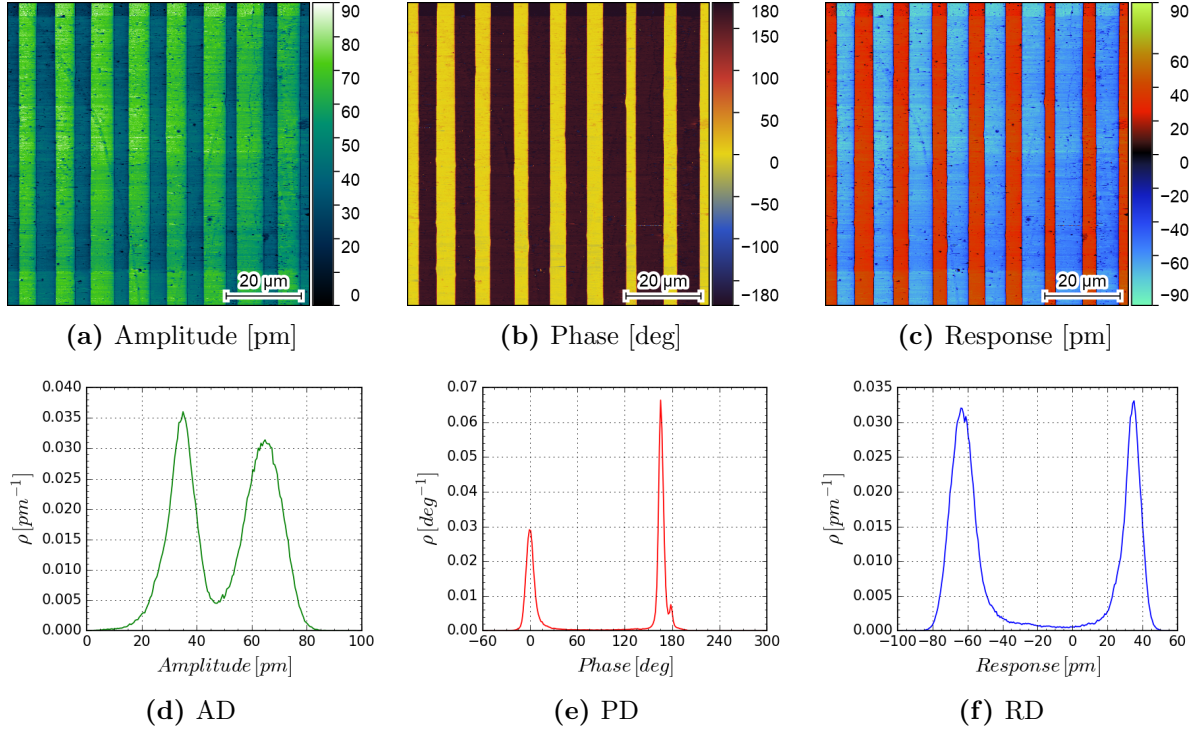


Figure 3.5: Amplitude (a), phase (b), and response (c) and their distributions (d, e, f) of periodically poled lithium niobate. The response is calculated from the amplitude and phase. The unit of the colour ruler is located below the image in brackets.

3.5.2 SS-PFM evaluation

The great extent of acquired data necessitates a semi-automated evaluation and classification of the SS-PFM data. In the ideal case, the phase, amplitude, and response curves of an individual SS-PFM experiment have the same appearance as the curves in figure 2.15b, 2.15c, and 3.7b. However, non-piezoelectric contributions as well as sudden changes in contact properties can significantly alter the shape of the acquired data and can heavily impede the data evaluation and interpretation. Hence, a proper pre-filtering algorithm was necessary to exclude failed experiments from the final evaluation. After a detailed inspection of the data, three criteria that indicate a successful SS-PFM experiment were derived. However, it must be noted that these criteria represent a subjective, but unambiguously defined selection of the data. The mathematical models of the SS-PFM evaluation were adopted from the work of Jesse et al., which treated the quantification of SS-PFM data [82].

Prior to the application of the filters, another pre-correction of the data is necessary. Since the resonance enhancement and especially the Q-factor are dependent on the tip-sample interaction, the effective piezoresponse can significantly vary from sample to sample. Hence, it is necessary

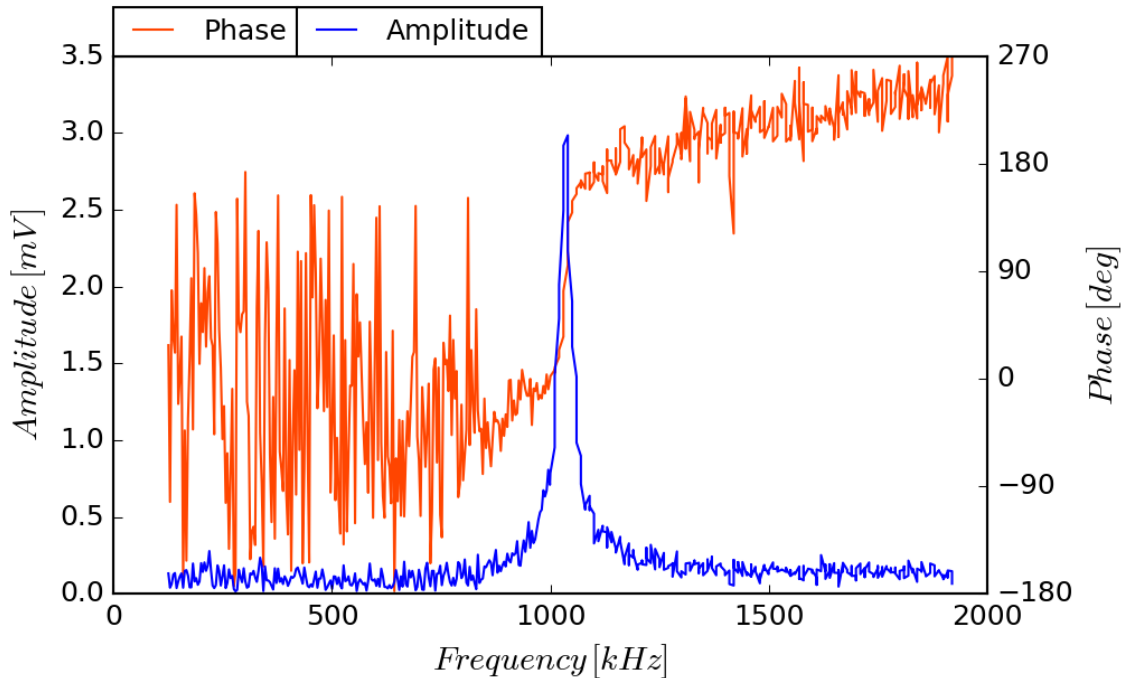


Figure 3.6: Result of a PFM frequency tune in an Asylum MFP-3D. A phase change of approximately 180° occurs when surpassing the contact resonance frequency, which is indicated by the amplitude peak. The frequency-dependent phase evolution is often noisier below the contact resonance frequency than above it.

to consider this variation for a conclusive comparison of the SS-PFM results. The frequency-dependence of the amplitude and phase, obtained from a PFM frequency tune, is illustrated in figure 3.6. While the shift in phase at resonance can be corrected by simply rotating the data points as illustrated in figure 3.4, a more sophisticated correction is necessary for the amplitude. The purpose of this correction is to scale the amplitude as if it had been measured in the low-frequency range (e.g. at 10 kHz). The frequency-dependent amplitude $\mathbf{A}_j(\omega_j)$ of individual PFM data points \mathbf{P}_i can be modelled by a simplified harmonic oscillator equation [64, 65]:

$$\mathbf{A}_j(\omega_j) = \frac{\mathbf{A}_{j,max} \omega_{j,r}^2 / Q}{\sqrt{(\omega_{j,r}^2 - \omega_j^2)^2 + (\omega_{j,r} \omega_j / Q)^2}}. \quad (3.5)$$

$\mathbf{A}_{j,max}$ is the amplitude at resonance and $\omega_{j,r}^2$ is the (angular) contact resonance frequency of the system. In literature, the resonance frequency is occasionally replaced by the eigenfrequency of the system, since both are practically equal under the condition of low damping. The quality factor is obtained from the AFM's internal calculation after a frequency tune, as illustrated in figure 3.6. In DART, the two amplitudes below and above the resonance frequency are equal and the two stimulation frequencies can be derived from the centre frequency $\omega_{j,c}$ and frequency width $\Delta\omega$:

$$\omega_{j,1} = \omega_{j,c} - \Delta\omega/2 \quad \text{and} \quad \omega_{j,2} = \omega_{j,c} + \Delta\omega/2. \quad (3.6)$$

Note that $\omega_{j,c}$ is close, but not equal to $\omega_{j,r}$. The two corresponding amplitudes $\mathbf{A}_{j,1} = \mathbf{A}_j(\omega_{j,1})$ and $\mathbf{A}_{j,2} = \mathbf{A}_j(\omega_{j,2})$ can be equalized, since the AFM's feedback loop acts in the same way,

leading to the following expression:

$$\frac{A_{j,max} \omega_{j,r}^2 / Q}{\sqrt{(\omega_{j,r}^2 - \omega_{j,1}^2)^2 + (\omega_{j,r} \omega_{j,1} / Q)^2}} = \frac{A_{j,max} \omega_{j,r}^2 / Q}{\sqrt{(\omega_{j,r}^2 - \omega_{j,2}^2)^2 + (\omega_{j,r} \omega_{j,2} / Q)^2}}. \quad (3.7)$$

Rearranging yields the resonance frequency of the PFM data point $\mathbf{P}_j(\omega_j)$:

$$\omega_{j,r} = \sqrt{\frac{(\omega_{j,2}^4 - \omega_{j,1}^4) Q^2}{2 Q^2 (\omega_{j,2}^2 - \omega_{j,1}^2) + \omega_{j,1}^2 - \omega_{j,2}^2}}. \quad (3.8)$$

Now the amplitude at resonance $\mathbf{A}_{j,max} = \mathbf{A}_j(\omega_{j,r})$ can be calculated:

$$A_{j,max} = \frac{A_{j,1} Q}{\omega_{j,r}^2} \sqrt{(\omega_{j,r}^2 - \omega_{j,1}^2)^2 + (\omega_{j,r} \omega_{j,1} / Q)^2}. \quad (3.9)$$

Now that the resonance curve is fully determined, the corrected off-resonance amplitude for each PFM data point $\mathbf{P}_{j,corr}(\omega_j = \omega_{corr})$ can be calculated by simply inserting the desired frequency into equation 3.5. The chosen frequency was **11.763 kHz** corresponding to an angular frequency of **$73.909 \cdot 10^3$ 1/s**. A scaling factor correction similar to equation 3.3 is applied as well.

The first filter is defined by the shape of the data points in the complex plane and by how well they follow a linear function. The SS-PFM data is less noisy than the SF-PFM data, due to the point-wise, resonance-enhanced acquisition of the hysteresis loops. However, non-piezoelectric contributions can still alter the signal significantly. An ideal example of the data points is illustrated by the green dotted line in figure 3.7a. Here, a fit with equation 3.2 would yield a high R^2 value, often referred to as the coefficient of determination in statistics [83]. On the contrary, the orange dotted line in figure 3.7a would yield a low R^2 value due to the non-linear part. Curves with an R^2 value smaller than 0.75 are omitted. If the curves surpass the threshold, a phase correction $\mathbf{P}_{j,corr} = \mathbf{P}_j \cdot e^{-i\theta}$ is conducted.

The second filter is based on the evolution of the phase and contains three independent selection criteria. An ideal example of the phase evolution in an SS-PFM experiment is illustrated by the grey line in the inset of figure 3.7a. The hysteresis saturates at 0° or 180° and only deviates from either of the two values during the switching process. The evolution of the phase can be divided into two parts, which are called the forward (ϕ^+) and reverse (ϕ^-) branches. Each branch is described by a sigmoid function with an additional linear part:

$$\phi^+ = b_1 - b_2 \cdot \left(1 + \exp\left(\frac{V - b_3}{b_5}\right)\right)^{-1} + b_6 \cdot V \quad (3.10)$$

$$\phi^- = b_1 - b_2 \cdot \left(1 + \exp\left(\frac{V - b_4}{b_5}\right)\right)^{-1} + b_6 \cdot V \quad (3.11)$$

where $\mathbf{b}_1 \dots \mathbf{b}_6$ are the fitting parameters. Both functions are simultaneously fitted, within the variable boundaries displayed in table 3.4, using the `optimize.curve_fit` function from Scipy [84] in Python 3. Besides the R^2 value, three parameters can be derived from the fit for the selection criteria: $\phi_{max} = \mathbf{b}_1$, $\phi_{min} = \mathbf{b}_1 - \mathbf{b}_2$, and $\Delta\phi = \mathbf{b}_2$. The former two parameters are

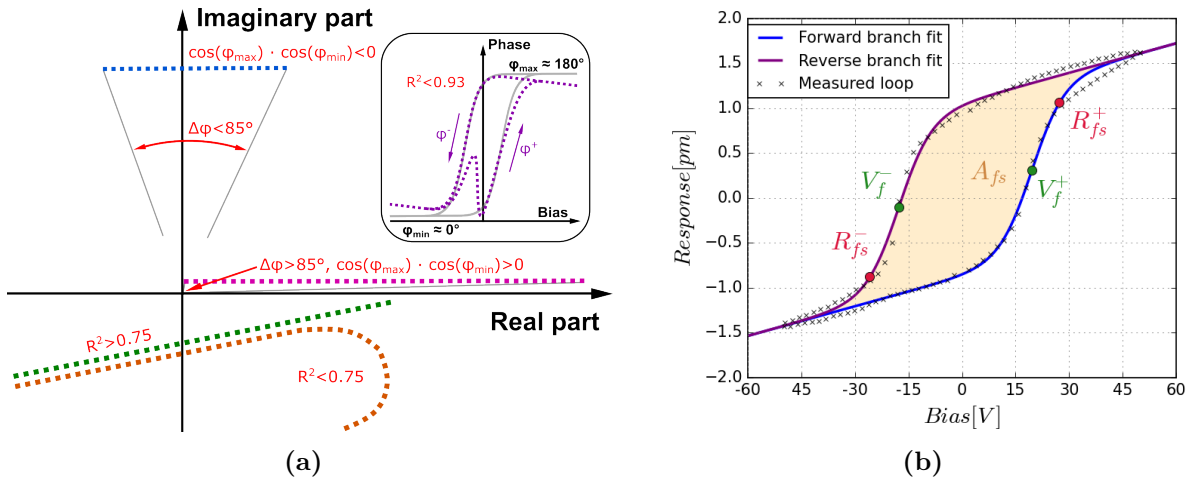


Figure 3.7: SS-PFM signal in the complex plane (a) and response hysteresis (b). Ideally, the data points of an SS-PFM experiment should lie on a straight line in the complex plane (with small deviations during the quasi-discontinuous polarization switching process), as illustrated by the green dotted line. However, non-piezoelectric contributions can shift or even distort the data (cf. orange, pink, and blue dotted lines), which leads to a distorted hysteresis loop. The inset in (a) displays the ideal (grey full line) and distorted (purple dotted line) evolution of the phase during a switching experiment. Note that V_f^- , V_f^+ , R_{fs}^- , R_{fs}^+ , and A_{fs} are the negative Coercive Bias, positive Coercive Bias, negative Saturation Response, positive Saturation Response, and effective Work of Switching parameter, respectively.

the saturation phases after a full switch and the latter is the phase change during the switch. With these parameters, the following three criteria are defined:

$$1) R^2 > 0.93 \quad 2) \Delta\phi > 85^\circ \quad 3) \cos(\phi_{max}) \cdot \cos(\phi_{min}) < 0. \quad (3.12)$$

The first criterion limits the accepted deviation of the measured phase hysteresis from its optimal shape, as illustrated in figure 3.7a by the phase graph. The purple-dotted hysteresis deviates from the ideal grey hysteresis in the saturation regime and also at the onset of a switch, resulting in a R^2 value below the threshold. The second criterion filters curves that do not exhibit a sufficiently high change of phase during the switching process, as illustrated by the blue dotted line in figure 3.7a. The change of phase is lower than the threshold, even though the data points lie on a straight line in the complex plane.

This can be attributed to a large imaginary shift of all data points, possibly originating from non-piezoelectric contributions. Such curves are therefore omitted as well. The third criterion tests for an actual switch of FE polarization, which is indicated by a change of sign of the real part of the piezoresponse, here simply referred to as the response. Since the amplitude can only exhibit values with a positive sign, the change of sign has to originate from the cosine of the phase. Consequently, the product of the two saturation phases' cosines will be negative in case of a successful FE polarization switch. The pink line in figure 3.7a illustrates a case where this criterion is not fulfilled. Even though the second criterion is fulfilled ($\Delta\phi > 85^\circ$), the

Variable	Lower	Upper
b_1 [deg]	$\min(\phi_j)$	$\max(\phi_j)$
b_2 [deg]	0	∞
b_3 [V]	-50	50
b_4 [V]	-50	50
b_5 [V]	$-\infty$	∞
b_6 [deg/V]	-0.4	0.4

Table 3.4: Phase fit – boundaries of the variables $b_1 \dots b_6$ in equations 3.10 and 3.11.

experiment is not accepted since all the data points are in the first quadrant, which violates the third criterion. In summary, the first criterion assesses the shape of the hysteresis, the second one the non-piezoelectric influence, and the third one decides if genuine FE switching occurs.

The response curve of an SS-PFM experiment comprises the most characteristic properties of local FE switching. The hysteresis loop, as illustrated in figure 3.7b, can be modelled by two sigmoid functions with a linear term. The forward (\mathbf{R}^+) and reverse (\mathbf{R}^-) branch are defined as follows:

$$R^+ = a_1 - a_2 \cdot \left(1 + \exp\left(\frac{V - a_3}{a_5}\right) \right)^{-1} + a_6 \cdot V \quad (3.13)$$

$$R^- = a_1 - a_2 \cdot \left(1 + \exp\left(\frac{V - a_4}{a_5}\right) \right)^{-1} + a_6 \cdot V. \quad (3.14)$$

Both branches are simultaneously fitted by using the `optimize.curve_fit` function from Scipy in Python 3. The R^2 value of this fit serves as the third filter. If it is below **0.9**, the curve is not used for further evaluation. The boundary conditions of the fitting parameters $\mathbf{a}_1 \dots \mathbf{a}_6$ are listed in table 3.5. If a measurement passes all three stages of filtering, three characteristic parameters are extracted from the response hysteresis loop as illustrated in figure 3.7b: the Coercive Bias (\mathbf{V}_f), the Saturation Response (\mathbf{R}_{fs}), and the effective Work of Switching parameter (\mathbf{A}_{fs}). The first corresponds to the minimum bias necessary to cause a change of polarization beneath the tip and the second is the maximum response in the saturation regime. The third can be considered a robust parameter to describe the local FE switchability of a material. If the contact properties between the tip and surface change, the Coercive Bias raises and the Saturation Response shrinks or vice versa, which impedes the comparison of curves obtained from different spots on the surface and practically prevents the comparison between different samples. However, the area between the forward and reverse branches is not affected by the change in contact properties, making the effective Work of Switching parameter a proper candidate for the comparison of polarization switching dynamics [82]. All three parameters can be derived from the response hysteresis loop as follows:

$$V_f = \frac{|V_f^+ - V_f^-|}{2} = \frac{|a_3 - a_4|}{2} \quad (3.15) \quad R_{fs} = \frac{|R_{fs}^+ - R_{fs}^-|}{2} = a_2 \quad (3.16)$$

$$A_{fs} = \int_{-\infty}^{\infty} [R^+(V) - R^-(V)] dV = a_2 \cdot |a_3 - a_4|. \quad (3.17)$$

DART SS-PFM experiments yield two AmpOff and two AmpOn response curves as a consequence of two simultaneously acquired phases. In the case that both hysteresis loops of AmpOff or AmpOn are accepted by the filter, the value pairs of the derived characteristic parameters are averaged. Since 36 SS-PFM experiments are conducted per temperature, the extracted parameters from the accepted response hysteresis loops are averaged as well for the temperature-dependent evolution of \mathbf{V}_f , \mathbf{R}_{fs} , and \mathbf{A}_{fs} . For completeness, the percentage of curves accepted by the filter is also displayed in the temperature-dependent evolution.

Variable	Lower	Upper
a_1 [pm]	$\min(R_j)$	$\max(R_j)$
a_2 [pm]	0	∞
a_3 [V]	-50	50
a_4 [V]	-50	50
a_5 [V]	$-\infty$	∞
a_6 [pm/V]	$-\infty$	∞

Table 3.5: Response fit – boundaries of the variables $a_1 \dots a_6$ in equations 3.13 and 3.14.

4 Results and discussion

The results are grouped by the four investigated material systems: BT, BZT, BNT, and BNZT. Every group is divided into four parts: First, the microstructure of the samples is presented with the main focus on the grain size. Coarse-grained samples were imaged with OM and finer-grained samples were imaged using contact-AFM. Next, the (ideally) pristine domain structure of the freshly polished samples, obtained via SF-PFM, is discussed. Then the results of the polarization switching experiments are presented. The last part addresses the local, temperature-dependent dynamics of the polarization-switching process by reviewing the SS-PFM experiments. In the last section of this chapter, conclusions are drawn from the results to answer the three questions of this thesis raised in chapter 1.

4.1 BT-System

The polycrystalline BT sample represents the model FE state and serves as a reference material for comparison with the BZT, BNT, and BNZT systems. The AD and PD of the PFM domain structure scans as well as the results of the SS-PFM experiments of BT are also present in the results of the other systems for better comparability.

4.1.1 Microstructure

An OM image of the microstructure of BT is displayed in figure 4.1. The coarse grains are up to 200 μm in size. Consequently, the domain structure is of herringbone type with a complicated arrangement of 180° and 90° domains at RT. The lamellae are also visible in the OM image, indicating domain-selective material removal during the final polishing step with the OP-S solution; a consequence of the different etching rates at the positive and negative ends of the domains [85]. The microstructure is dense and contains few large pores, comparable to the crystals in size, as well as smaller pores located inside the crystals. The larger pores can be avoided by the proper choice of the AFM's measurement area, however, the smaller pores are unavoidable due to their uniform distribution across the whole microstructure.

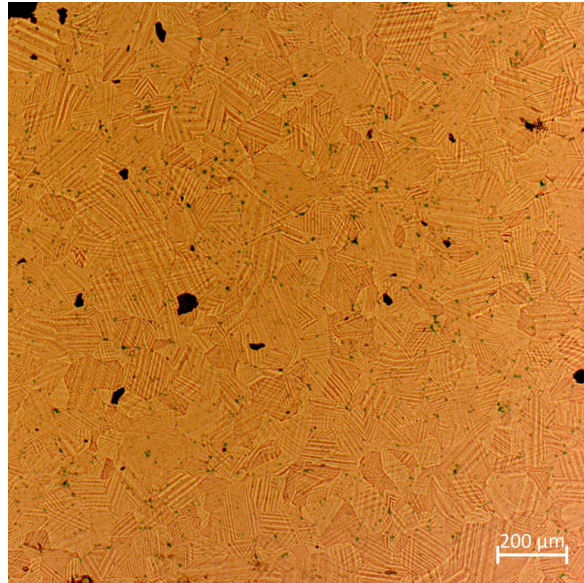


Figure 4.1: BT - Microstructure. The coarse grains (up to 200 μm in size) were imaged with OM.

4.1.2 Domain structure

The sophisticated domain structure of BT can be obtained via careful conduction of SF-PFM, as illustrated in figure 4.2. The herringbone structure is present in the topography (4.2a), amplitude (4.2b), and phase (4.2c) image of the scan. However, while the topography image can only provide information about the size of the domains, the amplitude and phase provide insight into the local orientation of the polarization vector of the FE domains. The phase image reveals

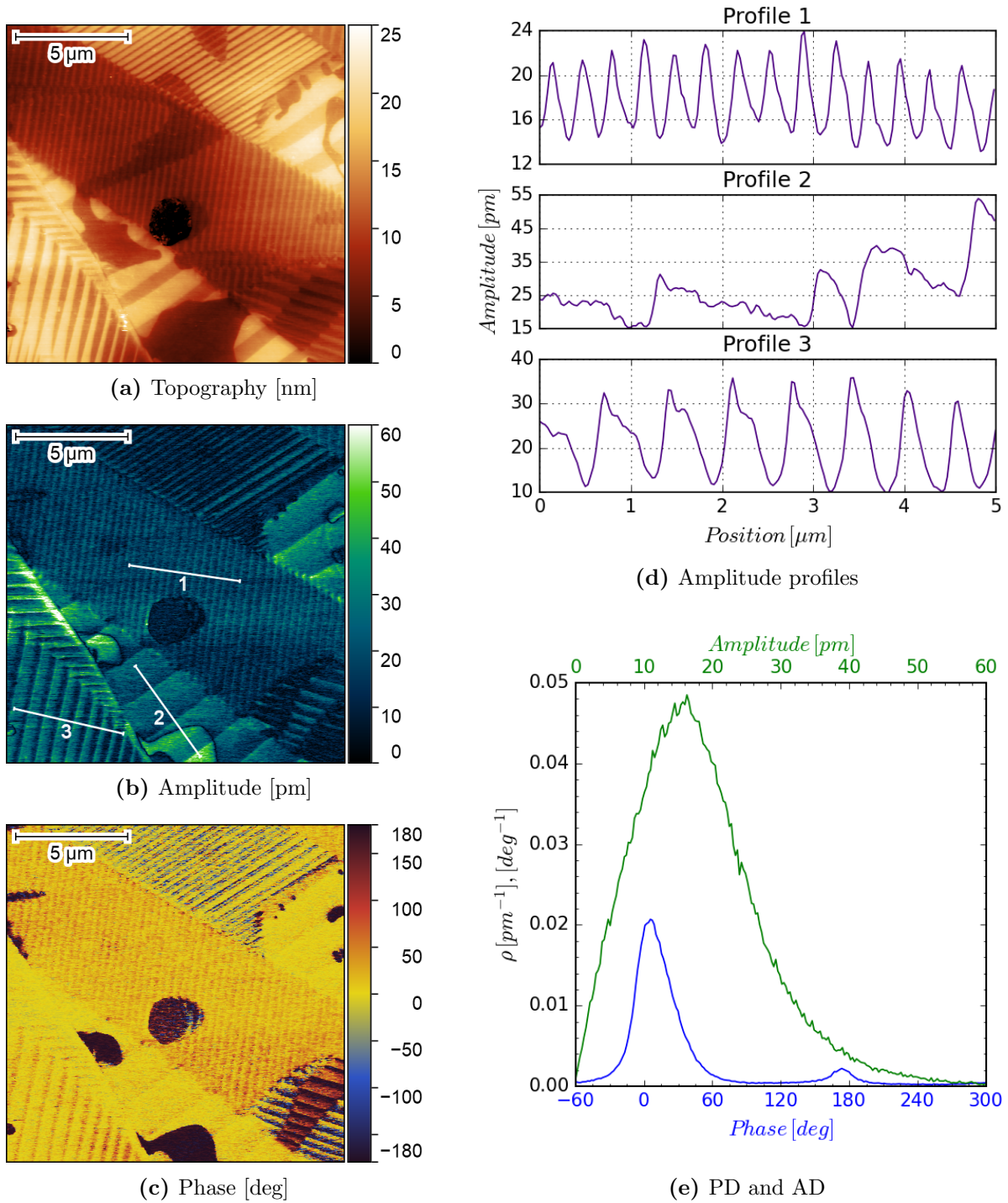


Figure 4.2: BT - Domain structure. The herringbone-type domain structure is visible in the topography (a), amplitude (b), as well as in the phase image (c). The width of the lamellae ranges from 300 nm to 2 μm , derived from the amplitude profiles in (d), which are indicated by the lines in (b). The AD and PD (e) are monomodal and bimodal, respectively.

the orientation of the vertical part of the piezoresponse, whereas the amplitude contains the magnitude of the piezoresponse. The phase image exhibits domains with phase values of either 0° or 180° , ideally corresponding to up and down vertical polarization. It can be assumed that the lamellae comprise domains with both 90° and 180° domain walls, as not every lamellar structure exhibits vertical PFM phase contrast of $\pm 180^\circ$. One indicator for real vertical (lateral) PFM

contrast in FEs is a vanishing amplitude in the vicinity of a domain wall between domains with antiparallel out-of-plane (in-plane) polarization. This emerges from the destructive interference of the anti-phase oscillations of adjacent antiparallel domains. The amplitude image exhibits this indicator at almost all 180° domain walls, indicating genuine PFM contrast originating from ferroelectricity. The three profiles extracted from the amplitude image reveal lamellae widths ranging from 300 nm to 2 μm . The AD is monomodal with a peak at 16 pm and the PD is bimodal with peaks at 5° and 173° . The bimodal PD with a difference of nearly 180° is another indicator of genuine PFM contrast emerging from ferroelectricity.

BT exhibits tetragonal crystal symmetry at RT. Hence, 6 polarization orientations along the $\langle 001 \rangle$ crystallographic directions are possible. Switching of polarization occurs via the rotation of the polarization vector by either 180° (FE switching) or 90° (ferroelastic switching). While the former does not involve a change in the lattice parameters, the latter is accompanied by a change in the long axis of the tetragonal unit cell. This leads to localized strain in the switched areas. An example of such a ferroelastic switching process is displayed in figure 4.3. Comparing the topography (cf. figure 4.3a) and response (cf. figure 4.3c) image reveals the traces of a domain that was still present during the polishing procedure. However, the polarization of this domain appears to have switched after the last polishing step in order to adapt to the polarization state of the surrounding domain, since the (former) inner and outer domain cannot be discriminated in the response image. The response profile in figure 4.3b has a uniform pattern, but the topography profile exhibits a step of approximately 5 nm. This is direct proof of ferroelastic switching, accompanied by local strain emerging from the change of the long c -axis. According to figure 2.8a, the c -axis is shortened by roughly 4.5 pm during a ferroelastic switch. Therefore, the height change of 5 nm is caused by the correlated switching of at least 1000 unit cells. Translated to actual length scales, this would mean that the domain had a depth of 450 nm (assuming a c -axis length of 404 pm), comparably low to the lateral extent of the surrounding domain, which implies why this domain could not sustain after polishing.

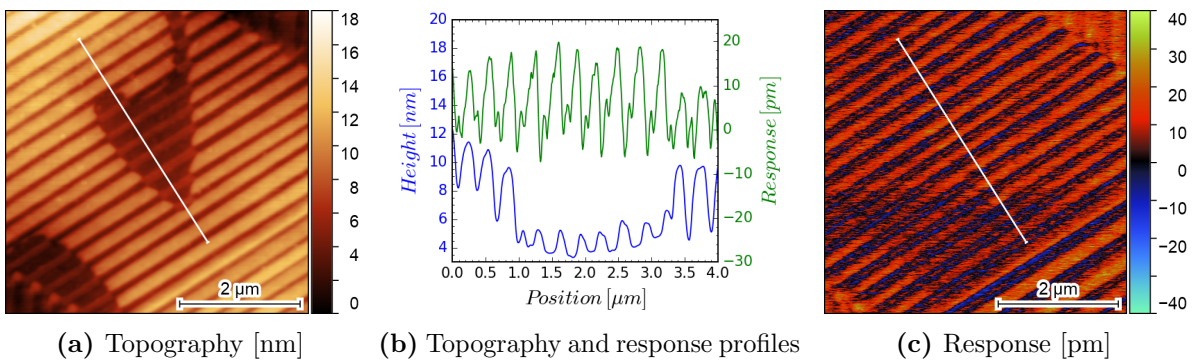


Figure 4.3: BT - Ferroelastic switching after sample preparation. The topography (a) and response (c) images as well as their corresponding profiles along the white lines (b) suggest that the inner domain performed a ferroelastic switch in order to adapt the surrounding domain structure.

The measured out-of-plane signal of vertical PFM is often not exclusively comprised of vertical piezoresponse, but also includes a lateral contribution. The local lateral deformation can lead to cantilever buckling, which is detected as a vertical PFM signal, albeit the deformation is strictly

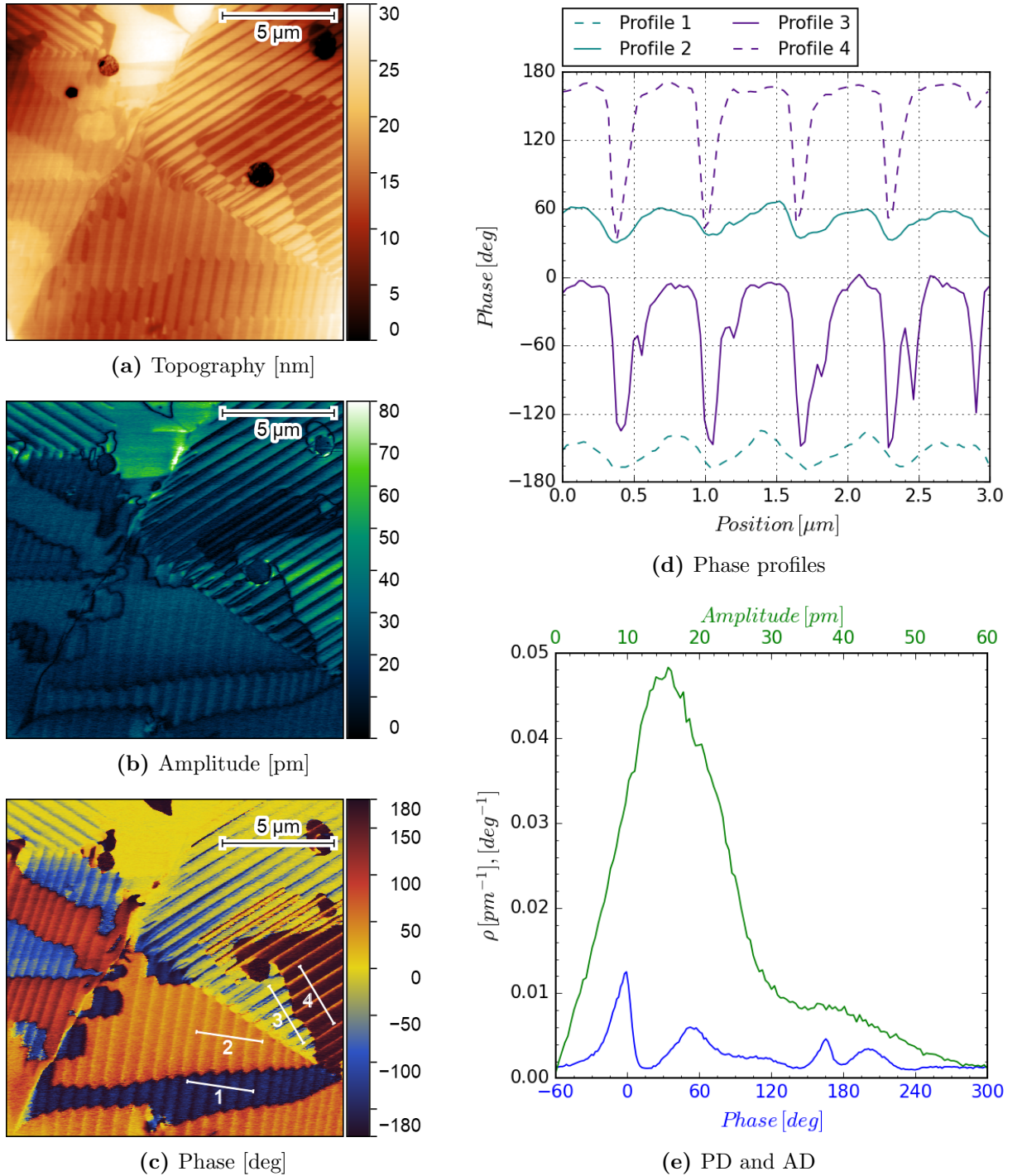


Figure 4.4: BT - Influence of the lateral contribution to the vertical PFM signal. A comparison between "up" or "down" domains reveals a phase difference in the twin grain (cf. (c) and (d)), emerging from the cantilever buckling and induced by the in-plane oscillation of the domain. Consequently, the phase exhibits a multimodal distribution with four peaks (e). The four domains are visible in the topography (a) and amplitude (b) image as well.

in-plane [86]. As a consequence, the measured phase and amplitude can be significantly altered by that contribution, even leading to misinterpretation of the vertical polarization component. Separating the in-plane from the out-of-plane contribution necessitates a sophisticated calibration procedure [87], which was not conducted in this thesis. The SF-PFM experiment displayed in

figure 4.4 is a good example of this type of artefact. The phase image (cf. figure 4.4c) and the associated profiles (cf. figure 4.4d) reveal the influence of the lateral contribution on the phase of the signal. Even though profiles 1 and 4 correspond to vertical piezoresponse pointing upwards, they exhibit a difference in phase of 45° . This effect is even larger in the domains pointing downwards (cf. profile 2 and 3), with 60° of phase difference. These phase shifts also influence the PD, as illustrated in figure 4.4e. The distribution is multimodal, with four rather clear peaks at roughly 0° , 53° , 165° , and 202° . Note that a phase of 202° is equivalent to -158° . This artefact is not present in the measurement displayed in figure 4.2, which suggests that a certain mutual arrangement of adjacent domains is required to obtain it.

4.1.3 Polarization switching

The results of the polarization switching experiment are displayed in figure 4.5. The subfigures 4.5a, 4.5b, and 4.5c, show the response of the unpoled, poled ($V = -50$ V), and partially relaxed structure (after 117 h). The target size of the poled area is $10 \mu\text{m} \times 10 \mu\text{m}$. However, the actual poled area is slightly larger as the actual length of a scan line is larger than the saved part in the image, which results in a broadening of the poled area in the scan direction. Polarization switching was successful throughout the whole target area, and it remained partially stable for at least 117 h. The partial relaxation can be attributed to the system's drive to minimize the

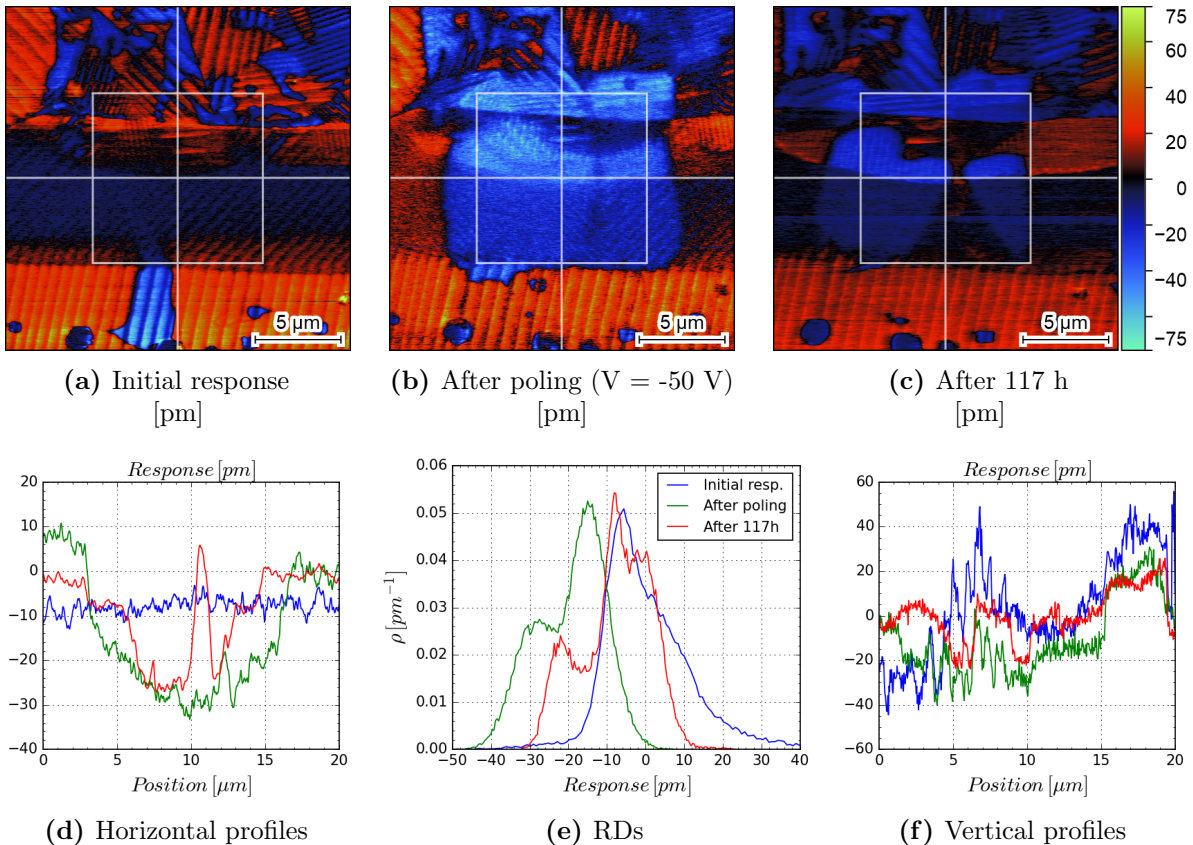


Figure 4.5: BT - Polarization switching experiment. The PFM response in (a) displays the pristine domain structure and (b) the response after poling with -50 V. The third scan (c) covers the same spot, 117 h after poling. Figure (d), (e), and (f) are the horizontal profiles (marked by the white horizontal lines), RDs (data extracted from within the squares), and vertical profiles (marked by the white vertical lines). The poled area was $10 \mu\text{m} \times 10 \mu\text{m}$ in size, as indicated by the white square.

elastic and electrostatic energy, as indicated by the remaining lamellar pattern in the poled area. The change in polarization is confirmed by a change of sign in the horizontal (cf. figure 4.5d) as well as the vertical (cf. figure 4.5f) profiles. Furthermore, the RD of the target area (all data points within the square are taken into account) in figure 4.5e is strongly shifted towards negative response values, and the shape changes from an unimodal to a bimodal distribution. After relaxation, the RD is slightly shifted back towards more positive values, but the bimodal shape remains. Note that the apparent switch of polarization in the opposite direction left and right to the square occurred due to a precedent polarization switching attempt in the same area with positive bias. Summarized, the presented data in figure 4.5 confirms FE switching in BT, a prerequisite for true ferroelectricity [88].

4.1.4 SS-PFM

The SS-PFM results are displayed in figure 4.6. The graphs on the left exhibit the characteristic parameters from the hysteresis loops that were acquired during the poling pulse (AmpOn) and the graphs on the right present the same parameters for the field-free case (AmpOff). Special focus will be laid on the Work of Switching parameters as well as on the Acceptance Rate of the filter algorithm introduced in section 3.5.2. The Coercive Bias and Saturation Response serve as complementary parameters and will only be addressed if ambiguities in the Work of Switching parameters occur since these parameters are prone to alteration by changing contact properties between the AFM tip and sample. In general, the AmpOn Work of Switching parameter is higher than the AmpOff. This can be explained by the additional electrostrictive and electrostatic contribution, which is negligible in the field-free case. After an initial decline, the Work of Switching parameters of AmpOn and AmpOff increase with rising temperature until they reach their maximum at 130 °C, which is in the temperature range of the reported Curie temperature of BT. Upon further heating, there is a steep decline of A_{fs} . This sudden drop is a direct proof of an ongoing FE-PE PT. Similar experiments in the FE community confirm this assumption [89, 90]. A closer look at the Acceptance Rate reveals another discriminating feature between AmpOn and AmpOff. While the Work of Switching parameter drops for both cases, a drop in the Acceptance Rate is only present in the AmpOff evolution. This can be explained as follows: the phase transition of BT is of mixed type with a dominant displacive and but also non-negligible order-disorder contribution. Consequently, most of the remaining FE clusters are not stable enough to remain in a state of uniform polarization in the field-free case, resulting in a steady decline in the accepted AmpOff curves. However, since there are still (disordered) dipoles present above T_C , a temporary, field-stabilized alignment is still possible, leading to an electromechanical response and hysteresis loops in AmpOn.

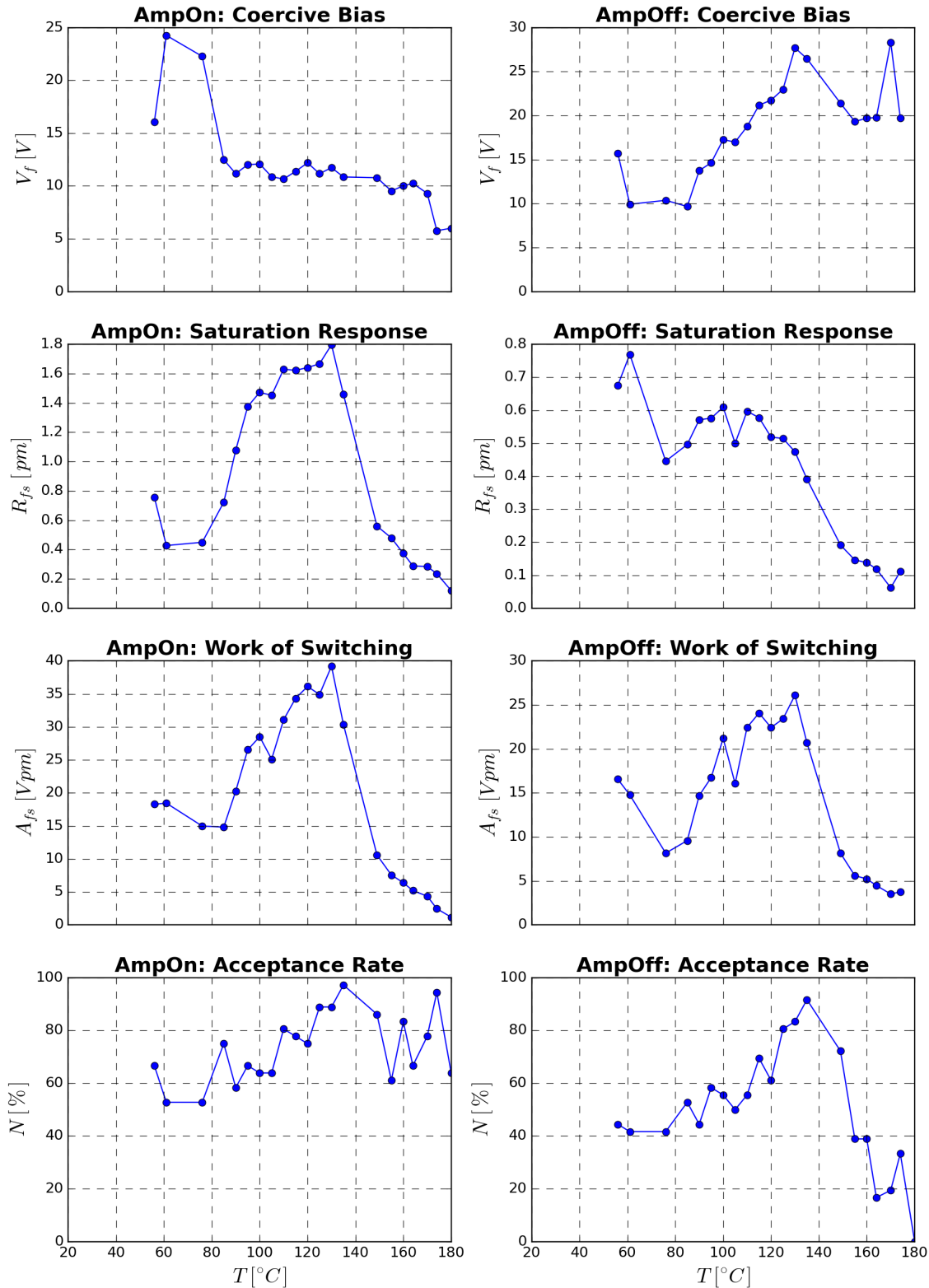


Figure 4.6: BT - SS-PFM results. The graphs display the temperature-dependent evolution of the Coercive Bias, Saturation Response and Work of Switching parameter from the fitting procedure (cf. equations 3.15, 3.16 and 3.17), as well as the Acceptance Rate from the filters described in section 3.5.2, for AmpOn and AmpOff. BT exhibits a phase transition at 130 $^{\circ}\text{C}$, which is marked by a sharp drop of the AmpOn and AnpOff Work of Switching parameter as well as the AmpOff Acceptance Rate of the filter.

4.2 BZT-System

For this system, four different compositions were investigated by PFM: 10% Zr (BZT_10), 20% Zr (BZT_20), 30% Zr (BZT_30), and 40% Zr (BZT_40). The sample with 30% Zr is not included in the SS-PFM results due to unexplained problems with the acquisition of the hysteresis loops.

4.2.1 Microstructure

The four samples exhibit a significantly different microstructure compared to each other, as is illustrated in figure 4.7. The sample with 10% Zr (cf. figure 4.7a) has coarse grains with roughly 50 μm in size. The dense microstructure contains pores significantly smaller than the grains and the domain structure is not visible in the OM image. The sample with 20% Zr (cf. figure 4.7b) exhibits a clearly bimodal grain size distribution, that comprises coarse grains up to 100 μm in size, with considerably smaller grains (between one and two orders of magnitude smaller) filling the voids between them. The majority of the pores are located in the vicinity of the smaller grains. A similar, but not as strongly pronounced microstructure can be obtained for the sample with 30% Zr (cf. figure 4.7c). Coarse grains comparable in size to the former sample and finer grains, roughly one order of magnitude smaller, coexist in the microstructure. The pores are considerably larger compared to the other samples. Furthermore, twin crystals appear to be present in the microstructure. The sample with 40% Zr (cf. figure 4.7d) exhibits a dense and fine-grained microstructure with grains predominantly smaller than 5 μm .

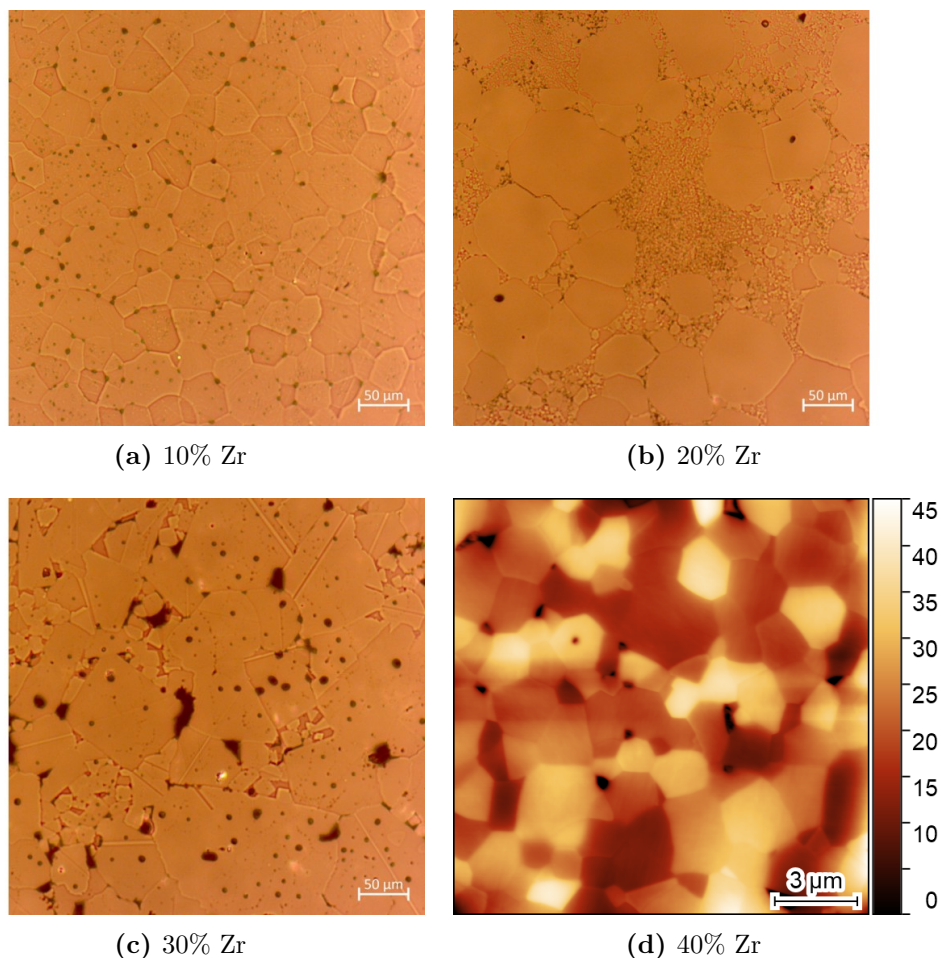


Figure 4.7: BZT - Microstructure obtained by OM (a, b, c) and contact-AFM (d).

4.2.2 Domain structure

The domain structure of the sample with 10% Zr is displayed in figure 4.8. Like in pure BT, there is a clear correlation between the topography (cf. figure 4.8a), amplitude (cf. figure 4.8b), and phase (cf. figure 4.8c) image. In the vicinity of domain walls, the amplitude exhibits a minimum, which is an indicator of a genuine PFM contrast. Furthermore, the amplitude is uniform within the domains with little noise. The phase image exhibits three dominant values, namely 0° , -180° , and -90° . The latter value is only obtained in the grain at the lower right rim of the image. The bimodal PD (cf. figure 4.8d, blue line) exhibits peaks at -10° and 187.5° . The AD (cf. figure 4.8d, green line), on the other side, is trimodal with peaks at 16 pm, 55 pm, and 74 pm, which can be explained by the orientation-dependent amplitude of the large individual grains. The peak at 74 pm corresponds to the high-amplitude grain in the lower part of the picture, whereas the peak at 16 pm corresponds to the small grain in the centre and the grain at the lower right rim of the image. The most dominant peak at 55 pm is caused by the remaining grains of the

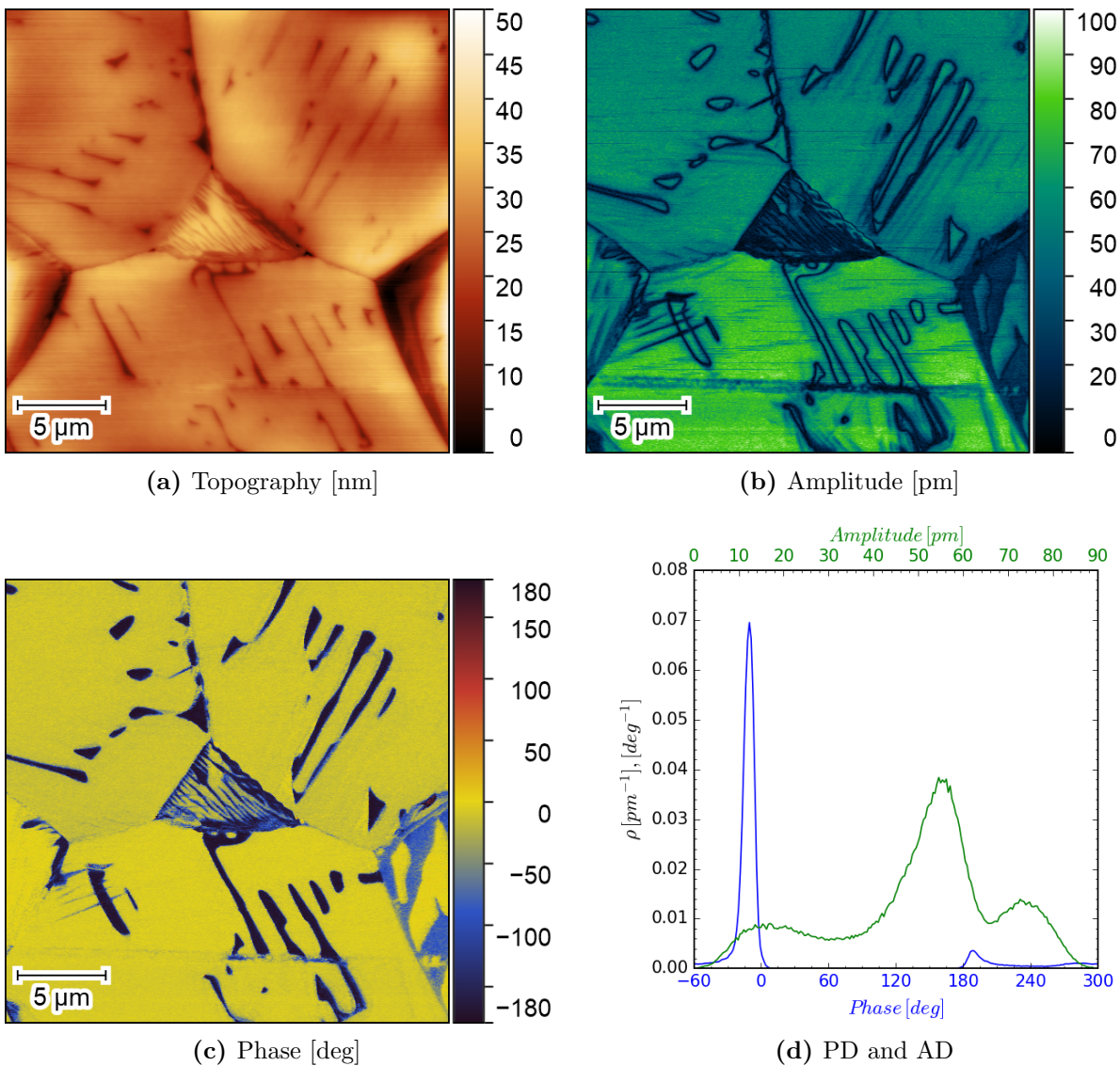


Figure 4.8: BZT (10% Zr) - Domain structure obtained by PFM; (a), (b), (c), and (d) are the topography, amplitude, phase and the combined AD-PD, respectively. The images exhibit all indicators for genuine PFM contrast emerging from ferroelectricity.

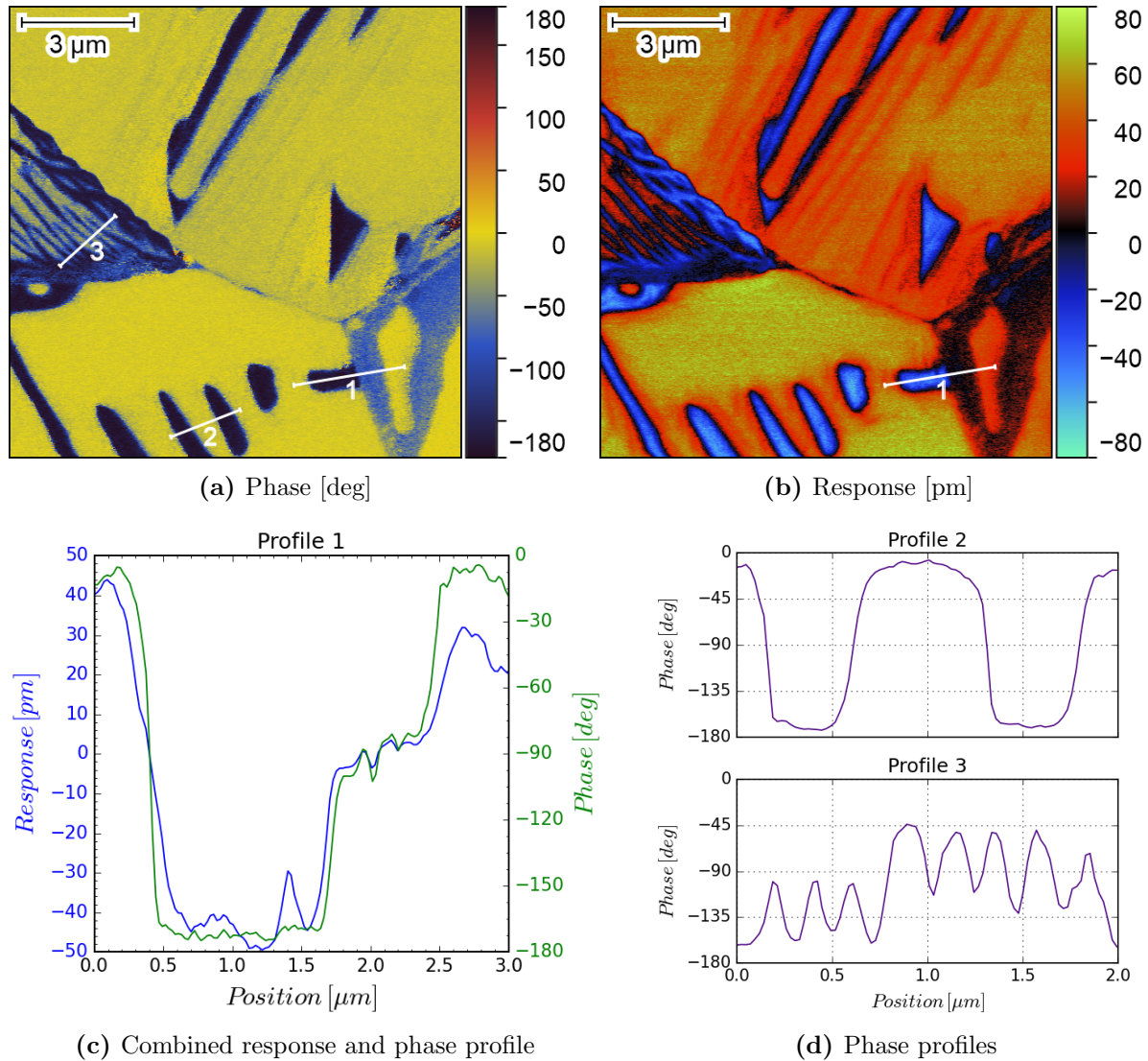


Figure 4.9: BZT (10% Zr) - Magnified domain structure obtained by a $12\ \mu\text{m} \times 12\ \mu\text{m}$ PFM measurement. The response and phase image are displayed in (a) and (b). Their respective profiles, marked by white lines, are displayed in (c) and (d).

image. There appears to be an inverse correlation between the number of domain walls within grains and the width of their respective peak in the AD. In general, the domains are of lamellar type, although they appear to be intercepted in larger grains. A comparison of the topography and phase image suggests that some domains shrank after the polishing procedure. Some of the lamellae in the phase image appear to be smaller than in the topography image, and numerous of the smaller ones even vanished completely. A magnified scan in the same area is displayed in figure 4.9. The phase image (cf. figure 4.9a) and profiles 2 and 3 (cf. figure 4.9d) reveal lamellae widths of approximately 500 nm and 100 nm for the large and small grains, respectively. Profile 1 in figure 4.9c illustrates a similar case as described in figure 4.4, where the lateral contribution significantly alters the measured vertical phase. It appears that a strong lateral contribution can rotate the complex PFM vector by a large angle, in this case by $\pm 90^\circ$. Consequently, the response in these areas of the scan is almost zero, as illustrated by the white lines with the number 1 in the lower right of figures 4.9a, 4.9b and their corresponding profiles in figure 4.9c [86, 87]. BZT₁₀ should exhibit rhombohedral crystal structure at RT according to figure 2.11a.

In addition, XRD [91] and Raman [92] experiments suggest FE behaviour in this composition. It can be stated that the system clearly exhibits a spontaneous polarization that can be detected by PFM.

For the sample with 20% Zr (BZT_20), the disrupting effect of higher substitution is already visible, as illustrated in figure 4.10. While there is still contrast in the amplitude figure (cf. figure 4.10b), only negligible phase contrast can be detected (cf. figure 4.10c). This is further confirmed by the two profiles in figure 4.10d (marked by the white lines in figures 4.10b and 4.10c), with

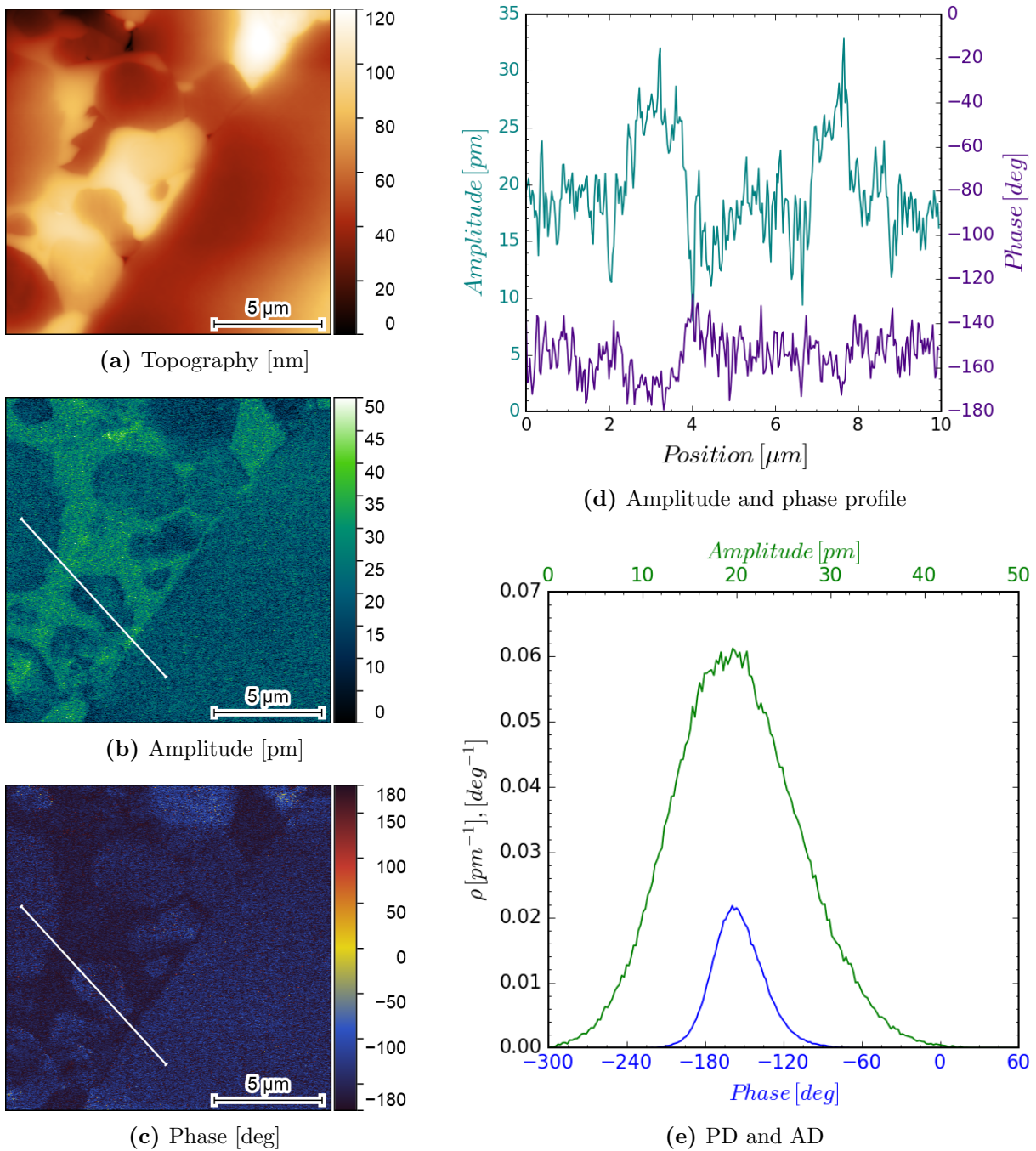


Figure 4.10: BZT (20% Zr) - Domain structure obtained by PFM. While there is still contrast in the amplitude image (b), only minor contrast is visible in the phase image (c). This is further confirmed by the profiles (d) and distributions (e) of phase and amplitude. The topography image (a) partially coincides with the two PFM images.

clear changes in the amplitude, but negligible ones in the phase. As expected, the PD and AD are both monomodal with peaks at -145° and 19 pm, respectively (cf. figure 4.10e). However, if the stimulation frequency is at the contact resonance frequency, distinct PFM contrast can be obtained, as illustrated in figure 4.11. Note that the abrupt change in contrast in figure 4.11b is caused by a significant shift of the resonance frequency due to changes in the contact properties between tip and sample. One explanation for the weak contrast in figure 4.11c compared to figure 4.11b could be a dominant electrostatic contribution, possibly originating from a strongly increased or decreased surface potential [93]. This undesired contribution should become more negligible at resonance, since resonance PFM yields a higher piezoresponse than off-resonance PFM. Therefore, a DART-PFM scan was conducted at a spot that partially includes a large grain and numerous small grains (cf. figure 4.12). A clear correlation between the topography image (cf. figure 4.12a) and the response images of the three consecutive scans (cf. figure 4.12b, 4.12c, and 4.12d), each taking approximately 30 minutes, can be obtained. Many of the grains appear to be single-domain due to their uniform response, with some exceptions, e.g. in the green encircled area 3. The three consecutive response images reveal a dynamic behaviour of the domains in this sample. In area 1, the polarization is uniform in the whole grain, but in the next scan, a new domain nucleated in the centre, which shrank again in the consecutive scan. In area 2, the changes are even more pronounced. A great majority of the domains appear to have switched after the second scan. However, many have apparently reversed again after the third scan. The domain in area 3 exhibits a full switch during the three consecutive scans in order to adapt to the surrounding polarization state. One detail of importance is that this spontaneous domain-switching behaviour can also appear in the larger grains of this system. The magnitude of the response suddenly increases almost five-fold in the middle of the second scan (cf. figure 4.12c), which is most likely attributed to a change of contact properties between tip and sample. The results suggest that the domain structure of BZT₂₀ is highly dynamic and unstable. However, it is unclear if this dynamic behaviour of the domains is an inherent feature of the system, or if it is (partially) mediated by the tip's pressure on the surface or the stimulating AC bias. In addition, the domains can only be obtained in DART-PFM, which suggests the presence of additional non-piezoelectric interactions between tip and surface, caused by e.g. strong electrostatic interactions. Such additional contributions can be considered an artefact of the AFM's optical beam deflection method, which can be avoided by using a more quantitative method for measuring the cantilever displacement, e.g. an interferometric displacement sensor

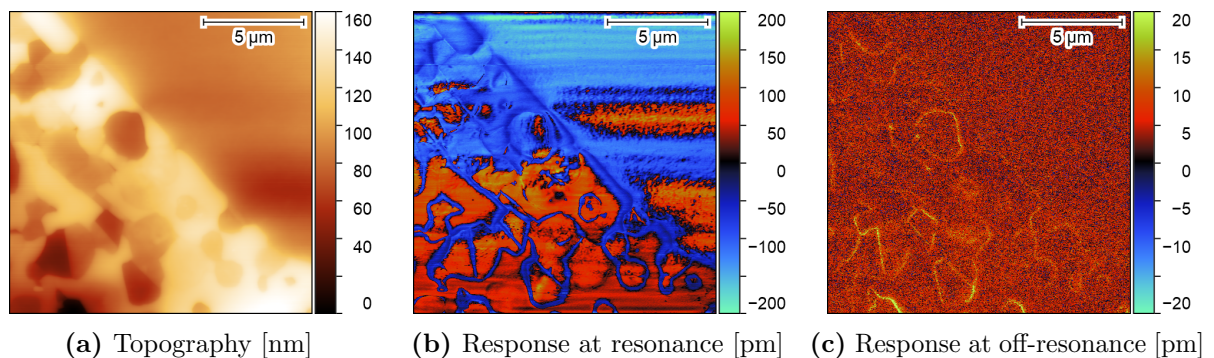


Figure 4.11: BZT (20% Zr) - Domains imaged in resonance (b) and off-resonance (c) mode. The topography of the scanned area is displayed in (a).

[94, 95]. A closer look at the phase diagram in figure 2.11a reveals that at RT, the system is very close to its transition temperature T_m . Various sources report values for T_m between 11 °C and 37 °C and furthermore, the presence of FE clusters above T_m can be assumed [43, 92, 96]. A coexistence of rhombohedral and cubic symmetry above T_m was reported as well, which consolidates this statement.

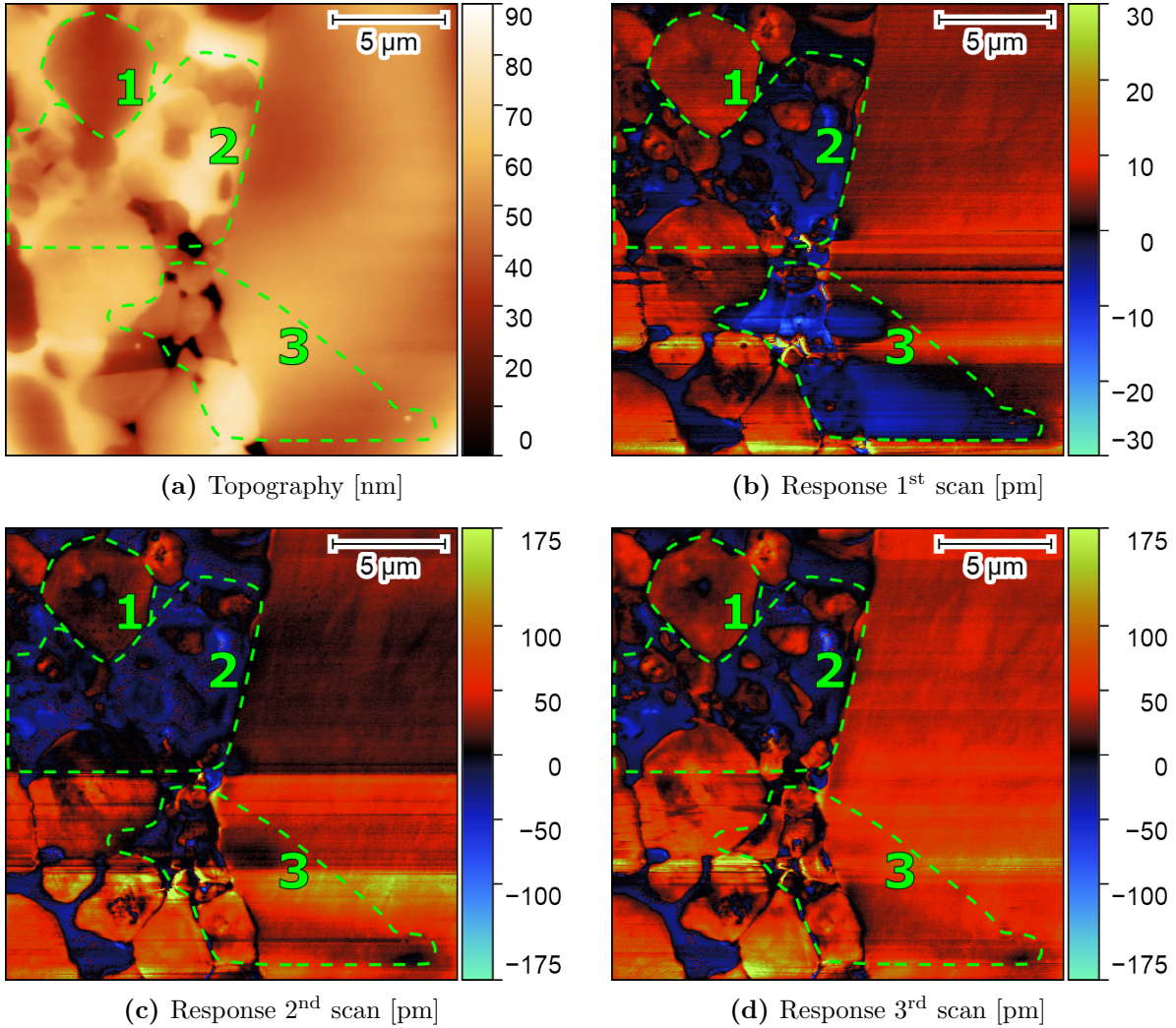


Figure 4.12: BZT (20% Zr) - DART scan of the dynamic domain structure. The topography (a) and the response images of three consecutive scans (b, c, d) reveal an apparent change in the domain structure. The changes are most significant in the green-encircled areas. The dashed lines serve solely as guidance lines.

Raising the substitution level to 30% leads to the suppression of any long-range FE order, as illustrated in figure 4.13. The microstructure exhibits nearly uniform amplitude and a noisy phase (cf. figures 4.13b and 4.13c). Both the AD and broad PD (cf. figure 4.13d) are monomodal with peaks at 7 pm and 135°. It appears that there is minor PFM contrast in the vicinity of some grain boundaries. An explanation of this effect could be an additional electromechanical contribution emerging from dipoles in the symmetry-broken grain boundary region or topographic crosstalk [97]. Summarized, BZT₃₀ does not exhibit a detectable spontaneous polarization. According to figure 2.11a and supporting literature [41, 96], BZT₃₀ is an ER at RT with randomly distributed dynamic PNRs. However, the PNRs cannot be resolved by PFM, which can be explained by a lack of stability and/or the lateral resolution limit of PFM [55, 77].

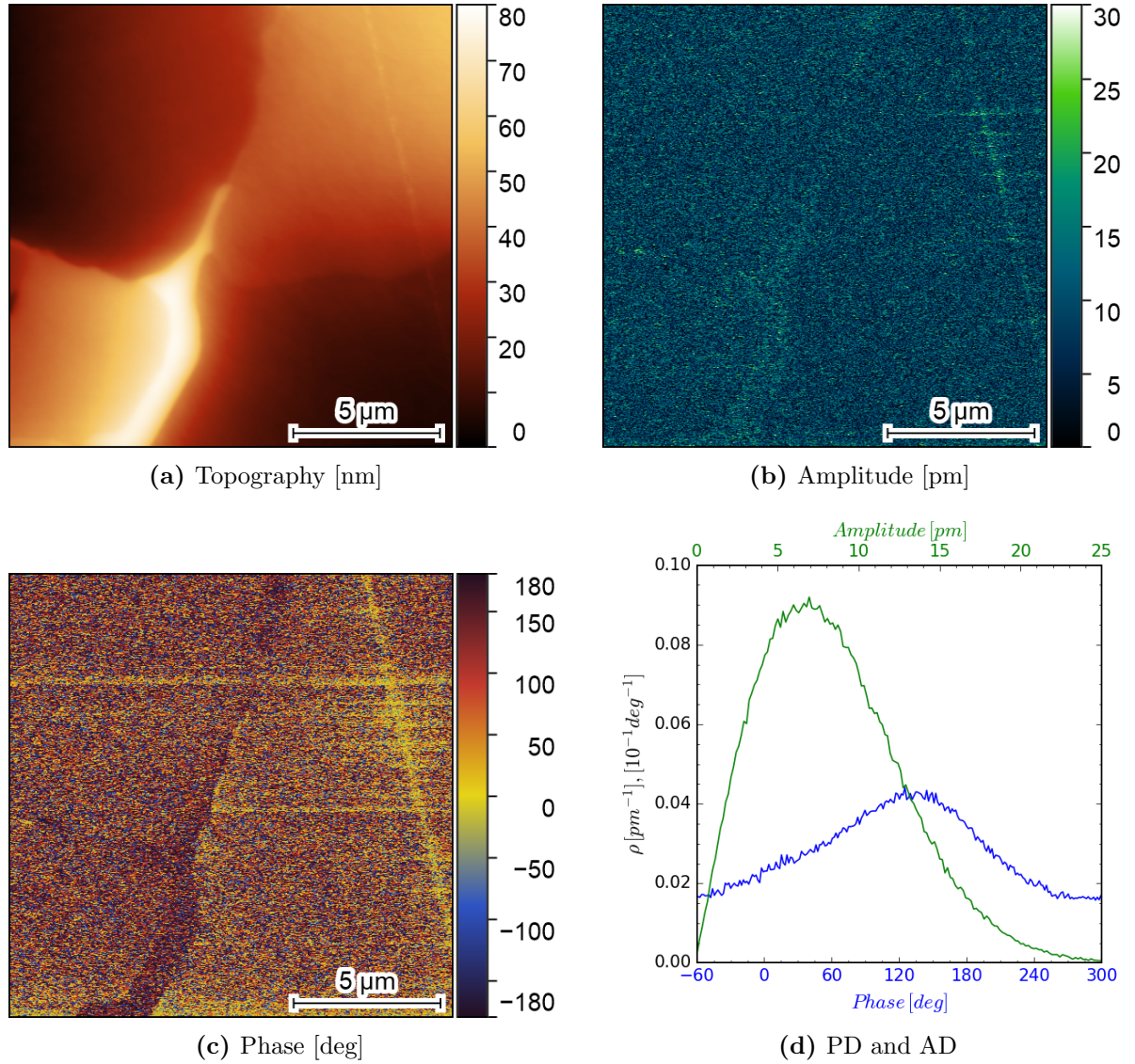


Figure 4.13: BZT (30% Zr) - Domain structure. The measurement exhibits only weak contrast in the amplitude (b) and phase (c) image, which is also confirmed by the two distributions in (d). The topography is displayed in (a).

A substitution level of 40% Zr does not cause any significant changes to the system (cf. figure 4.14). Neither from the amplitude image nor from the phase image, a domain structure can be derived (cf. figures 4.14b and 4.14c). There is also no correlation between the topography (cf. figure 4.14a) and the PFM signal. Both the AD and PD in figure 4.14d are monomodal with their respective peaks at 14 pm and -45° . BZT₄₀ is considered an ER at RT with an average cubic structure. However, PDF analysis suggests that local polar clusters with rhombohedral symmetry are present in the crystals as well [91]. Summarized, no long-range FE order can be obtained in this sample.

Figure 4.15 depicts the ADs and PDs of the SF-PFM experiments of all BZT samples. One striking detail about the ADs is the significantly larger amplitude of BZT₁₀ compared to BT. The rhombohedral crystal structure in BZT₁₀ is a possible explanation for this enhanced electromechanical response, since a total of eight discrete polarization directions is possible, in contrast to the six possible directions in tetragonal BT. BZT₂₀ and BZT₄₀ exhibit a comparable amplitude to BT, implying that further substitution does not increase the piezoresponse. BZT₃₀

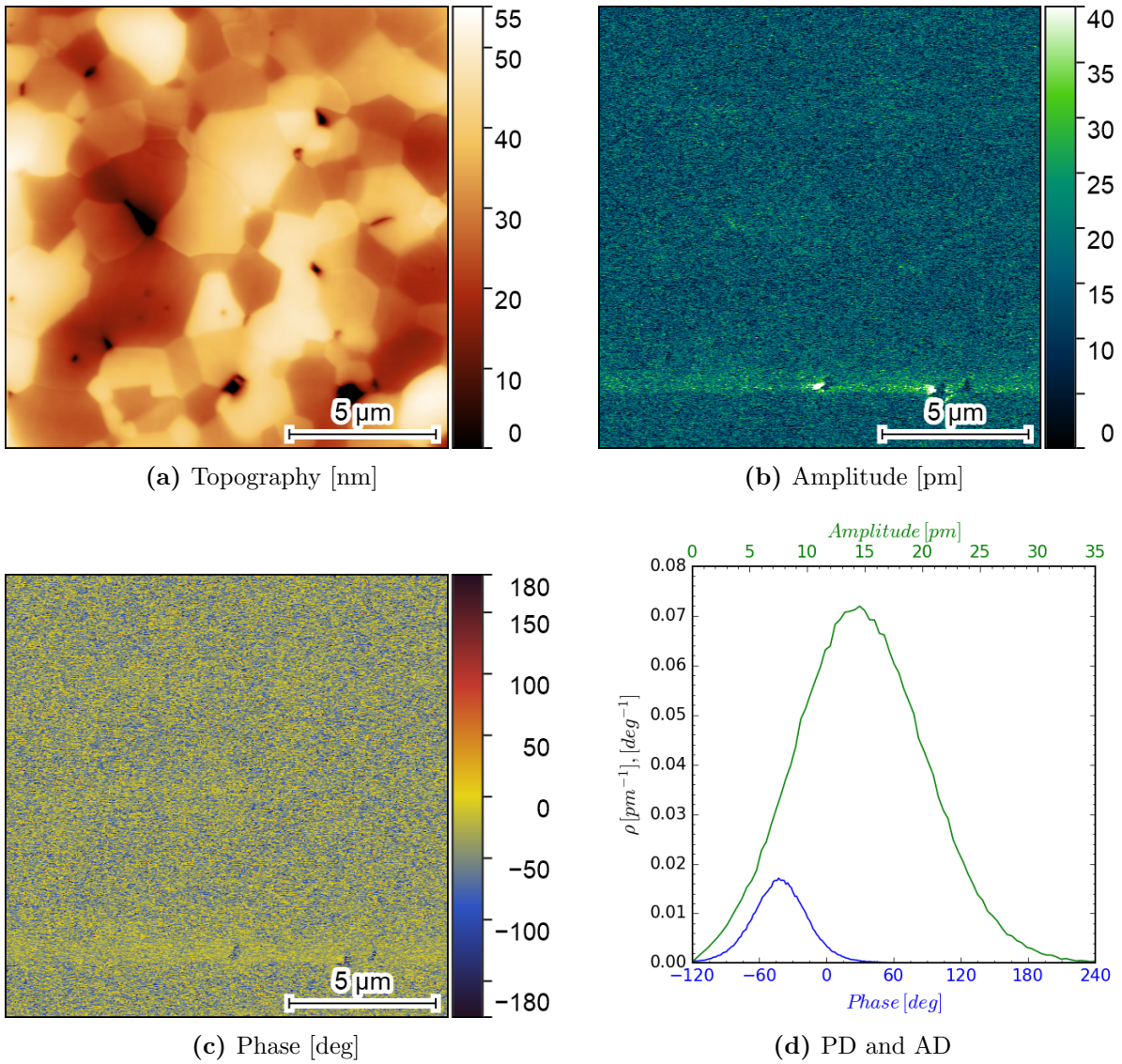


Figure 4.14: BZT (40% Zr) - Domain structure. The measurement exhibits almost no contrast in the amplitude (b) and phase (c) image, which is confirmed by the two distributions in (d) as well. The topography is displayed in (a).

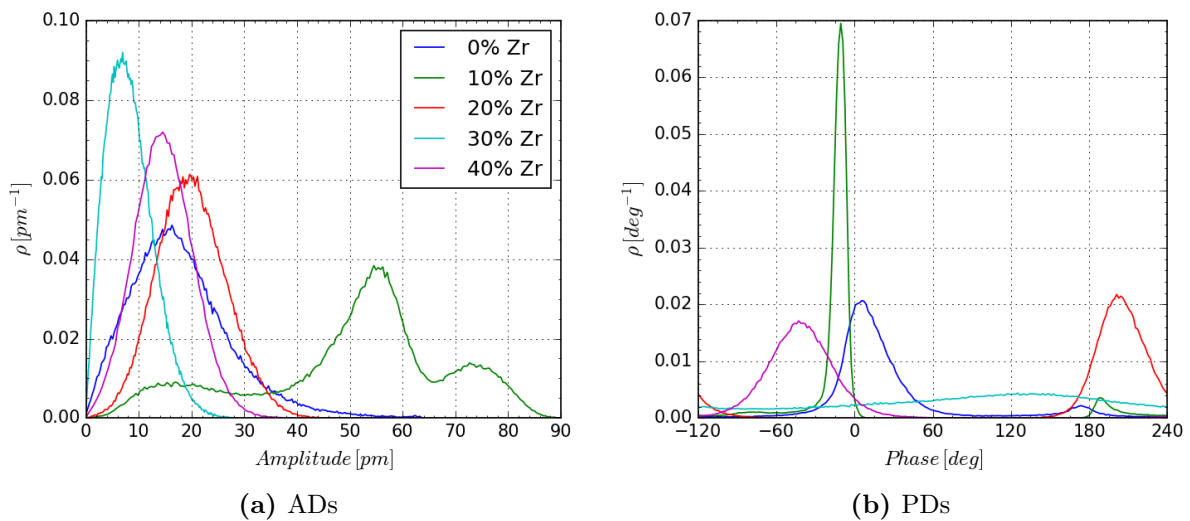


Figure 4.15: BZT - Summary of the SF-PFM results. The ADs are displayed in (a) and the PDs in (b).

exhibits the lowest response of all samples, which could be an inherent property of the material composition or related to a circumstantial orientation of the four grains, that yields a weak out-of-plane PFM signal. For the PDs, only BT and BZT_10 exhibit a bimodal distribution, the rest are monomodal. Note that the PD of BZT_20 is derived from figure 4.10.

4.2.3 Polarization switching

The polarization of the sample with 10% Zr can be successfully switched, as illustrated in figure 4.16. The actual switched area is considerably larger (the side length of the poled square is $7\ \mu\text{m}$ according to the profiles in figures 4.16d and 4.16f) than the target area (cf. figure 4.16a and 4.16b). This is most likely caused by the diverging field at the tip, a coalescence with already present domains in the vicinity of the target area, and the high magnitude of the poling voltage ($-50\ \text{V}$). The majority of the induced domains remained stable for at least 18 h, with a few renucleated domains of elongated shape. The RDs presented in figure 4.16e exhibit a clear shift of the peak towards negative values. Note that the peak shift towards more negative values after 18 h is most likely an artefact originating from changing tip-sample contact properties and not from a change in the electromechanical properties of the material. The elongated domain in the lower left part of figure 4.16b formed as the biased tip approached the target area. The well-behaved switch of polarization is another indicator of true ferroelectricity in this sample.

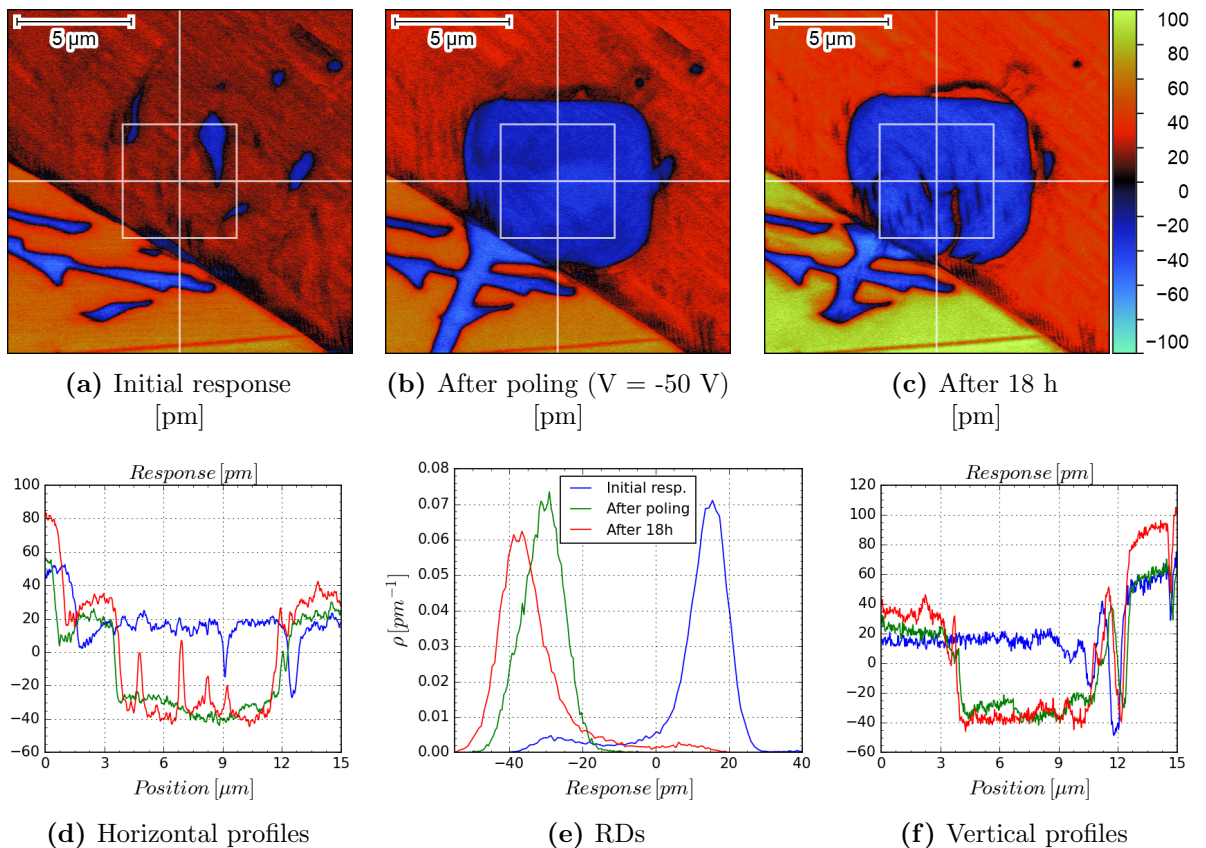


Figure 4.16: BZT (10% Zr) - Polarization switching experiment. The PFM response in (a) displays the pristine domain structure and (b) the response after poling with $-50\ \text{V}$. The third scan (c) covers the same spot, 18 h after poling. Figure (d), (e), and (f) are the horizontal profiles (marked by the white horizontal lines), RDs (data extracted from within the squares), and vertical profiles (marked by the white vertical lines). The poled area was $5\ \mu\text{m} \times 5\ \mu\text{m}$ in size, as indicated by the white square.

A different outcome of the polarization switching experiment can be obtained for the sample with 20% Zr. A total of three polarization switching attempts were conducted for this sample. Figure 4.17 depicts the results of the first experiment, located in the bulk of a large grain. The response of the pristine polarization state (cf. figure 4.17a) is uniform. A poling attempt with +50 V leads

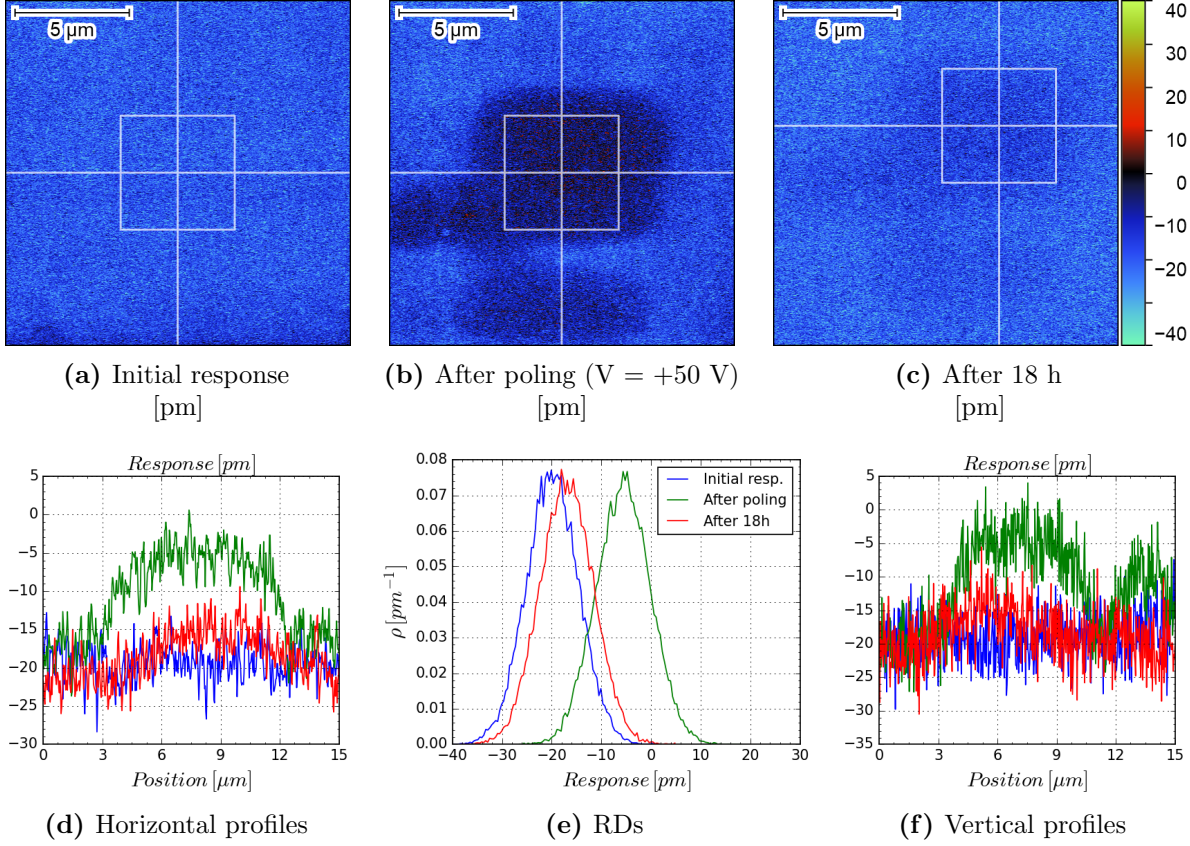


Figure 4.17: BZT (20% Zr) - Polarization switching experiment. The PFM response in (a) displays the pristine domain structure and (b) the response after poling with +50 V. The third scan (c) covers the same spot, 18 h after poling. Figure (d), (e), and (f) are the horizontal profiles (marked by the white horizontal lines), RDs (data extracted from within the squares), and vertical profiles (marked by the white vertical lines). The poled area was 5 μm x 5 μm in size, as indicated by the white square.

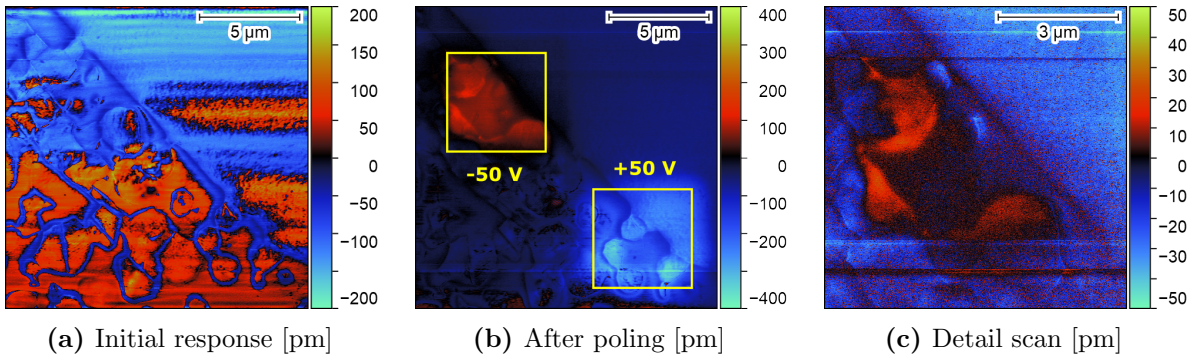


Figure 4.18: BZT (20% Zr) - Polarization switching experiment at the interface between one large and numerous small grains. The PFM scans were conducted near the contact resonance frequency. The pristine domain state is displayed in (a) and (b) represents the same spot after poling with ± 50 V. A more detailed scan of the negatively poled area is displayed in (c).

to a change in the response of the target area towards more positive values (cf. figure 4.17b), which almost completely vanishes after 18 h (cf. figure 4.17c). This is further confirmed by the RDs presented in figure 4.17e. A close look at both cross sections (cf. figure 4.17d and 4.17f) reveals that the interface between the poled and unpoled area is not well-defined, but rather smeared out. These results suggest that the source of the contrast detected after poling is not a change of polarization, but rather emerging from (screening) charges. However, this does not necessarily exclude that the FE polarization was switched, but rather that the PFM response is too weak to be detected [93]. Consequently, a second and third poling experiment with the PFM imaging frequency near the contact resonance were conducted. The two experiments were conducted at the same spot as in figure 4.11. The spot presented in figure 4.18a was poled in two square areas of $5\ \mu\text{m} \times 5\ \mu\text{m}$ with $\pm 50\ \text{V}$ (cf. figure 4.18b). One significant detail about the positively poled area is that the response is shifted towards lower values, in contrast to the results presented in figure 4.17b. Furthermore, the poled area is well-defined and does exhibit a sharper border. This contradicting result consolidates the previously made assumption that non-piezoelectric contributions dominate during SF-PFM image acquisition. Poling with negative bias resulted in a polarization switch in the smaller grains, but not in the larger grain. One explanation could be that the newly formed domain in the large grain immediately reversed to adapt to the polarization state of the large grain. A second, magnified scan of the negatively poled area (cf. figure 4.18c) depicts an already partially relaxed domain structure, suggesting that the system is in a highly dynamical state. The results imply that the polarization of BZT_20 can be temporarily switched, but imaging the induced domains is only possible with resonance PFM in areas with smaller grains. A possible explanation for this selective switching behaviour is the abundance of grain boundaries in areas with smaller grains, which act as pinning centres for domain walls and (temporarily) inhibit relaxation of the domains [30].

The samples with 30% Zr and 40% Zr exhibit similar behaviour upon poling (cf. figure 4.19). According to the RDs in figures 4.19d and 4.19e, both systems have a similar initial response magnitude before poling, contradicting the unequal ADs presented in figure 4.15. The minor change in contrast is most probably caused by accumulated charge carriers on the surface, which is also confirmed by their respective RDs. In the BZT_40 sample, there seems to be stronger contrast in some grains. In both cases, the induced contrast vanishes completely after 40 h and 19 h for the BZT_30 and BZT_40 sample, respectively. The poling experiments further consolidate the assumption that these two systems are in the ER state at RT, with highly dynamical PNRs that cannot be permanently stabilized in their orientation by poling [91].

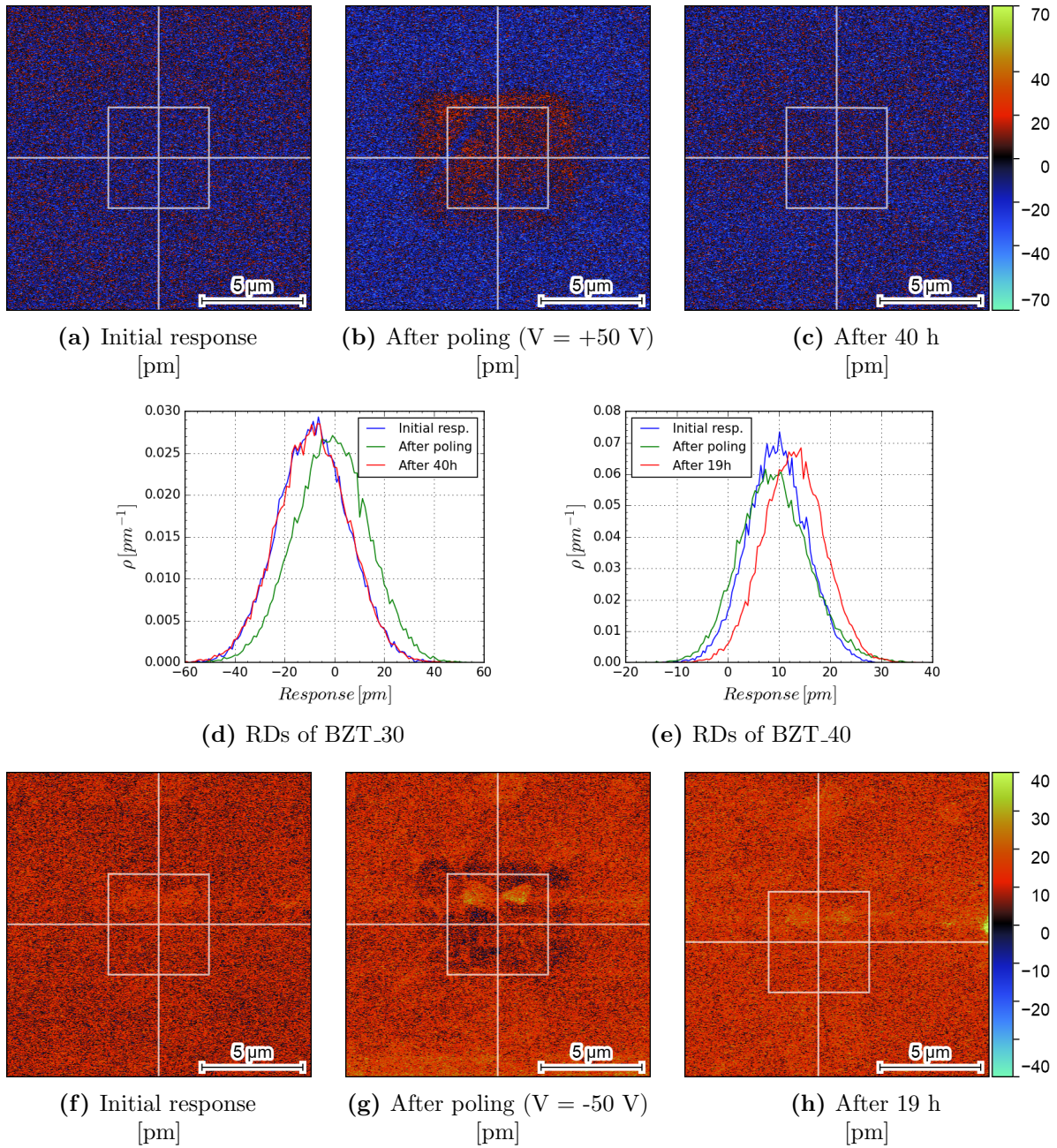


Figure 4.19: BZT (30% and 40% Zr) - Polarization switching experiments. Figures (a - d) belong to BZT_30 and figures (e - h) to BZT_40. The PFM response in (a)/(f) displays the pristine domain structure and (b)/(g) the response after poling with +50 V/-50 V. The third scan (c)/(h) covers the same spot, 40 h/19 h after poling. The RDs are displayed in (d) and (e). The poled area was $5 \mu\text{m} \times 5 \mu\text{m}$ in size, as indicated by the white square.

4.2.4 SS-PFM

The results of the temperature-dependent SS-PFM experiments of BT, BZT_10, BZT_20, and BZT_40 are depicted in figure 4.20. Note that the BT curves serve as a means of comparison and will not be discussed in detail here. The focus of the discussion will be laid again on the Work of Switching parameters as well as on the Acceptance Rate of the filter of AmpOn and AmpOff.

The sample with 10% Zr exhibits a nearly 100% Acceptance Rate for all data points. Both the AmpOn and AmpOff curves exhibit the same trend towards higher temperatures, that is, a rising Work of Switching parameter. The measured temperatures were in the interval between 67.2 °C and 109.9 °C. Various sources report a transition temperature T_m between 68 °C and 94 °C [41, 92, 98] for BZT_10, which is within the measured temperature range. However, unlike in BT, no abrupt change in the Work of Switching parameter is observed. A possible explanation for this discrepancy with the literature results is the DPT of this sample, which translates to a non-abrupt loss of polarization. Another detail of importance is that BZT_10 exhibits a so-called pinched phase transition [96]. According to this, the coexistence of multiple stable crystal symmetries (rhombohedral, tetragonal and cubic) might be possible in the vicinity of T_m (i.e. translating to a higher number of possible discrete polarization orientations), thus explaining the overall higher Work of Switching parameter compared to BT [92]. The presence of stable FE domains above T_m for substituted BT with a DPT was also reported in literature [99].

As already addressed before, BZT_20 should have its DPT in the temperature interval between 11 °C and 37 °C [41, 92, 98]. The declining trend of the Work of Switching parameter of AmpOff (red) indicates that BZT_20 has at least partially completed this transition. It can be assumed, that this sample still exhibits polar clusters above T_m , which become increasingly unstable at higher temperatures. The evolution of the Work of Switching parameter of AmpOn does not exhibit the same trend as in AmpOff, which is most likely attributed to the lower Acceptance Rate at lower temperatures, possibly emerging from instrumental issues. The Saturation Response of BZT_20 is still significantly higher than in BT.

The trend of the sample with 40% Zr is similar to the one in BZT_20. Both Work of Switching parameters are lower than BZT_20, and AmpOff is even lower than BT. Furthermore, the values exhibit a slight decline towards higher temperatures. The low A_{fs} is also an indicator for slim hysteresis loops, corresponding to low hysteric energy losses. One striking detail about BZT_40 is that the Acceptance Rate is high for both AmpOn and AmpOff, even though the system is significantly above $T_m \sim -75$ °C (cf. figure 2.11a). This is another indicator for dynamic PNRs in the ER state, which can be temporarily stabilized in their orientation [41].

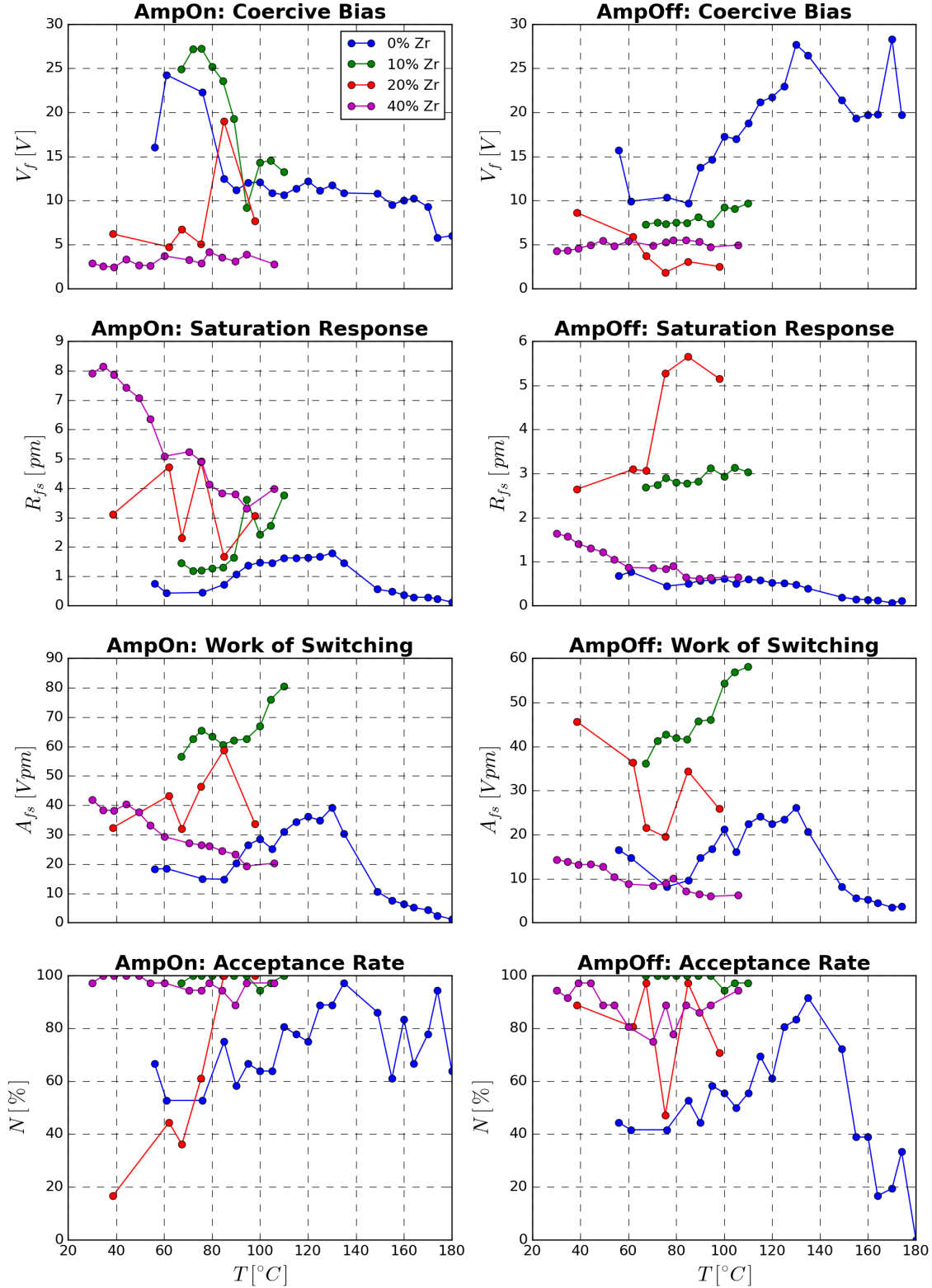


Figure 4.20: BZT - SS-PFM results. The graphs display the temperature-dependent evolution of the Coercive Bias, Saturation Response and Work of Switching parameter from the fitting procedure (cf. equations 3.15, 3.16 and 3.17), as well as the Acceptance Rate from the filters described in section 3.5.2, for AmpOn and AmpOff. The Zr-substituted samples behave significantly different compared to the pure BT. However, even the sample with the highest substitution exhibits PFM hysteresis loops.

4.3 BNT-System

For this system, five different compositions were examined by PFM: 2.5% Nb (BNT_2p5), 5% Nb (BNT_5), 7% Nb (BNT_7), 10% Nb (BNT_10), and 15% Nb (BNT_15). In contrast to BZT, no samples were left out in any of the measurements.

4.3.1 Microstructure

When a sufficient amount of Nb is introduced into BT, it acts as a grain growth inhibitor [100]. The fine-grained microstructure of the BNT samples is displayed in figure 4.21. Most grains have a size between 1 μm and 2 μm , and in 2.5% Nb (cf. figure 4.21a), a lamellar domain structure can be derived from the topography. BNT_10 exhibits slightly larger grains compared to the other samples, which is most likely a result of slightly deviating processing parameters. The microstructure of all samples is dense with few pores comparable in size to the grains. In general, the grain size distribution appears to become more uniform with higher substitution.

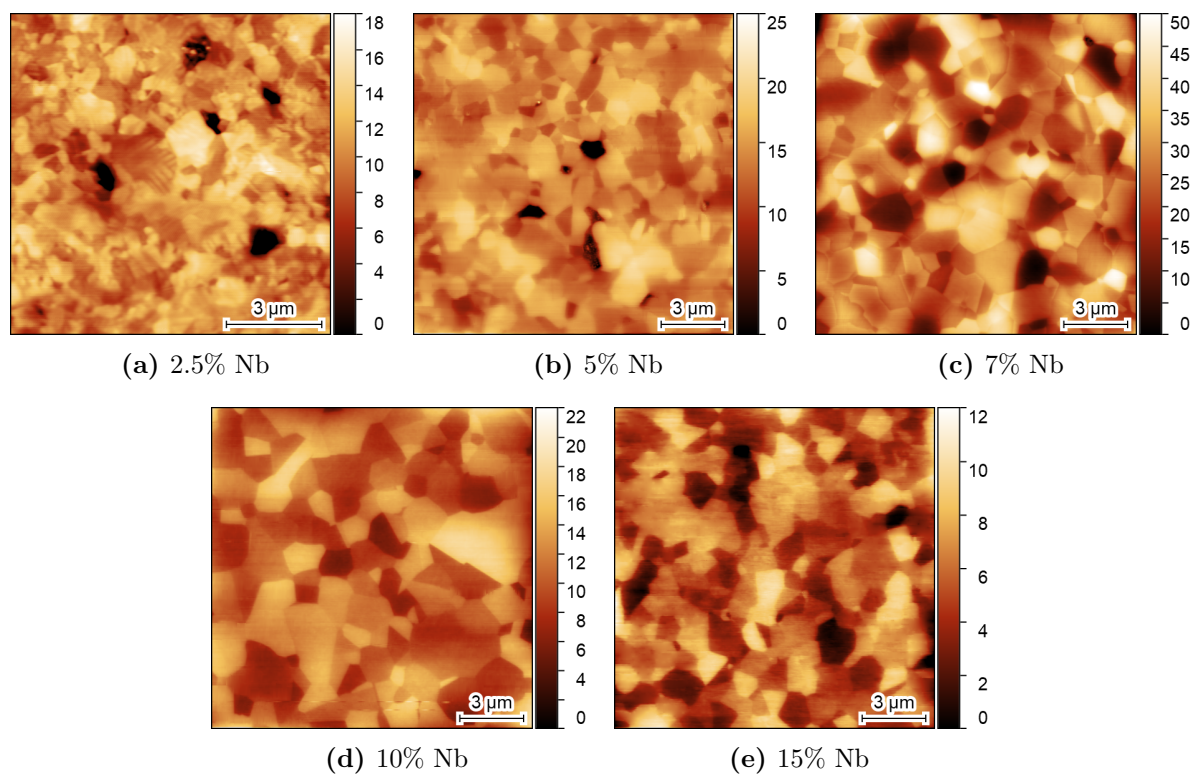


Figure 4.21: BNT - Microstructure. All images were acquired using contact-AFM.

4.3.2 Domain structure

The sample with the lowest substitution (2.5% Nb) exhibits an FE domain structure, as illustrated in figure 4.22. Lamellar features are visible in the topography, amplitude, as well as in the phase image (cf. figures 4.22a, 4.22b, and 4.22c). The orientation of the lamellae appears to be uniform within individual grains, so the domain structure of BNT_2p5 can be classified as lamellar type, which is expected for FEs with grains of this size [30, 31]. The AD and PD are monomodal and bimodal, respectively, with their corresponding peaks at 6 pm, -165° , and -15° . A magnified scan of the same area is depicted in figure 4.23, and a lamellae width of approximately 100 nm can be derived from the profiles of the phase image (cf. figures 4.23b and 4.23c). Summarized, BNT_2p5 clearly exhibits a domain structure emerging from spontaneous polarization. According to figure 2.11b and supporting literature [42, 43], this system exhibits non-centrosymmetric

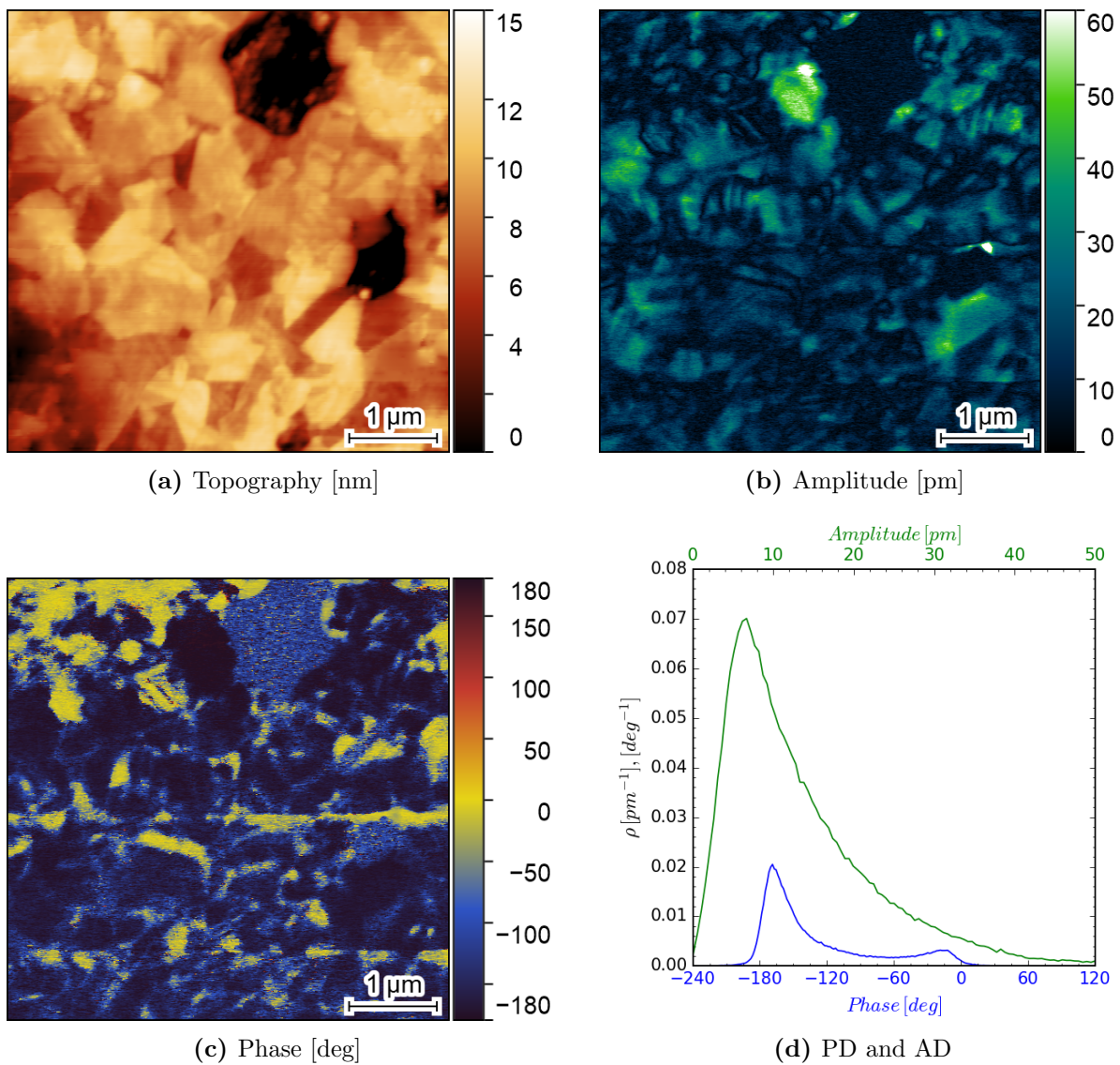


Figure 4.22: BNT(2.5% Nb) - Domain structure. The topography (a), amplitude (b), and phase (c) image reveal a lamellar domain structure. In (d), the monomodal AD and bimodal PD indicate genuine PFM contrast.

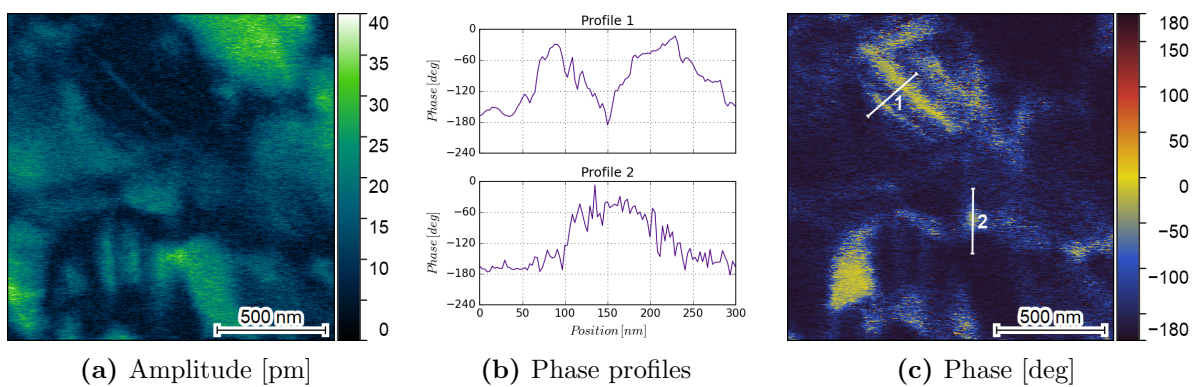


Figure 4.23: BNT(2.5% Nb) - Magnified domain structure. The amplitude (a), phase (c), and the phase profiles (b) along the lines indicated in (c) reveal a lamellae width of 100 nm.

rhombohedral symmetry at RT, further confirming ferroelectricity as the origin of this measured domain structure.

Raising the substitution amount to 5% drastically disrupts the domain structure of BNT, as illustrated in figure 4.24. The phase and amplitude (cf. figures 4.24c and 4.24b) appear to be dominated by noise and no domain structure can be derived from either of them. There is also no correlation between the topography (cf. figure 4.24a) and the PFM signal. In some instances, there is an enhanced amplitude in the vicinity of some grain boundaries or pores, suggesting topographic cross-talk. A closer look at the phase reveals some clusters of enhanced phase contrast. However, it is unclear whether this is weak PFM contrast or some other non-piezoelectric contribution, e.g. weak electrostatic contrast. The AD and PD are both monomodal, with their respective peaks at 4 pm and -195° . There are three possible explanations for why there is no distinct PFM contrast in this sample: One explanation is that the high Nb substitution

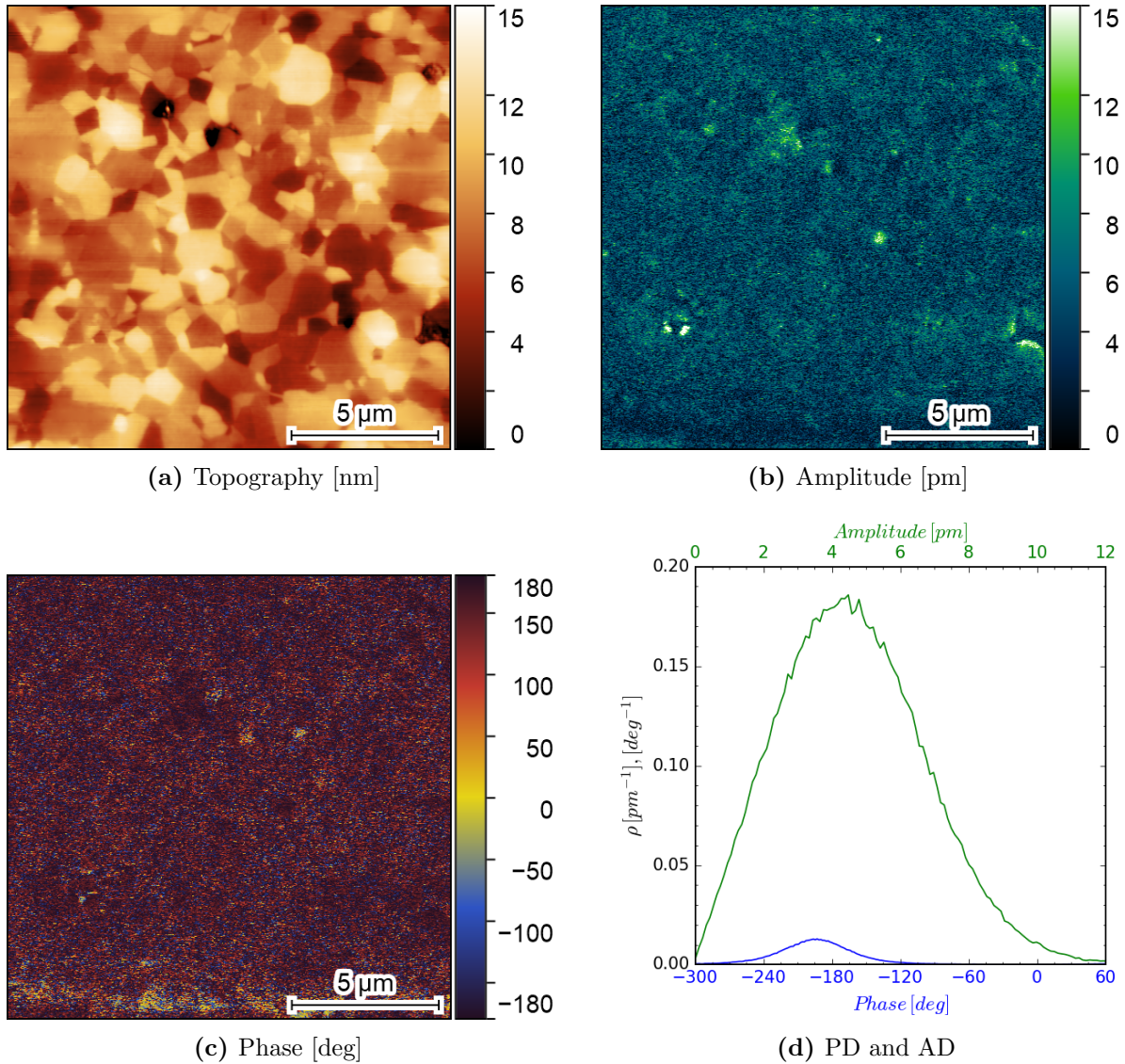


Figure 4.24: BNT(5% Nb) - Domain structure. The amplitude (b) as well as phase (c) image are predominantly comprised of noise. There is an enhanced amplitude contrast in the vicinity of some grain boundaries and pores, possibly emerging from topographic (a) crosstalk. Both the AD and PD (d) are monomodal.

reduces the domain size beyond the lateral resolution limit of PFM [55, 77]. Another explanation could be the fact that the system is most likely in the vicinity of its T_m at RT (cf. figure 2.11b), which results in the increased instability of the nano-sized domains, impeding stable domain imaging [42, 43, 101]. Finally, a strong electrostatic contribution caused by a significant change in the surface potential due to the increasing prevalence of charge-balancing Ba or Ti vacancies cannot be excluded as well [46, 93, 102, 103]. In summary, no domain structure can be obtained for this composition. However, the mechanisms that prevent PFM contrast formation remain unclear.

Further substitution (7% Nb, 10% Nb, and 15% Nb) does not change the domain structure of BNT significantly, as illustrated in figures 4.25, 4.26, and 4.27. The phase and amplitude images are mainly comprised of noise, and no distinct domain structure can be derived from either of them. There seems to be minor contrast in the vicinity of grain boundaries in all amplitude pictures, which could be caused by topographic cross-talk or local symmetry breaking in the grain

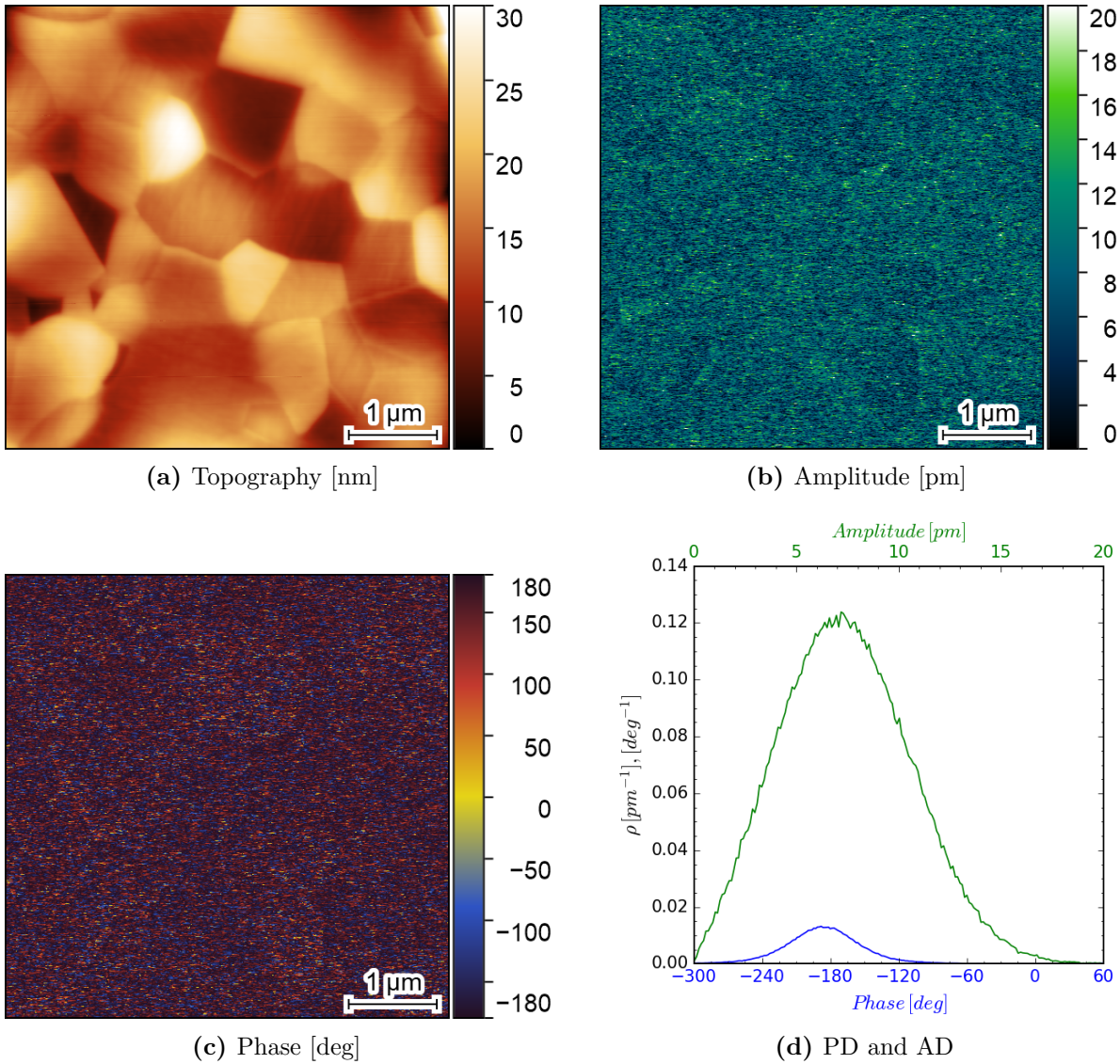


Figure 4.25: BNT(7% Nb) - Domain structure. The amplitude (b) as well as phase (c) image are predominantly comprised of noise. No domain structure can be derived here. Both the AD and PD (d) are monomodal. The topography is displayed in (a).

boundary [97]. The ADs are monomodal with peaks at 7 pm, 3.5 pm, and 7.5 pm for BNT_7, BNT_10, and BNT_15, respectively. Monomodality can be obtained for the PDs as well, with peaks at -187.5° , -195° , and -175° for BNT_7, BNT_10, and BNT_15, respectively. Comparing these results with the phase diagram in figure 2.11b and other experimental techniques like Raman spectroscopy, impedance spectroscopy, and XRD [42, 43, 101], suggests that FE clusters in these systems are nano-sized, ergodic entities.

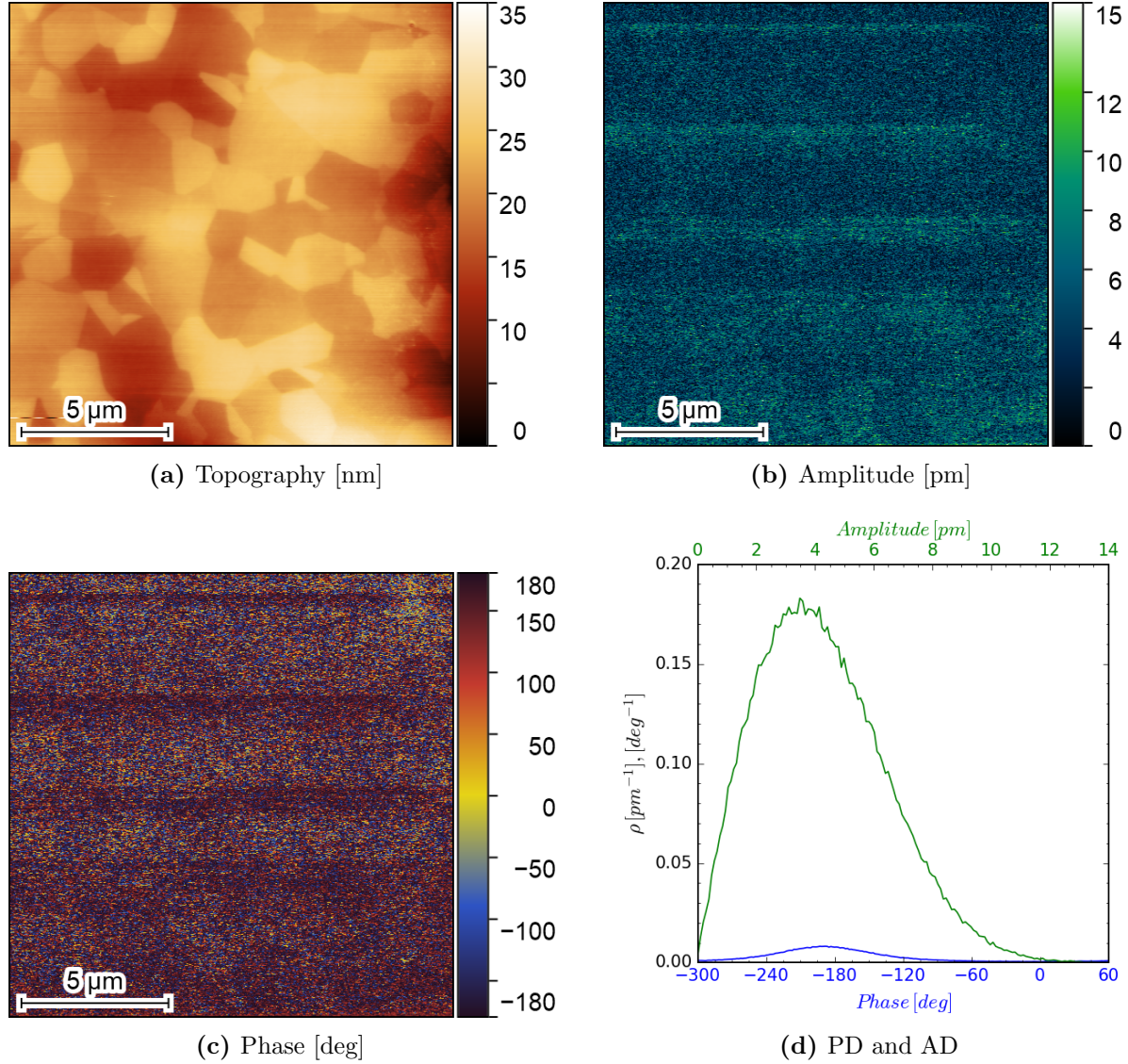


Figure 4.26: BNT(10% Nb) - Domain structure. The amplitude (b) as well as phase (c) image are predominantly comprised of noise. No domain structure can be derived here. Both the AD and PD (d) are monomodal. The topography is displayed in (a).

Figure 4.28 depicts the ADs and PDs of all BNT samples measured with SF-PFM. In general, all samples exhibit a lower amplitude compared to pure BT. However, increasing the substitution amount does not necessarily lead to the reduction of the amplitude, as can be seen by comparing the ADs of BNT_5 and BNT_15. It appears that there is a non-trivial relation between the Nb concentration and measured PFM amplitude, probably determined by the type and concentration of charge-balancing vacancies. All PDs are monomodal except for BT and BNT_2p5, which exhibit a spontaneous polarization that can be detected by PFM.

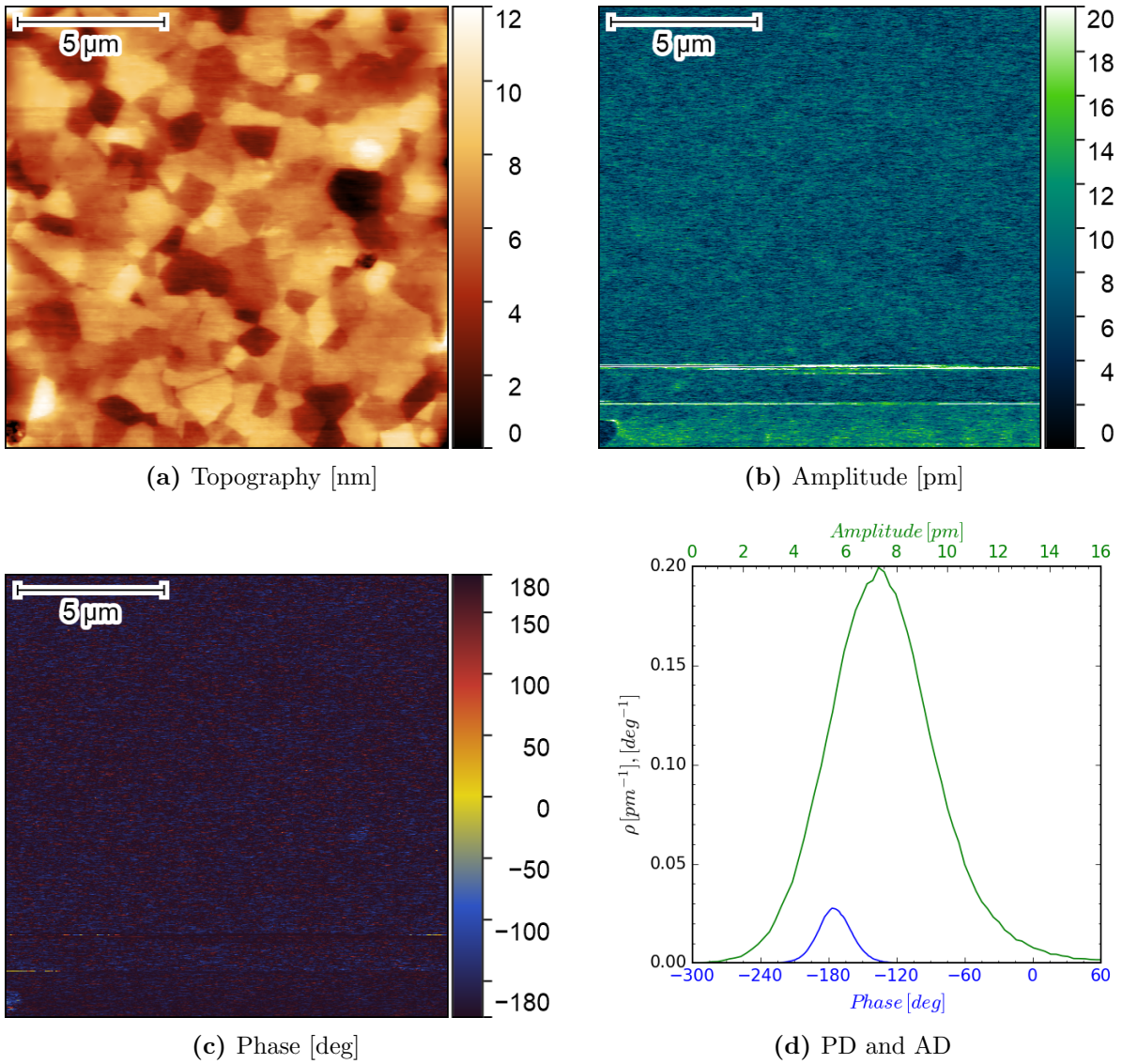


Figure 4.27: BNT(15% Nb) - Domain structure. The amplitude (b) as well as phase (c) image are predominantly comprised of noise. No domain structure can be derived here. Both the AD and PD (d) are monomodal. The topography is displayed in (a).

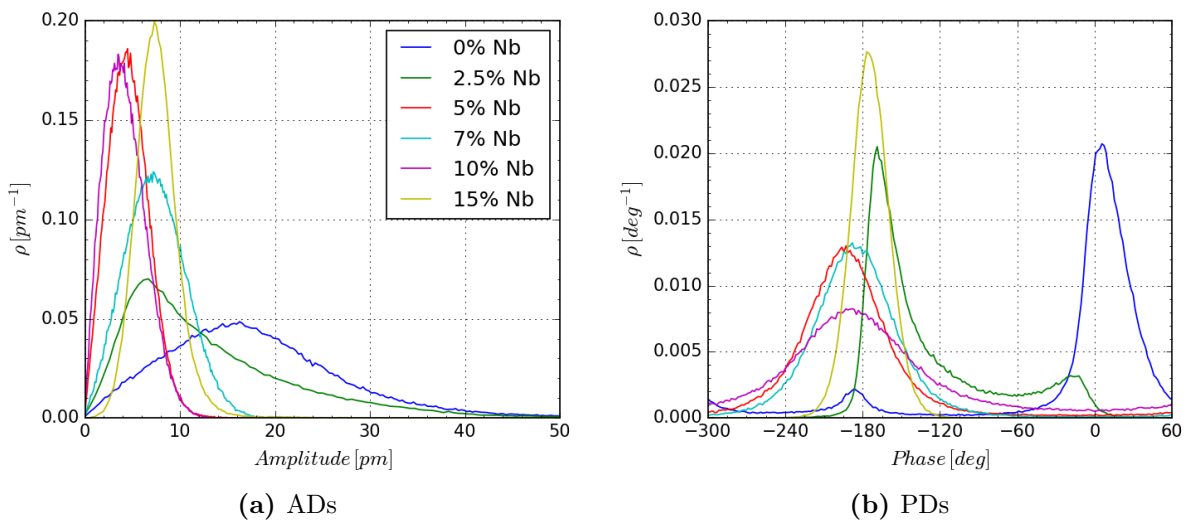


Figure 4.28: BNT - Summary of the SF-PFM results. The ADs are displayed in (a) and the PDs in (b).

4.3.3 Polarization switching

BNT_2p5 was poled with a bias of +50 V, as illustrated in figure 4.29. The pristine domain structure (cf. figure 4.29a) exhibits numerous sub-micrometre-sized domains with antiparallel vertical polarization. Hence, only a fraction of the domains can be reversed by the application of a positive bias (cf. figure 4.29b). Immediately after poling, there is a significant shift towards more positive response values, as depicted in the RDs in figure 4.29e. After 18 h, a significant number of the newly formed domains relaxed (cf. figure 4.29c), which is indicated by a shift of the RD towards more negative values. Another noteworthy detail can be found in the surrounding of the poled area in figures 4.29b and 4.29c. The poling did not only affect the area within the square but changed the surrounding domain state as well, towards more positive values on average. This is followed by a shift towards more negative values in the time interval between the first and second scan after poling, which can be explained as a means to reduce the excess electrostatic energy of the system, compensating for the predominantly downward-pointing vertical polarization within the square. Even though the domains clearly switched in the target area, the change in response, illustrated by the horizontal and vertical profiles in figures 4.29d and 4.29f, is less pronounced compared to similar systems, e.g. BZT_10 (cf. figure 4.16). However, this can be explained by the much finer domain structure of BNT_2p5 and the fact that the profiles average the response on a width of 5 pixels, thus leading to the apparent attenuation of the response in the vicinity of

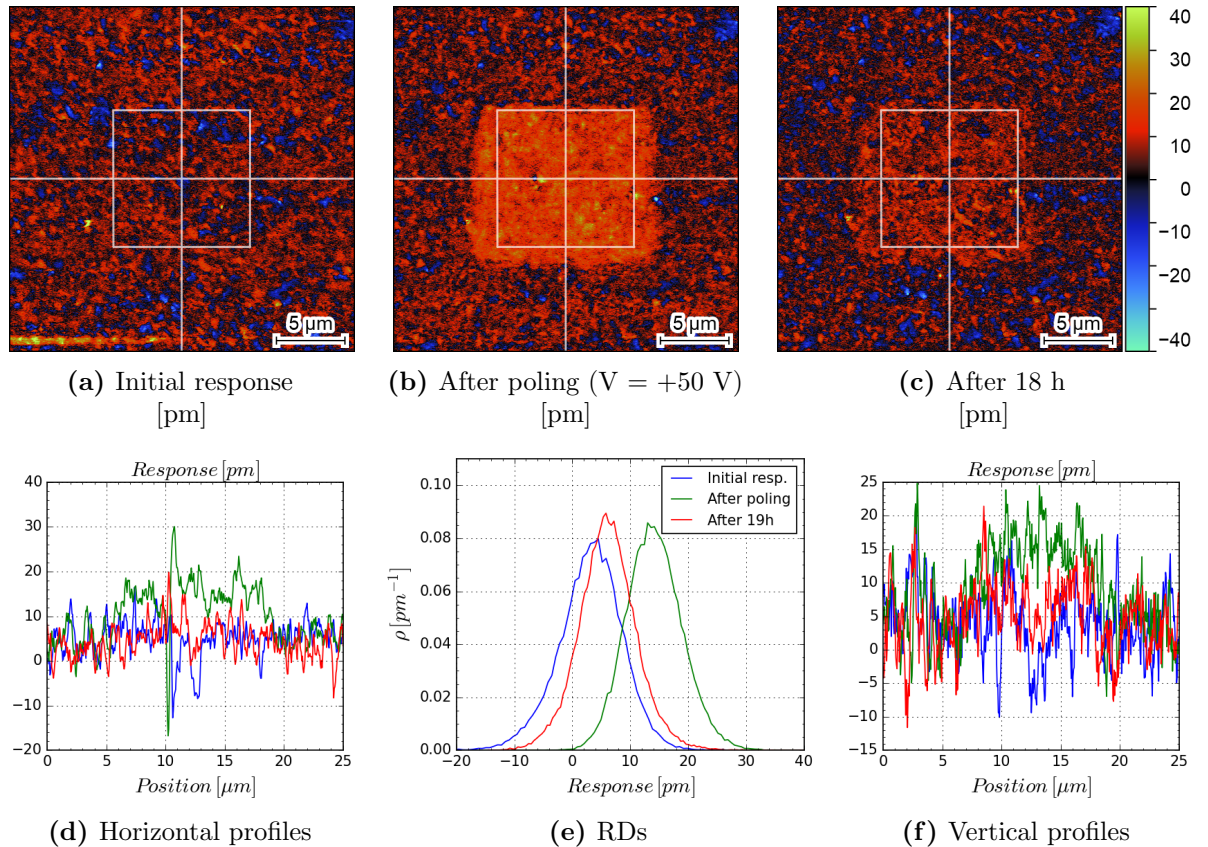


Figure 4.29: BNT(2.5% Nb) - Polarization switching experiment. The PFM response in (a) displays the pristine domain structure and (b) the response after poling with +50 V. The third scan (c) covers the same spot, 18 h after poling. Figure (d), (e), and (f) are the horizontal profiles (marked by the white horizontal lines), RDs (data extracted from within the squares), and vertical profiles (marked by the white vertical lines). The poled area was $10 \mu\text{m} \times 10 \mu\text{m}$ in size, as indicated by the white square.

domains with antiparallel vertical polarization. In summary, domain switching is possible for BNT_2p5 and (partially) stable, which is another indicator of true FE behaviour.

A drastic change in poling behaviour is observed upon higher substitution, as illustrated by the polarization switching results of BNT_5 in figure 4.30. The pristine, almost contrast-less domain structure (cf. figure 4.30a) exhibits a significant change towards negative values in response after applying a DC bias of -50 V. The highest change in response is located at the lower and right rims of the target area, up to 20 pm in magnitude (cf. the horizontal and vertical profiles in figures 4.30d and 4.30f). However, the effects of poling almost completely vanished after 114 h, with a minor remanent change in response towards lower positive values (cf. figure 4.30e). There is no straightforward explanation for why this change of response is so heavily enhanced at the lower and right rims of the target area. However, it appears that the contrast formed in these areas is a result of charge carrier accumulation and that the tip remained in these areas for a longer time, i.e. resulting in the spreading of more charges in these areas.

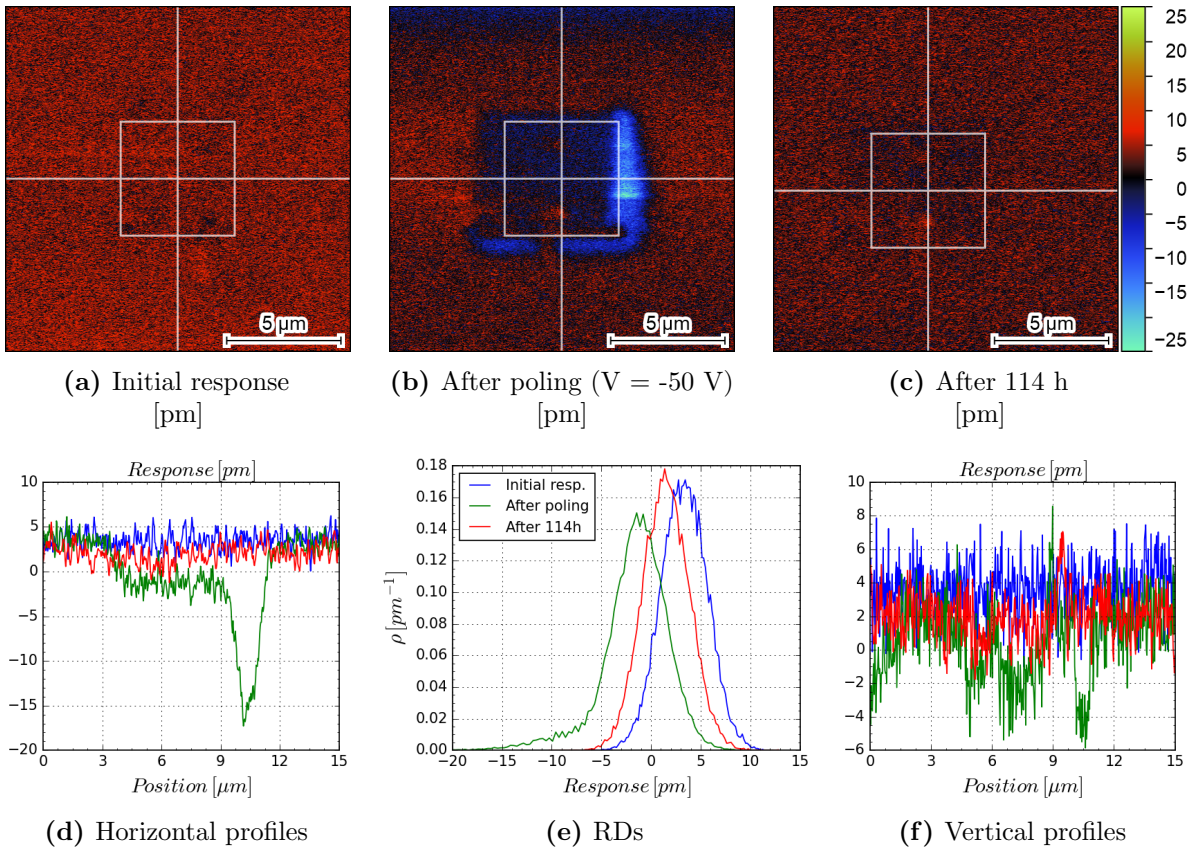


Figure 4.30: BNT(5% Nb) - Polarization switching experiment. The PFM response in (a) displays the pristine domain structure and (b) the response after poling with -50 V. The third scan (c) covers the same spot, 114 h after poling. Figure (d), (e), and (f) are the horizontal profiles (marked by the white horizontal lines), RDs (data extracted from within the squares), and vertical profiles (marked by the white vertical lines). The poled area was $5 \mu\text{m} \times 5 \mu\text{m}$ in size, as indicated by the white square.

BNT_7 exhibits inversed behaviour upon poling with a negative DC bias (cf. figure 4.31). The pristine and uniform domain structure (cf. figure 4.31a) is, in contrast to BNT_5, entirely comprised of negative, noise-like response and poling leads to a shift towards more positive values of response (cf. figure 4.31b). This shift is also visible in the horizontal and vertical profiles (cf.

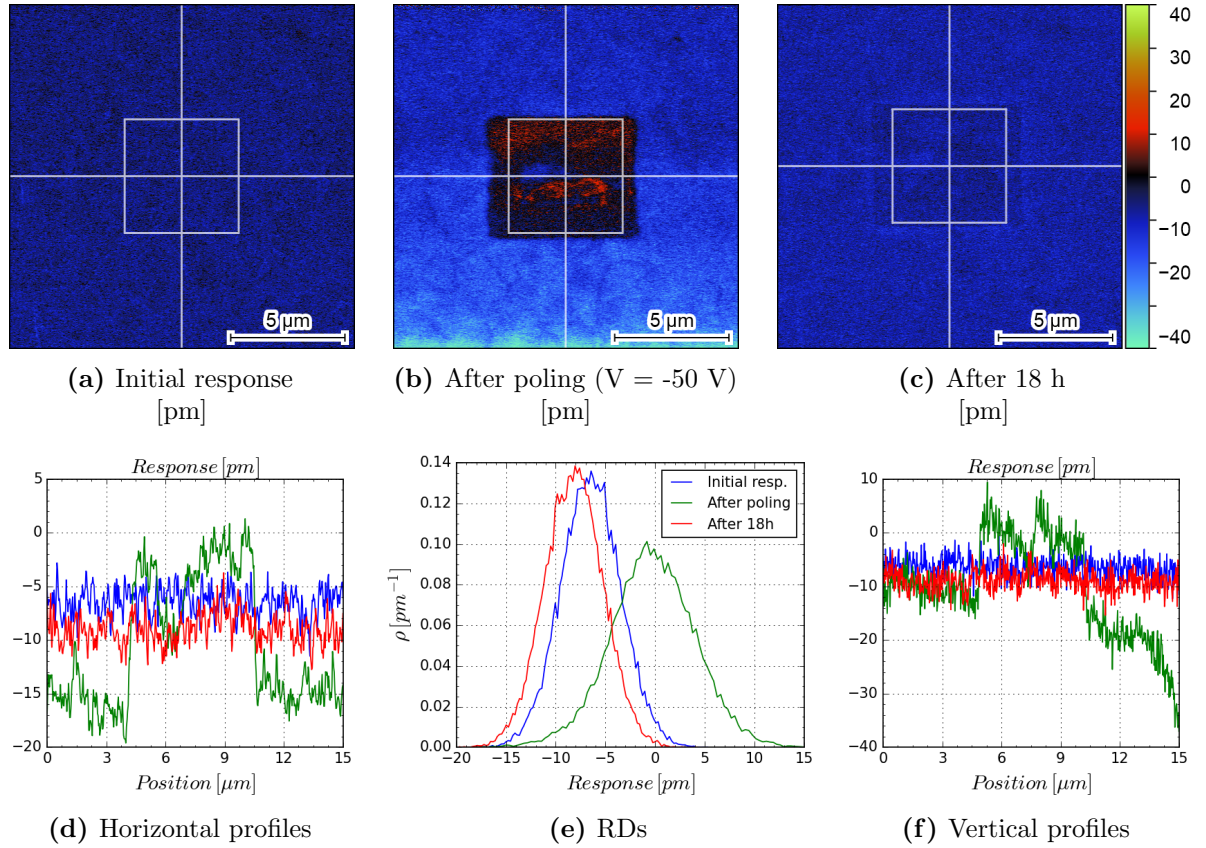


Figure 4.31: BNT(7% Nb) - Polarization switching experiment. The PFM response in (a) displays the pristine domain structure and (b) the response after poling with -50 V. The third scan (c) covers the same spot, 18 h after poling. Figure (d), (e), and (f) are the horizontal profiles (marked by the white horizontal lines), RDs (data extracted from within the squares), and vertical profiles (marked by the white vertical lines). The poled area was $5 \mu\text{m} \times 5 \mu\text{m}$ in size, as indicated by the white square.

figure 4.31d and 4.31f) as well as in the RDs in figure 4.31e. The poled area is slightly extended in the scan direction, which is a result of the additional distance travelled for changing from the trace to the retrace direction and vice versa. After 18 h, the induced change completely vanished (cf. figure 4.31c). One detail of importance is the enhanced, slowly decaying contrast at the bottom of the scan immediately after poling. This peculiar behaviour can be attributed to the accumulation of charges with opposite polarity on the probe and surface which decay or recombine during the scan.

The sample with 10% Nb differs significantly from the previous two samples, as illustrated in figure 4.32. While the pristine domain structure, a uniform and noise-dominated image with overall negative response values (cf. figure 4.32a), is equal to that of BNT₇, the reaction to the stimulating DC bias differs significantly. The application of +50 V to the tip results in a shift of response towards more positive values (cf. the profiles in figures 4.32d and 4.32f as well as the RD in figure 4.32e), which contradicts the previous results with the same shift caused by a negative DC bias. Initially, the change in response is concentrated in the lower part of the target area (cf. figure 4.32b), but appears to have spread out in the following 17 h, as illustrated by the last scan in figure 4.32c. So in contrast to BNT₅ and BNT₇, the change in contrast remains, but is still subject to change over time.

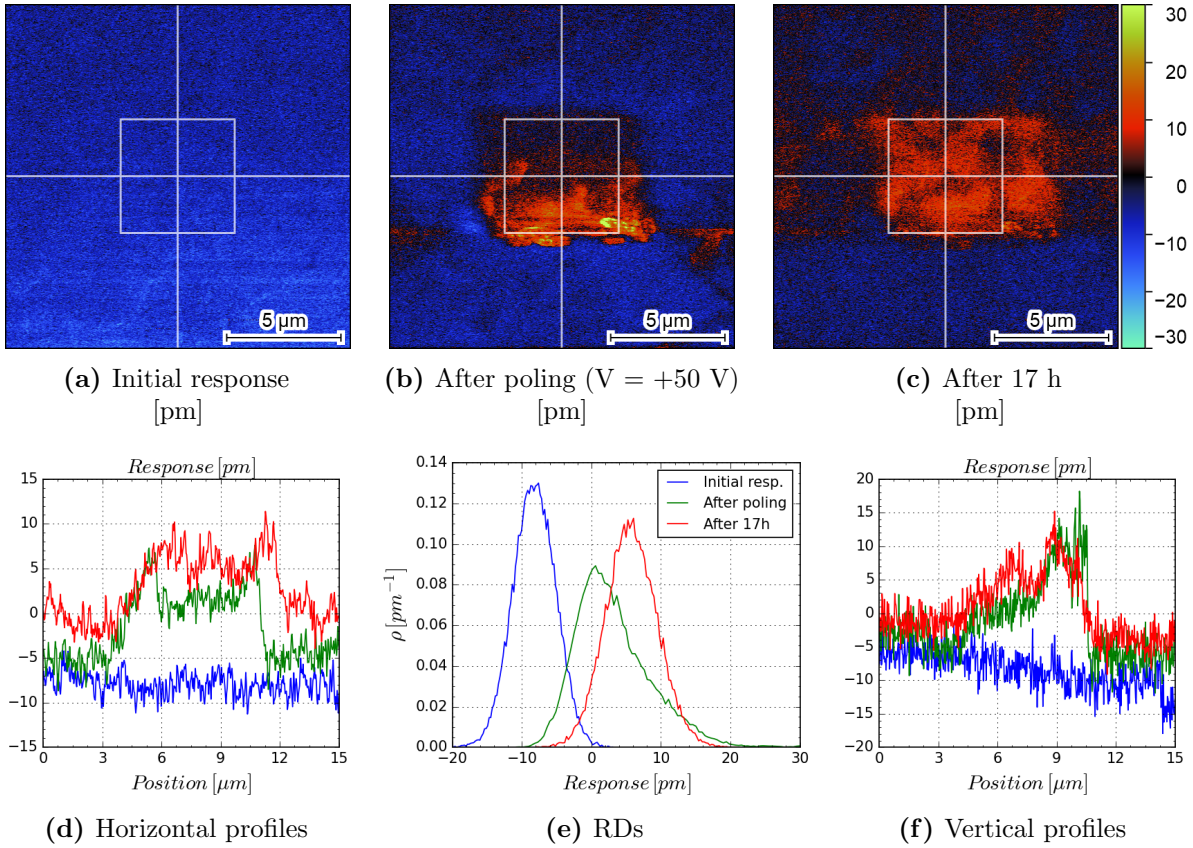


Figure 4.32: BNT(10% Nb) - Polarization switching experiment. The PFM response in (a) displays the pristine domain structure and (b) the response after poling with +50 V. The third scan (c) covers the same spot, 17 h after poling. Figure (d), (e), and (f) are the horizontal profiles (marked by the white horizontal lines), RDs (data extracted from within the squares), and vertical profiles (marked by the white vertical lines). The poled area was $5 \mu\text{m} \times 5 \mu\text{m}$ in size, as indicated by the white square.

Even though BNT₅, BNT₇, and BNT₁₀ differ in their poling behaviour, the observed poling phenomena have a common origin. There is no indicator that the changes in response are predominantly caused by FE polarization switching, but can be rather attributed to the incorporation or accumulation of charge carriers on the surface. Previous studies on donor substitution in BT suggest that either Ba or Ti vacancies are present in the system as a means of charge balancing of Nb donor incorporation [46, 102, 104, 105]. The dominant type of vacancy is determined by the

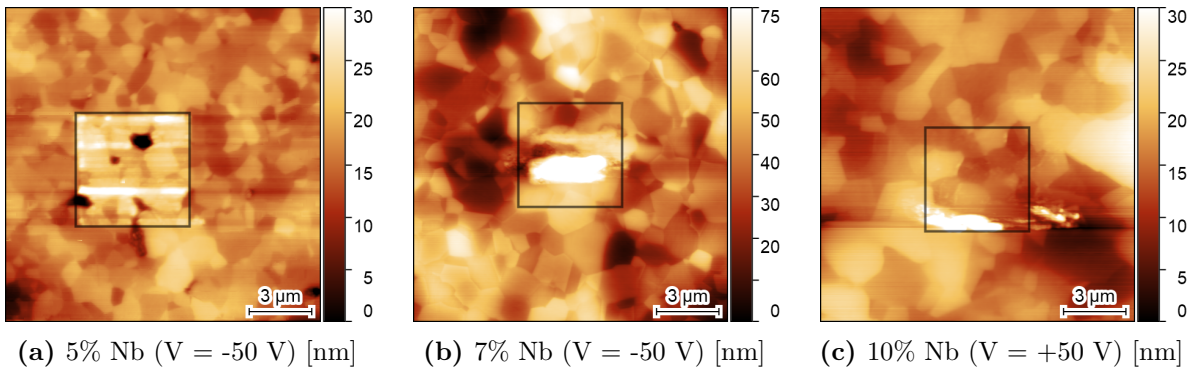


Figure 4.33: BNT - Surface swelling from poling. This effect is only present in BNT₅ (a), BNT₇ (b), and BNT₁₀ (c). The black squares indicate the poled areas.

dopant concentration and the processing parameters of the material. The influence of vacancies on PFM poling experiments in perovskite FEs was studied by Kalinin et al., and an irreversible change in topography, caused by material swelling due to the accumulation of vacancies in the poled area, was reported as well. The three samples exhibit similar behaviour as reported in this work (cf. figure 4.33), indicating electrochemically dominated poling behaviour.

The sample with the highest substitution, namely 15% of Nb, exhibits only little remanent changes from poling with a positive DC bias (cf. figure 4.34). The pristine, noise-dominated domain structure (cf. figure 4.34a) exhibits major charging effects at the bottom of the scan after poling with +50 V (cf. figure 4.34b), which gradually decayed during the scan (cf. the vertical profile in figure 4.34f). The target area does not exhibit any major change in response, except for some small clusters with an apparent positive response. After 16 h, some of these clusters still remain stable, as illustrated in figure 4.34c. However, an overall shift of the response towards positive values was not realized by poling (cf. figure 4.34e). In contrast to BNT_5, BNT_7, and BNT_10, no change in topography was caused by poling, suggesting a negligible change in vacancy concentration upon poling. One explanation for this change of poling behaviour could be an increase of repulsive forces caused by the intrinsically high vacancy concentration in this system, hindering the accumulation of any new charge carriers with the same sign of charge. In

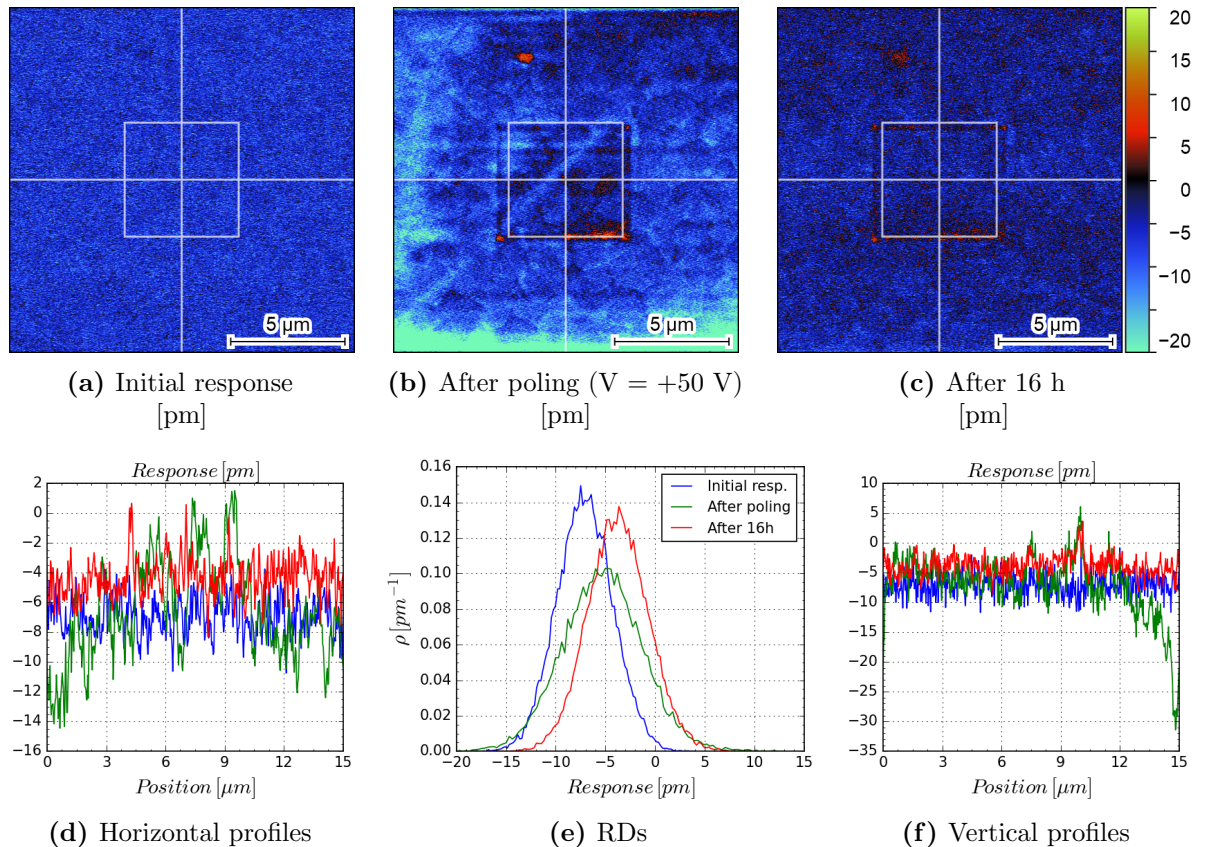


Figure 4.34: BNT(15% Nb) - Polarization switching experiment. The PFM response in (a) displays the pristine domain structure and (b) the response after poling with +50 V. The third scan (c) covers the same spot, 16 h after poling. Figure (d), (e), and (f) are the horizontal profiles (marked by the white horizontal lines), RDs (data extracted from within the squares), and vertical profiles (marked by the white vertical lines). The poled area was 5 μm x 5 μm in size, as indicated by the white square.

summary, BNT₁₅ does not show any signs of stable FE polarization switching due to the strong perturbation from the random electric fields in the system.

4.3.4 SS-PFM

As already observed in the previous section, a non-negligible electrochemical contribution to the PFM signal must be considered with increasing Nb donor substitution, due to the prevalence of charge-balancing Ba or Ti vacancies [46, 102, 104, 105]. Consequently, the generated signal in SS-PFM will be increasingly comprised of non-piezoelectric contributions, so it is appropriate to consider simultaneous contrast formation emerging from SS-PFM and ESM, since both mechanisms can produce genuine phase hysteresis loops and amplitude butterfly curves [72]. As previously, the focus will be laid on the Work of Switching parameter and Acceptance Rate (cf. figure 4.35).

Even though only one DPT in FE BNT compositions was reported in earlier studies [42], a newer contribution by Mayer et al., based on Molecular Dynamics simulations and Raman measurements, suggests the occurrence of three (minorly diffusive) PTs for lower substituted systems [106]. The SS-PFM results of BNT_{2p5} comply with these recent findings. The Work of Switching parameters, in both the AmpOn and AmpOff case, exhibit the same trend upon heating. First, A_{fs} falls drastically (more than 50% of its initial value), followed by an inflection point at 65 °C. Then A_{fs} rises again until it peaks at 90 °C with a steady decline upon further heating. The trend of these two curves can be explained in the following way: According to the phase diagram derived from Raman measurements by Meyer et al., a PT from orthorhombic to tetragonal crystal symmetry takes place somewhere in the temperature interval between 10 °C and 60 °C. It can be assumed that the system has already undergone this transition at the starting temperature, hence the initial decline of A_{fs} . Another PT from tetragonal to (pseudo)-cubic crystal symmetry is expected at approximately 100 °C, which explains the rising Work of Switching parameters above 65 °C. Conveniently, the peak at 90 °C, even though it underestimates T_C , coincides well with this prediction. Overall, BNT_{2p5} behaves like a classical FE similar to BT, with the difference that the Acceptance Rate of AmpOff is not significantly declining after the FE-PE PT as well as overall higher Work of Switching parameter values. A possible explanation for the former feature could be the minor diffusiveness of the PT at a substitution level of 2.5% [42, 43]. Hence a non-spontaneous loss of polarization can be assumed.

For 5% of Nb substitution, the Work of Switching parameters of AmpOn and AmpOff exhibit some differences. While the overall rising A_{fs} of AmpOn exhibits two peaks at 75 °C and 100 °C in the measured temperature interval, only one broad peak at 120 °C followed by a steady decline of A_{fs} can be observed in AmpOff. It is no coincidence that the first sample, which exhibited major charging effects in the poling experiments (cf. figure 4.30), exhibits some peculiarities in the SS-PFM experiments as well. Both types of experiments share the feature that they make use of a high bias at the tip, which can cause vacancy ordering in the system. Earlier work suggests the presence of only one DPT at RT for this composition (cf. figure 2.11b) [42], while the work of Mayer et al. proposes two PTs in the measured temperature interval (orthorhombic–tetragonal and tetragonal–(pseudo)-cubic), lying between RT and 110 °C [106]. Considering a still dominant FE contribution, the latter case is more likely, because if the system has already undergone these two transitions, A_{fs} would rather fall and not rise. However, it is not fully clear if the two peaks

in AmpOn can be attributed to the PTs, or if the broad maximum in AmpOff is an indicator of a DPT and the lower temperature PT (orthorhombic–tetragonal) was already completed at the starting temperature. AmpOff appears to be more convincing since it exhibits the onset of a declining A_{fs} after the peak at 120°C, in contrast to AmpOn, where it still rises after the two peaks. To fully clarify this discrepancy, a deeper investigation of the competing dynamics of SS-PFM and ESM in this system would be necessary. Note that the Acceptance Rate of both AmpOn and AmpOff is stable at high values for all temperatures, indicating the absence of any disturbing factors during the measurements or sudden loss of polarization.

Both sources agree that at a substitution level of 7%, only one broad DPT should occur in BNT, even though the predicted temperatures differ slightly [42, 106]. While Farhi et al. (cf. figure 2.11b) reported T_m at -10° C, Mayer et al. reported T_m in the interval between -10 °C to 40 °C [42, 106]. The SS-PFM results rather support the values of Mayer et al., since there is a steady rise of A_{fs} at the beginning of the measurement with a flat peak at 90 °C, followed by a steeper decline. The low value at 50 °C can be explained by a temporary change in the contact properties between tip and sample, further confirmed by a sudden decrease in the Acceptance Rate at the same temperature. An explanation for the considerably higher A_{fs} values in BNT_7 compared to BNT_5 could be the higher number of vacancies, enabling a larger contribution from ESM contrast in addition to the SS-PFM contrast. Nevertheless, the trend indicates the onset of a DPT in this system due to the broad peak of the Work of Switching parameter, even though additional ESM influences cannot be ruled out. A possible explanation for the late onset could be an inaccurate measurement of the temperature, e.g. due to an improperly placed thermocouple.

According to literature [42, 43, 73], the T_m of BNT with 10% Nb is at approximately -70 °C, so it can be assumed that a possible DPT is already completed in the temperature range of the SS-PFM measurements. Furthermore, due to the higher substitution, i.e. higher vacancy concentration, an increasing contribution emerging from ESM must also be considered. The Work of Switching parameter of AmpOff exhibits a steady decline towards higher temperatures, confirming an already completed DPT. The Work of Switching parameter of AmpOn exhibits several peaks. However, their true origin is unclear. One possible explanation could be an unstable contact between tip and sample during the AmpOn signal acquisition or electrochemical phenomena. In particular, the notably high Saturation Response in AmpOn could be an indicator of major ESM contrast. Further complimentary measurements would be necessary to clarify the true nature of these ambiguities.

Upon 15% substitution, BNT exhibits a low and slowly declining A_{fs} towards higher temperatures, for both AmpOn and AmpOff. Even though BNT_15 has the highest concentration of charge-balancing vacancies, it exhibits the lowest Work of Switching parameter. This indicates a considerably lower ESM contribution, probably caused by repulsive forces emerging from the high vacancy concentration, preventing any accumulation of new vacancies. Furthermore, the slim hysteresis loops (implied by the low A_{fs}) indicate low hysteric energy losses in this composition. The Work of Switching parameter of BNT_15 is in an almost stagnant state due to the low reported T_m at -150 °C [42, 43, 73]. However, even though this system can be considered fully disordered, PFM hysteresis loops can still be measured locally, indicated by the overall high Acceptance Rate of AmpOn and AmpOff, thus confirming the presence of PNRs.

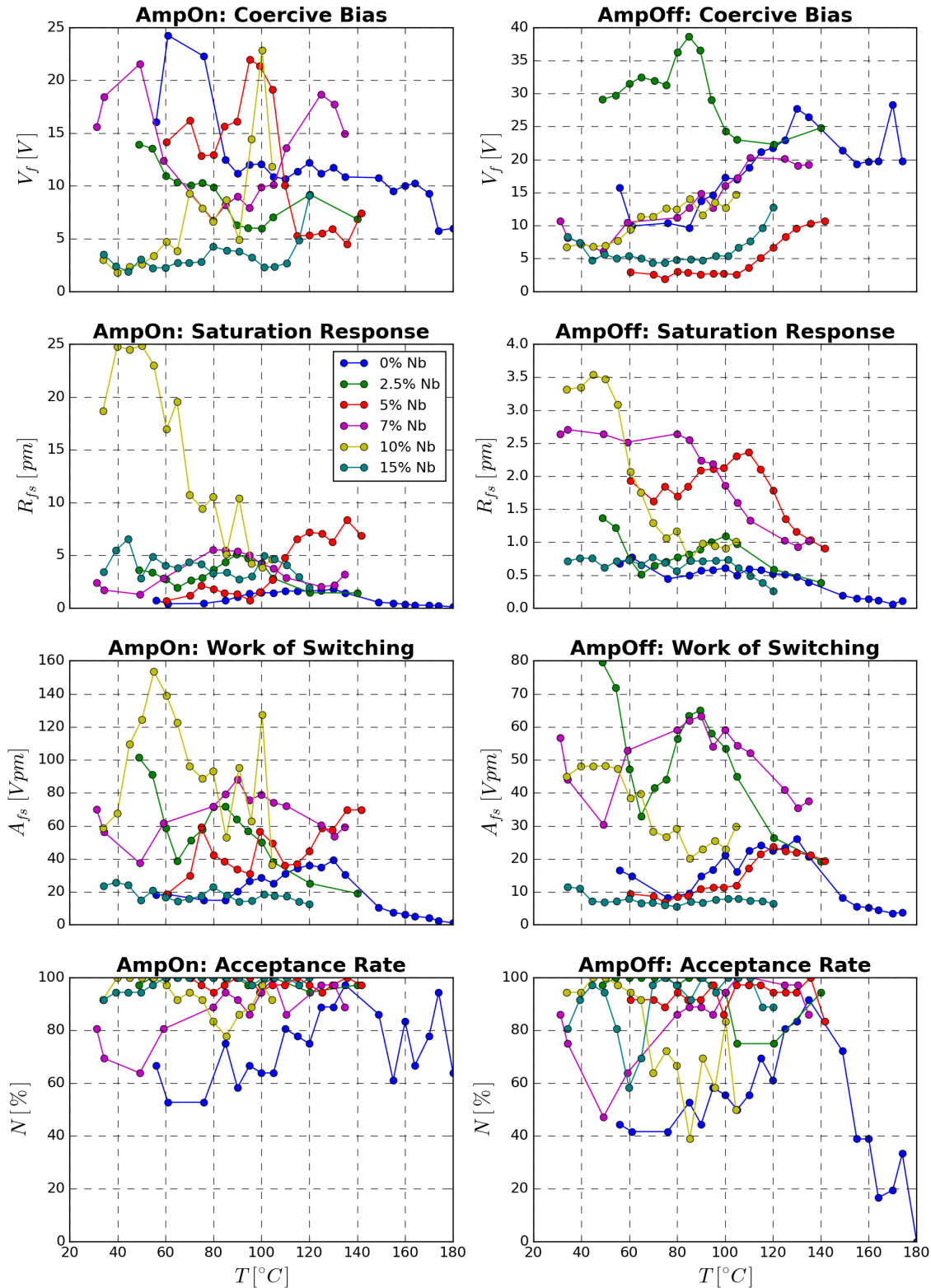


Figure 4.35: BNT - SS-PFM results. The graphs display the temperature-dependent evolution of the Coercive Bias, Saturation Response and Work of Switching parameter from the fitting procedure (cf. equations 3.15, 3.16 and 3.17), as well as the Acceptance Rate from the filters described in section 3.5.2, for AmpOn and AmpOff. The increased concentration of charge-balancing vacancies leads to additional ESM contrast besides PFM contrast.

4.4 BNZT-System

The four BNZT samples have a fixed Nb substitution of 2.5% and a variable Zr amount: 10% Zr (BNZT_2p5_10), 20% Zr (BNZT_2p5_20), 30% Zr (BNZT_2p5_30), and 40% Zr (BNZT_2p5_40). The SS-PFM experiments were not conducted on BNZT_2p5_40 since it was not possible to acquire any PFM hysteresis loops on this sample due to the high degree of FE disorder.

4.4.1 Microstructure

As in BNT, Nb acts as a grain growth inhibitor during sintering [100], thus all BNZT samples exhibit a uniform microstructure with grains ranging between 2 μm and 4 μm in size, as illustrated in figure 4.36. The two lower substituted systems exhibit twinning (cf. figures 4.36a and 4.36b), whereas the two higher substituted systems are practically free of any twins (cf. figures 4.36c and 4.36d). The microstructure exhibits a high overall density with only a few, small pores.

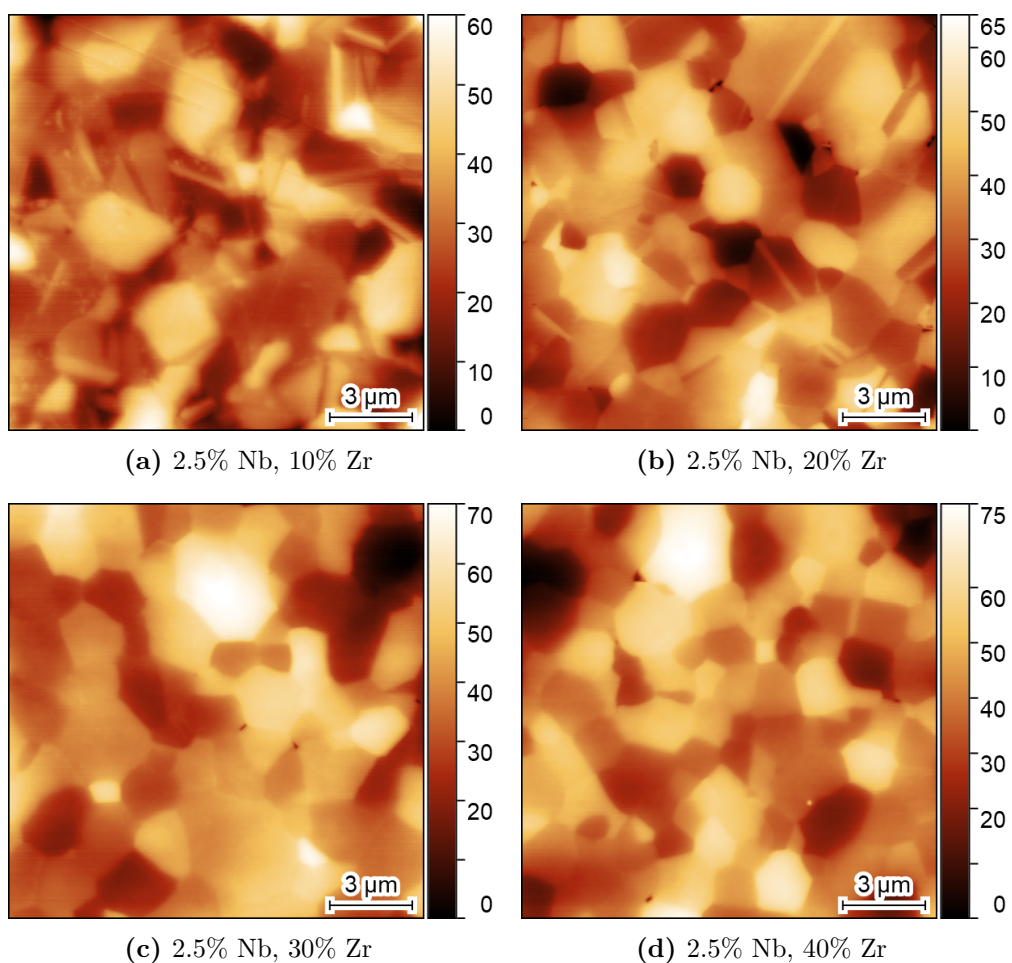


Figure 4.36: BNZT - Microstructure. All images were acquired using contact-AFM.

4.4.2 Domain structure

Even low co-substitution of 2.5% Nb and 10% Zr has already a significant effect on the domain structure, as illustrated in figure 4.37. Both the amplitude and phase image exhibit contrast that seems to coincide with some features in the topography image (cf. figures 4.37b, 4.37c, and 4.37a). The amplitude is enhanced in the lower part of the image, but this contrast weakens during the scan. Such artefacts are usually obtained after poling with a high DC bias. Since that was not the case in this scan, it must have another origin, e.g. a change of FE screening charges concentration on the surface leading to a change in electromechanical/electrostatic contrast [107]. Domain-like clusters can be derived from the phase image, but appear to be smeared out along the scan direction. The AD and PD (cf. figure 4.37d) are monomodal and bimodal, even though it must be mentioned that the peaks in the PD are broader compared to the other samples investigated. Their respective peaks are at 8 pm, -174° and, -30° . A magnified scan of the upper right region (cf. figure 4.38) indicates that the obtained domain structure is subject to constant

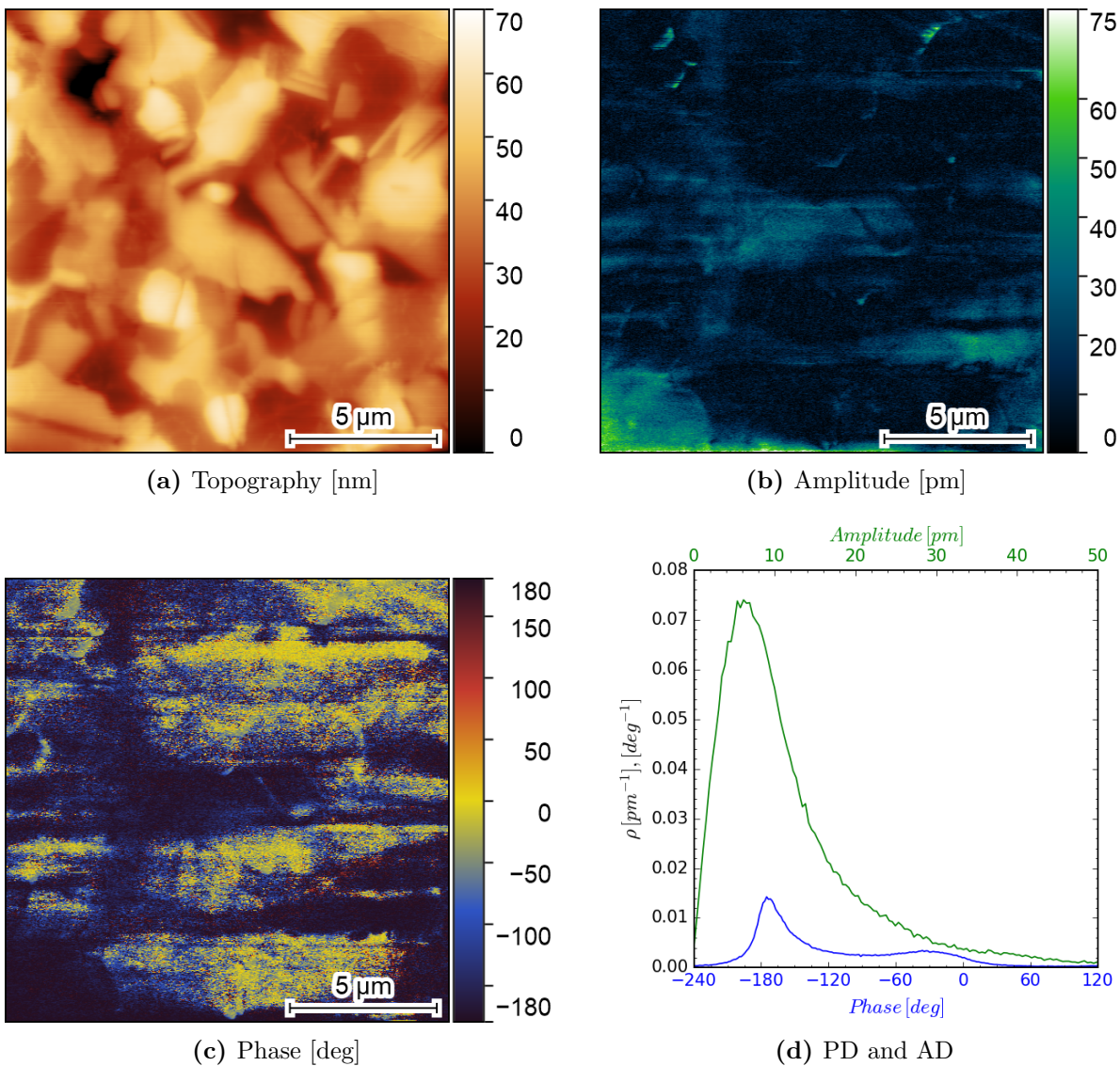


Figure 4.37: BNZT(2.5% Nb, 10% Zr) - Domain structure. Locally enhanced contrast can be obtained in the amplitude (b) and phase (c) image. The AD and PD (d) are monomodal and bimodal, respectively. The topography is displayed in (a).

change. By comparing the response images of two consecutive scans (scan time: 30 minutes) in figures 4.38c and 4.38d and their respective profiles in figure 4.38b, it can be derived that the scanned area develops a more uniform domain structure over time. However, whether this change is intrinsic or mediated by the PFM scan is unclear. Summarized, a domain structure cannot be unambiguously defined from these scans. However, by comparing this system with single-substituted systems of similar substitution level (BZT₂₀ and BNT₅) [42, 91, 92] as well as a paper on co-substituted BNZT [47], it cannot be excluded that this sample still exhibits a semi-stable domain structure as a consequence of spontaneous polarization.

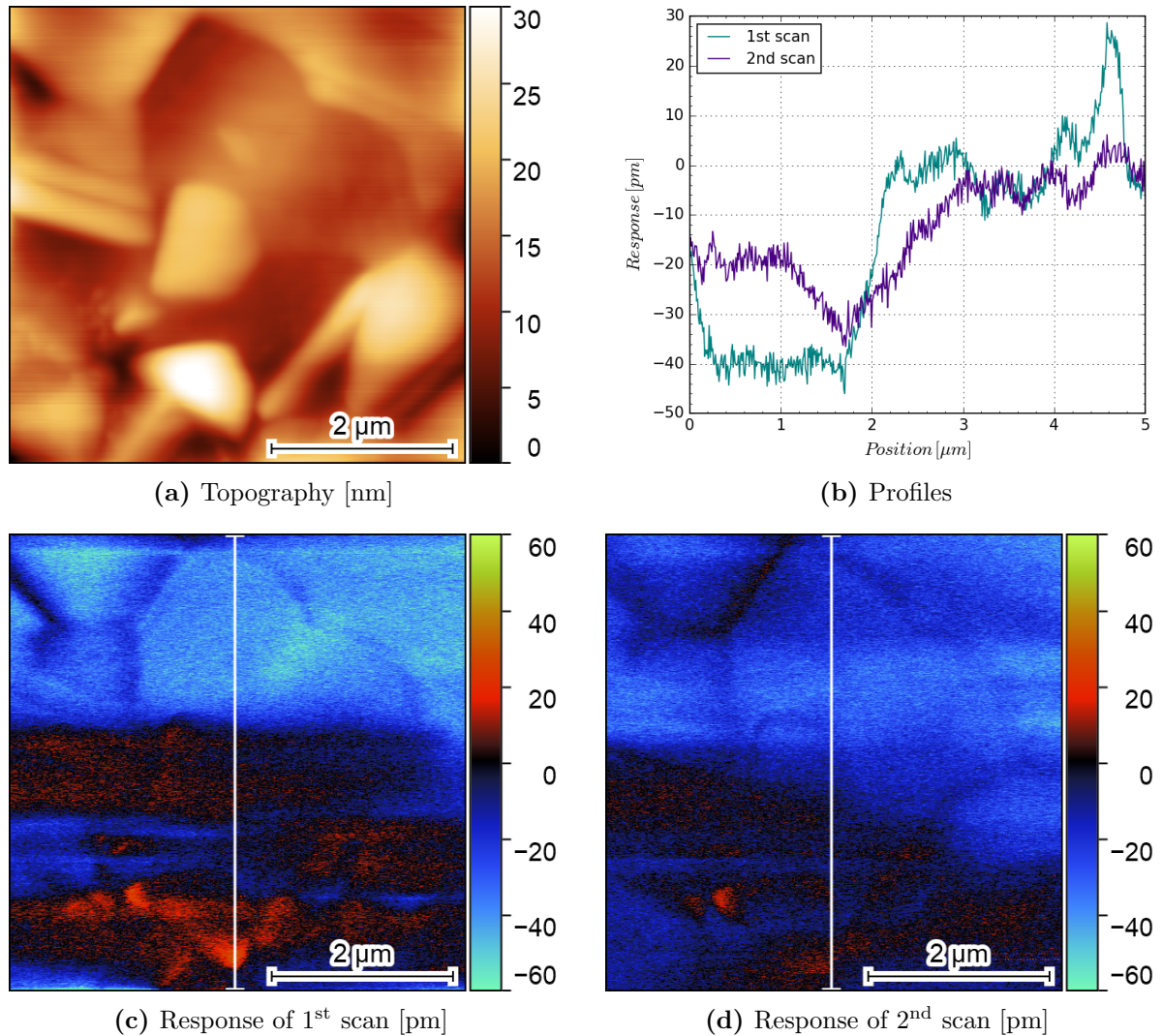


Figure 4.38: BNZT(2.5% Nb, 10% Zr) - Magnified domain structure obtained by a $5\ \mu\text{m} \times 5\ \mu\text{m}$ PFM measurement. The response of the PFM scan changes significantly over the two consecutive scans, as illustrated in the response figures (c) and (d), as well as in their profiles recorded along the vertical white lines in (c, d), which are presented in (b). The topography is displayed in (a).

Raising the Zr substitution to 20% leads to the effective disruption of long-range FE order in BNZT (cf. figure 4.39). No domain structure can be derived from the amplitude, phase or topography image (cf. figures 4.39b, 4.39c, and 4.39a). The former two are dominated by noise. The PD and AD are both monomodal with peaks at $7.5\ \text{pm}$ and -150° , respectively. Note that the horizontal scar in the upper quarter of the amplitude and phase image is topographic

cross-talk, caused by the small pore in that area. Considering supporting literature [42, 47, 91, 92], BNZT_2p5_20 is most likely comprised of PNRs sizing smaller than the lateral resolution limit of PFM [55, 77], which prevents the detection of a domain structure.

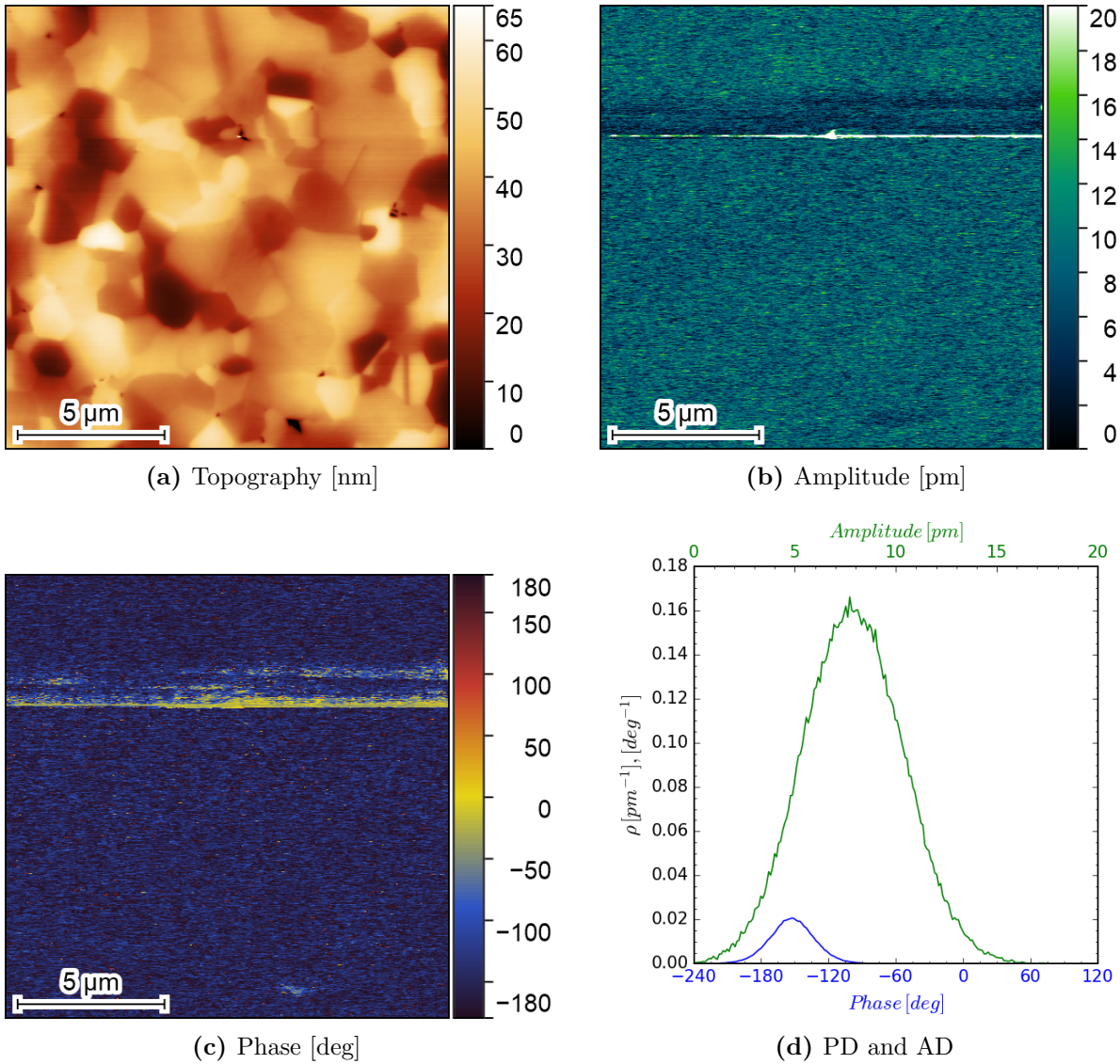


Figure 4.39: BNZT(2.5% Nb, 20% Zr) - Domain structure. Neither from the amplitude image (b), nor from the phase image (c), a domain structure can be derived. There is also no correlation between the topography (a) and the PFM signal. AD and PD (d) are both monomodal.

The sample with 2.5% Nb and 30% Zr exhibits some differences compared to the BNZT_2p5_20 (cf. figure 4.40). Phase and amplitude exhibit locally enhanced contrast along some scan lines, often coinciding with pores. Thus it can be assumed that the apparent contrast is not of true piezoelectric nature, but rather a topographical artefact. This is further confirmed by the magnified scan in figure 4.41, where phase and amplitude exhibit enhanced contrast in scan lines that cross the pore in the upper right. In general, the phase and amplitude images are dominated by noise. The monomodal AD has its peak at 7.5 pm and the PD appears to be bimodal with two partially intersecting peaks at -150° and -75° . On the basis of these measurements and by comparing them to results of similar single-substituted systems (BZT_40, BNT_10 and BNT_15)

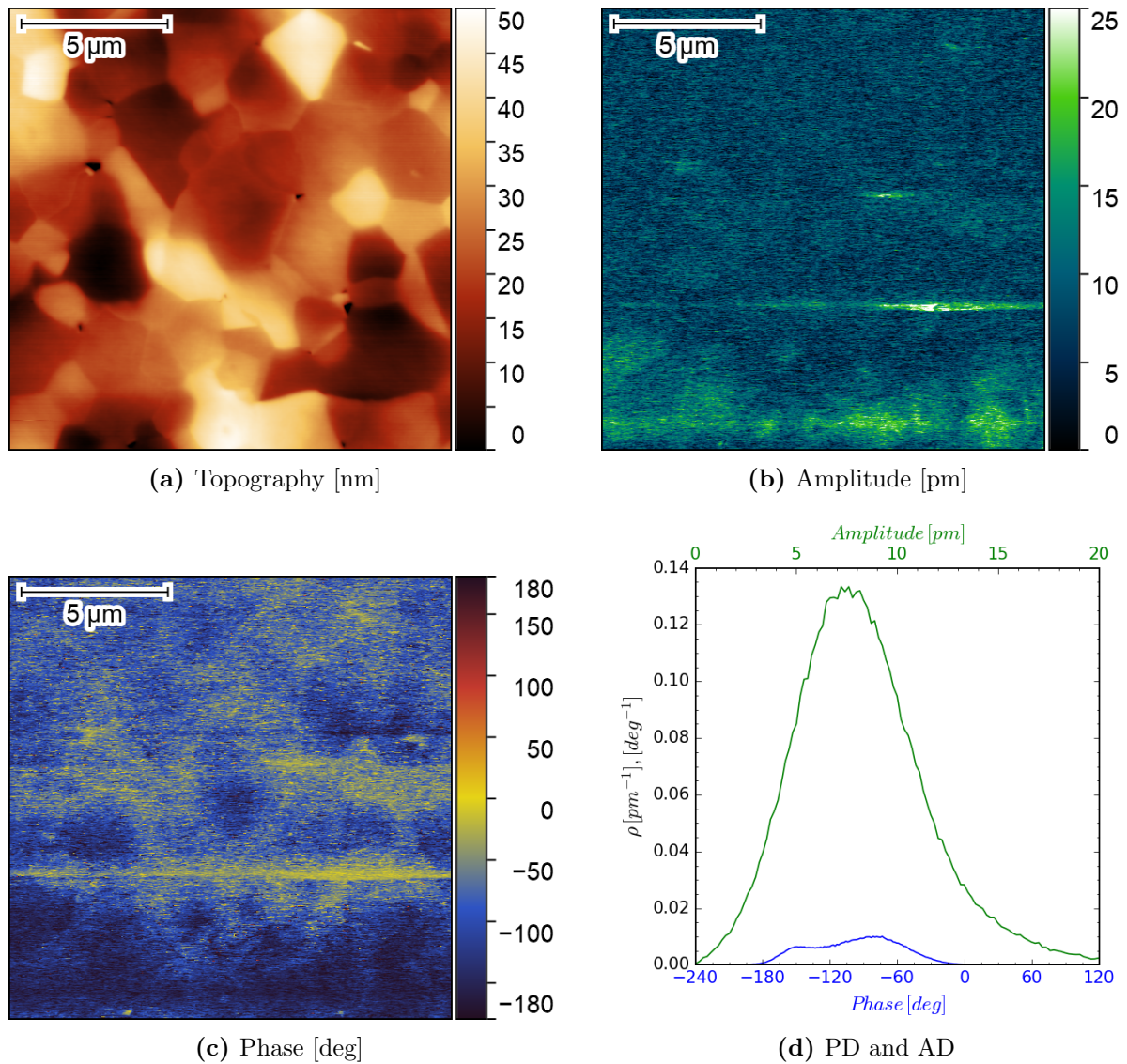


Figure 4.40: BNZT(2.5% Nb, 30% Zr) - Domain structure. Locally enhanced contrast in scan lines crossing pores can be obtained in the amplitude (b) and phase (c) image. The AD and PD (d) are monomodal and bimodal, respectively. The peaks of the PD partially intersect each other. The topography is displayed in (a). Locally enhanced PFM contrast can be obtained in scan lines coinciding with pores.

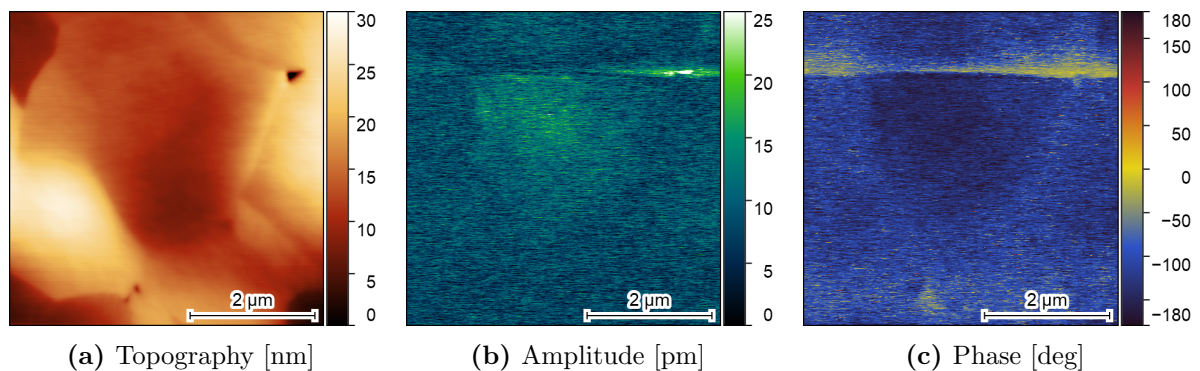


Figure 4.41: BNZT(2.5% Nb, 30% Zr) - Magnified domain structure obtained by a 5 μm x 5 μm PFM measurement. Enhanced contrast in amplitude (b) and phase (c) can be obtained in scan lines that cross pores, as illustrated by the upper right pore in the topography image (a).

[42, 47, 91, 92], it can be stated that BNZT_2p5_30 does not exhibit a domain structure that can be detected by PFM.

Upon 40% Zr substitution, no signs of long-range FE order are present (cf. figure 4.42). Phase and amplitude are entirely comprised of noise and do not exhibit any local artefacts (cf. figures 4.14c and 4.14b). Both the AD and PD in figure 4.14d are monomodal, with their respective peaks at 3.5 pm and 30°. It can be assumed that the domain structure of a system with such a high degree of substitution (the highest of all investigated samples), cannot be probed by PFM anymore due to the extraordinarily small PNRs and their expected high instability.

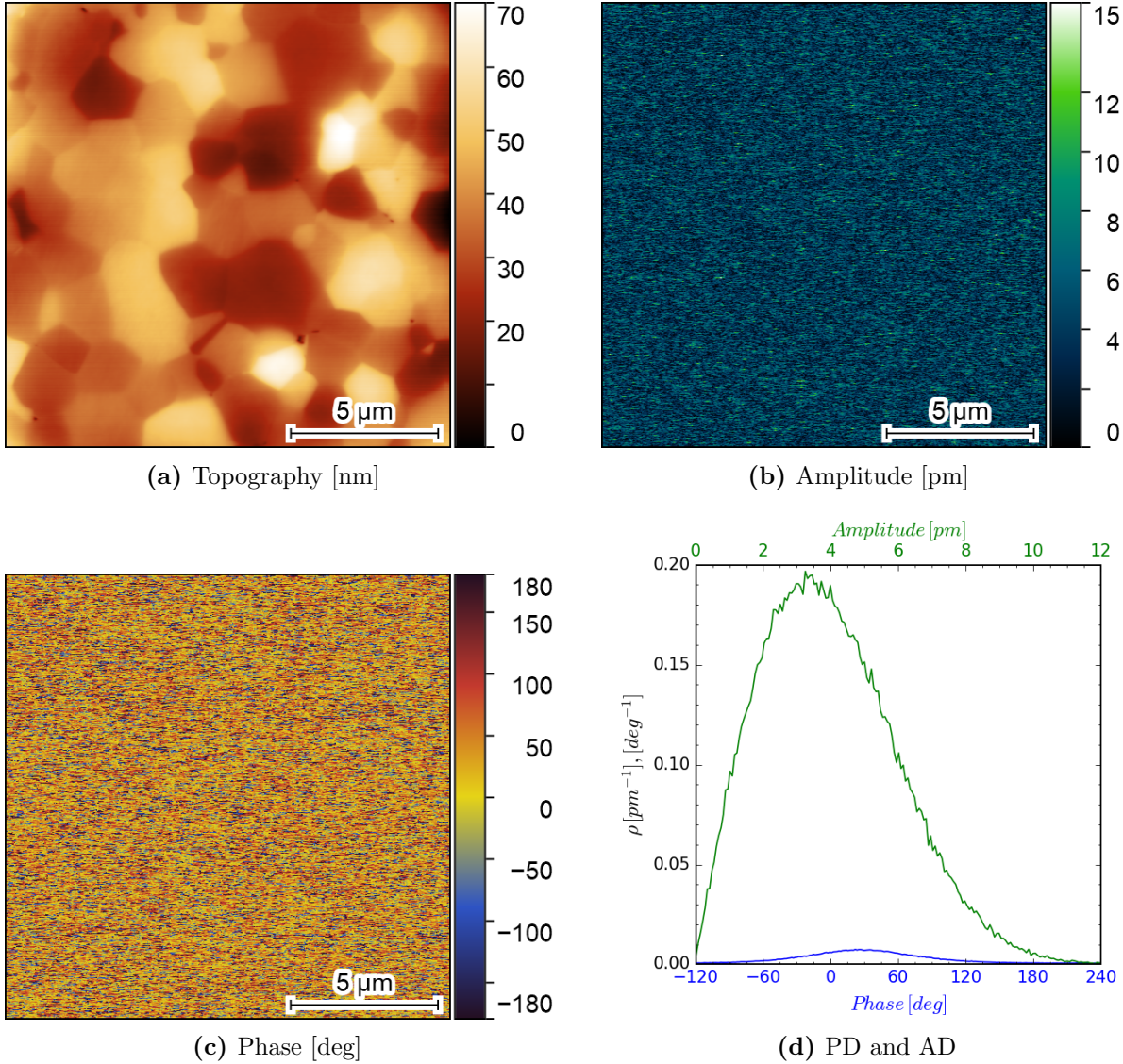


Figure 4.42: BZT(2.5% Nb, 40% Zr) - Domain structure. No domain structure can be derived from the amplitude image (b) or the phase image (c). There is no correlation between the topography (a) and the PFM signal. AD and PD (d) are both monomodal.

As before, a summary of the ADs and PDs of all BNZT samples is depicted in figure 4.43. The average amplitude is shifted towards lower values with increasing Zr substitution and the PDs of BT, BNZT_2p5_10, and BNZT_2p5_30 are bimodal. However, the bimodality of BNZT_2p5_30 is most likely caused by topography-related artefacts. The remaining PDs are monomodal.

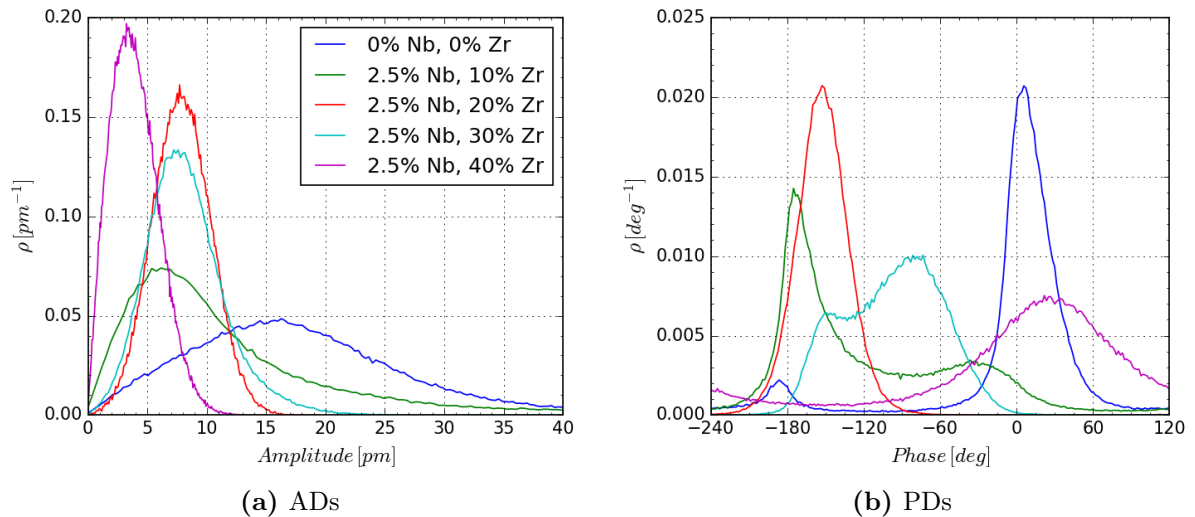


Figure 4.43: BNZT - Summary of the SF-PFM results. The ADs are displayed in (a) and the PDs in (b).

4.4.3 Polarization switching

The poling behaviour of BNZT with 2.5% Nb and 10% Zr is illustrated in figure 4.44. The pristine domain structure (cf. figure 4.44a) contains domain-like structures of elongated shape with a high positive response. Most of these structures (even outside the target area) vanish after the application of a negative DC bias in the target area, as illustrated in figure 4.44b. The shift of the response towards more negative values is also visible in the RDs as well as in the horizontal and vertical profiles (cf. figures 4.44e, 4.44d, and 4.44f). After 23h, all elongated-shaped structures vanished and the response image exhibits uniform and overall positive values, which are on average even higher than before poling (cf. figure 4.44c). The poling experiment of BNZT_2p5_10 consolidates the assumptions made in the SF-PFM section, namely that the measured domain structure of this sample appears to be subject to changes over time. Furthermore, it becomes highly unstable upon external stimulation with a high DC bias, as confirmed by the vanishing elongated structures of high response. The results suggest that the apparent domain structure can be disturbed by the application of a DC bias. However, it appears that the induced changes are delocalized and time-evolving. As already mentioned, it is unclear if this dynamic behaviour is mediated by the PFM measurements or if it is an inherent property of the system.

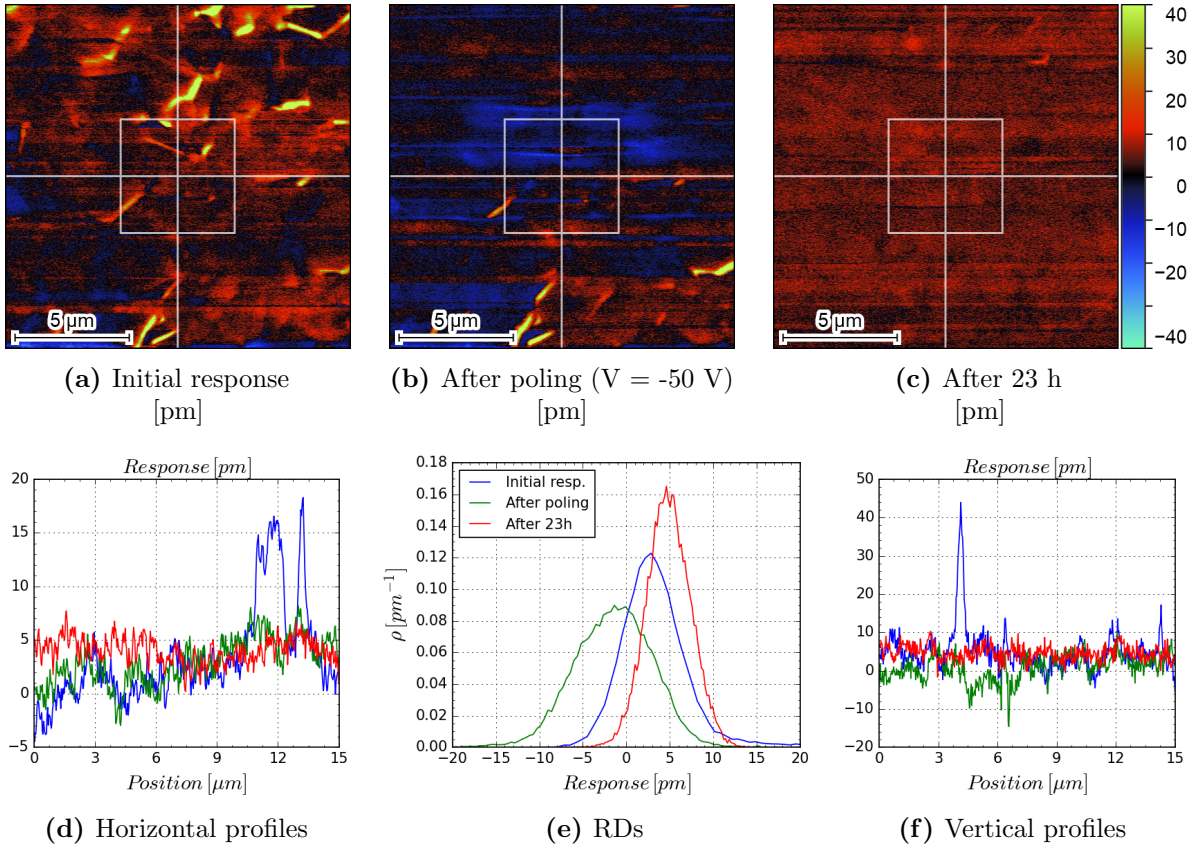


Figure 4.44: BNZT(2.5% Nb, 10% Zr) - Polarization switching experiment. The PFM response in (a) displays the pristine domain structure and (b) the response after poling with -50 V. The third scan (c) covers the same spot, 23 h after poling. Figure (d), (e), and (f) are the horizontal profiles (marked by the white horizontal lines), RDs (data extracted from within the squares), and vertical profiles (marked by the white vertical lines). The poled area was $5 \mu\text{m} \times 5 \mu\text{m}$ in size, as indicated by the white square.

BNZT_2p5_20 exhibits completely different behaviour upon poling compared BNZT_2p5_10 (cf. figure 4.45). Poling with -50 V leads to the inversion of the response from positive to negative values for the entire image (cf. figures 4.45a and 4.45b). Furthermore, this "switch" appears to be stable for at least 16 h, as illustrated in figure 4.45c. Immediately after poling, the response in the target area is enhanced compared to the surrounding, as visible in the profiles and RDs as well (cf. figures 4.45d, 4.45f, and 4.45e). The results suggest that no switching of FE polarization occurred in this experiment and the change of contrast is most likely explained by a change in surface potential [93], eventually caused by the spreading of charges during poling.

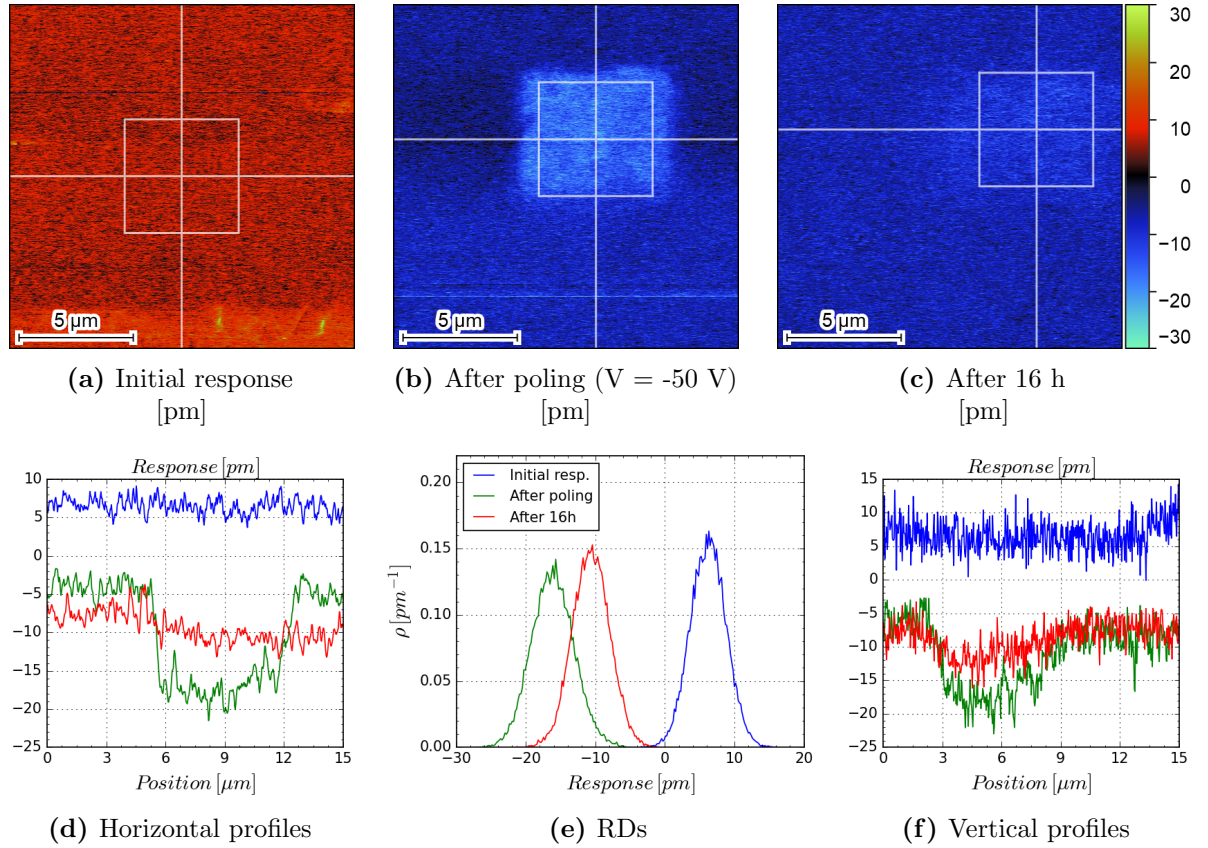


Figure 4.45: BNZT(2.5% Nb, 20% Zr) - Polarization switching experiment. The PFM response in (a) displays the pristine domain structure and (b) the response after poling with -50 V. The third scan (c) covers the same spot, 16 h after poling. Figure (d), (e), and (f) are the horizontal profiles (marked by the white horizontal lines), RDs (data extracted from within the squares), and vertical profiles (marked by the white vertical lines). The poled area was $5 \mu\text{m} \times 5 \mu\text{m}$ in size, as indicated by the white square.

BNZT_2p5_30 exhibits a similar, but not as pronounced behaviour upon poling, as illustrated in figure 4.46. The application of a DC bias of +50 V leads to a change in response from overall positive values (with some negative clusters in some areas) towards negative values everywhere, except in the target area (cf. figures 4.46a and 4.46b). The ineffectiveness of the poling attempt is also visible in the two profiles and the RDs in figures 4.46d, 4.46f, and 4.46e. After 18 h (cf. figure 4.46c), the domain structure exhibits a uniform (negative) response with weak localized contrast. The results do not indicate a real switch of FE polarization in BNZT_2p5_30.

The sample with the highest substitution, BNZT_2p5_40, exhibits almost no reaction upon poling with +50 V, except for a minor charge-induced change of contrast (cf. figure 4.47), which almost completely decayed after a second scan.

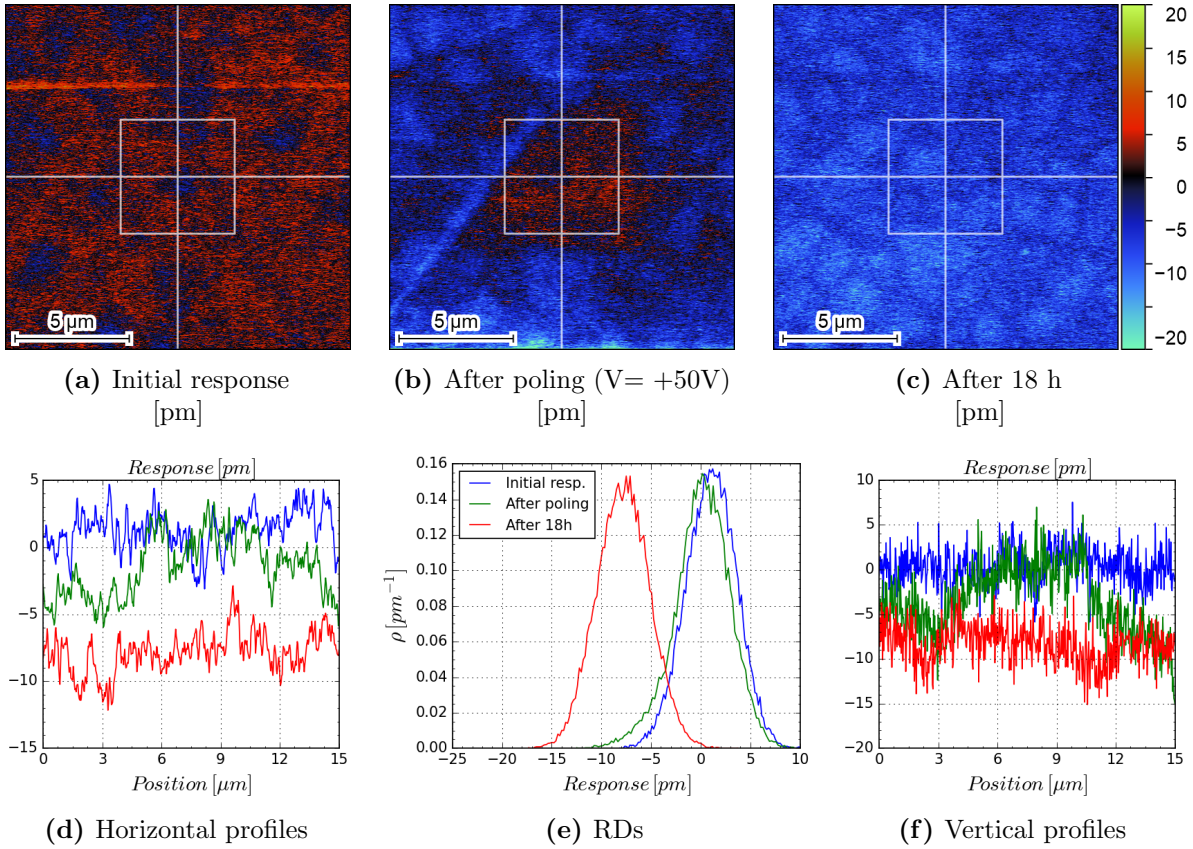


Figure 4.46: BNZT(2.5% Nb, 30% Zr) - Polarization switching experiment. The PFM response in (a) displays the pristine domain structure and (b) the response after poling with +50 V. The third scan (c) covers the same spot, 18 h after poling. Figure (d), (e), and (f) are the horizontal profiles (marked by the white horizontal lines), RDs (data extracted from within the squares), and vertical profiles (marked by the white vertical lines). The poled area was 5 μm x 5 μm in size, as indicated by the white square.

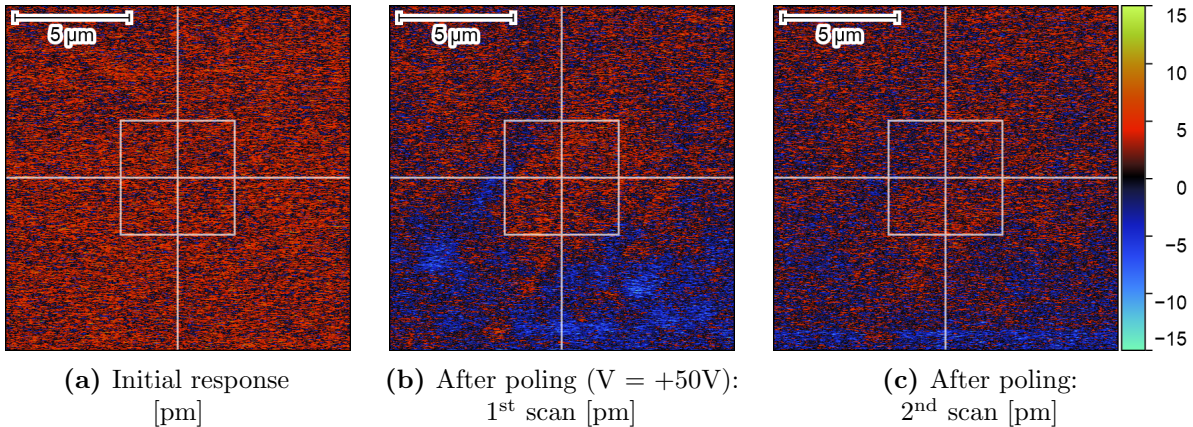


Figure 4.47: BNZT(2.5% Nb, 40% Zr) - Polarization switching experiment. The PFM response in (a) displays the pristine domain structure and (b) the response after poling with +50 V. The third scan in (c) is a 2nd scan after poling. The poled area was 5 μm x 5 μm in size, as indicated by the white square.

4.4.4 SS-PFM

The SS-PFM results are depicted in figure 4.48. As before, the focus will be laid on the Work of Switching parameter and Acceptance Rate. Co-substitution is highly efficient in perturbing the correlation between polar entities in BT, resulting in the swift relaxation of induced domains in the absence of an external electric field. This fast relaxation is confirmed by the overall low AmpOff Acceptance Rate of all BNZT samples. However, AmpOn exhibits an overall high Acceptance Rate in all samples, indicating a well-behaved active-field response. Higher Zr substitution leads to a reduction of the Work of Switching parameter, implying that the hysteresis loops become increasingly slim which corresponds to low hysteric energy losses. The AmpOn and AmpOff evolution of A_{fs} of BNZT_2p5_10 exhibit a peak around 75 °C, which could be an indicator for a DPT. However, since this system is only sparsely investigated, no reference can be taken into account to confirm this statement. Nevertheless, BZT and BNT systems with comparable substitution levels exhibit a DPT in the measured temperature range [42, 43, 91, 92, 101, 106]. So, it can be assumed that this holds in the BNZT_2p5_10 system as well. The other two systems exhibit a low and slowly declining A_{fs} in both AmpOn and AmpOff, suggesting a fully completed DPT. Note that it was only possible to acquire 5 data points for BNZT_2p5_30 because measurements at more elevated temperatures did not yield any hysteresis loops in AmpOff, indicating an immediate relaxation of newly formed domains.

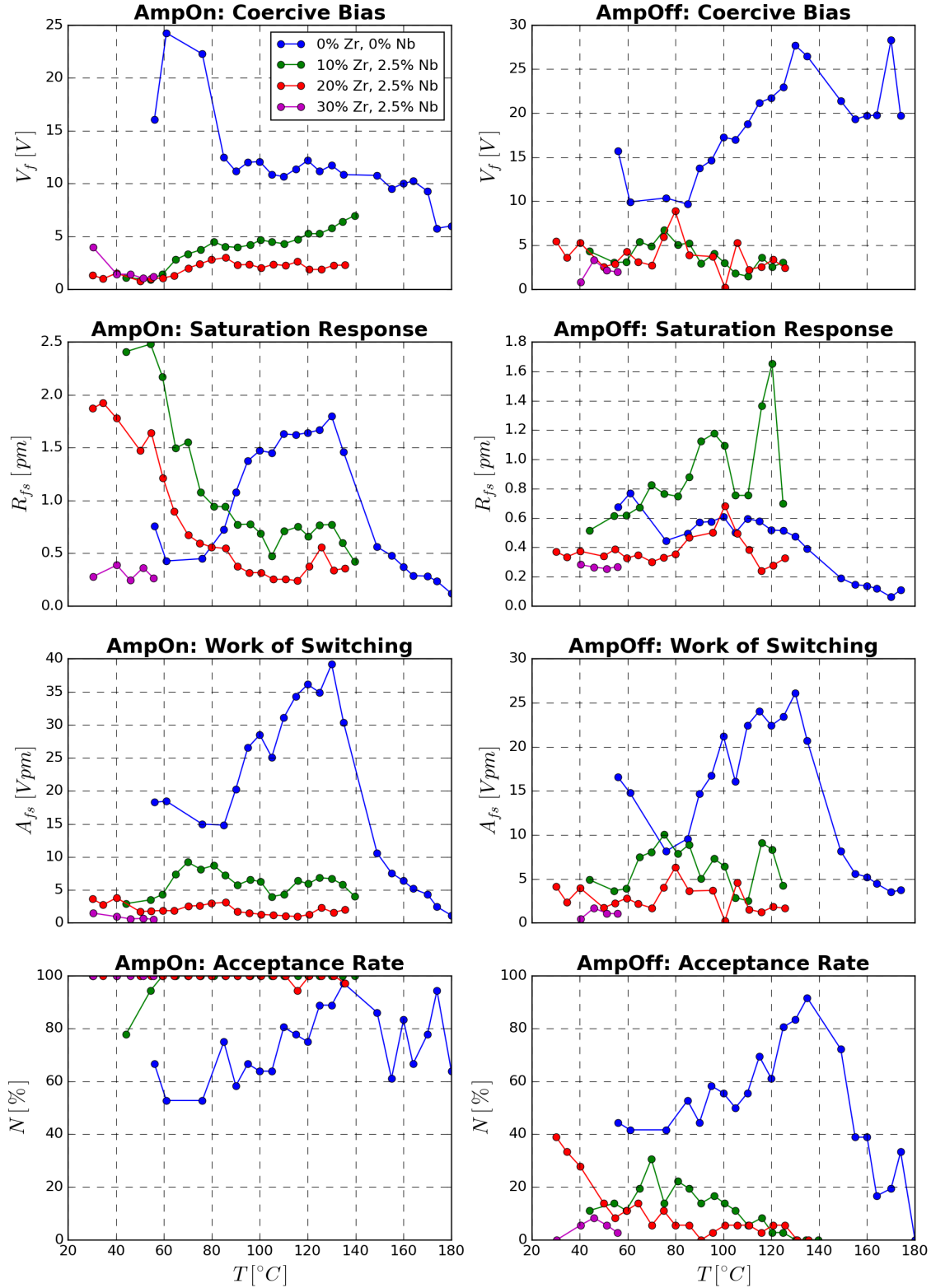


Figure 4.48: BNZT - SS-PFM results. The graphs display the temperature-dependent evolution of the Coercive Bias, Saturation Response and Work of Switching parameter from the fitting procedure (cf. equations 3.15, 3.16 and 3.17), as well as the Acceptance Rate from the filters described in section 3.5.2, for AmpOn and AmpOff. Both Work of Switching parameters are considerably lower for all samples compared to BT. Furthermore, the low Acceptance Rate of AmpOff indicates a swift relaxation of the newly formed domains, caused by the strong disruptive effect of co-substitution.

4.5 Conclusions derived from the measurements

The obtained results from the measurements exhibit a broad range of distinct details, which allow in combination with supporting literature to draw conclusions about the FE state of the four systems investigated. Table 4.1 represents the above-discussed results in a compact form.

The pure BT sample represents the model FE state. It exhibits a complex, herringbone-type domain structure resulting from spontaneous polarization. Furthermore, the polarization can be permanently switched by the application of a sufficiently high bias to the AFM tip. Relaxation of the newly formed domains occurs due to the role of strain and electrostatics in the microstructure. The SS-PFM results give insight into the local switching dynamics of the system, which are intrinsically temperature-dependent. More and more unit cells can be aligned when the temperature is raised and therefore, the Work of Switching parameter increases. However, when the temperature exceeds T_C , a PT from the FE to the PE phase occurs, which is indicated by a steep decline of the Work of Switching parameter. Even though the FE structure is considered fully disordered in the PE phase, local and only temporarily stable polar clusters [108] can still give rise to PFM hysteresis loops, even in the field-free case.

The partial replacement of the Ti ions by the considerably larger Zr ions results in random elastic fields, thus disturbing the FE order. At a substitution amount of 10%, the sample still exhibits a characteristic domain structure (intercepted lamellae), which can be probed by SF-PFM. Furthermore, the polarization can be locally switched by a biased tip and the newly formed domains remain stable for an extended period. The temperature-dependent SS-PFM results indicate the onset of a DPT due to the rise of the already considerably higher Work of Switching parameter. However, there is no indicator of a completed (diffuse) PT like in BT. The results and supporting literature confirm that BZT_10 can be considered an FE with a DPT. The diffuse nature of the PT in BZT_10 can also explain the absence of a drop in the Work of Switching parameter in the vicinity of T_m [41, 43, 44, 91, 92, 96].

At 20% Zr substitution, the FE domain structure becomes increasingly unstable, which is confirmed by the PFM measurements as well. A highly dynamic, single-domain structure can only be obtained in resonance PFM. Polarization switching is still possible, but unstable. The SS-PFM experiments indicate that a possible DPT has already happened due to the steady decline of the Work of Switching parameter. Taking supporting literature into account [91, 92, 96], BZT_20 can still be considered an FE with DPT, even though the increasingly unstable domains exhibit similarities to the PNRs in relaxors, e.g. the ergodicity.

BZT_30 and BZT_40 can both be considered ERs at RT since there is no detectable domain structure present. Furthermore, poling has no effect beyond the spreading of charge carriers on the surface, even though temporary switching followed by immediate relaxation cannot be ruled out. In contradiction, the low, but non-vanishing Work of Switching parameter suggests a temporary alignment of the PNRs. The results and supporting literature suggest that even though these RF systems appear fully disordered, they exhibit traces of ferroelectricity [41, 43, 91].

Heterovalent substitution by e.g. Nb^{5+} introduces random electric fields into BT, making it more effective than homovalent substitution. At 2.5% Nb substitution, BNT still exhibits a lamellar

FE domain structure with domains of approximately 100 nm width. Switching the polarization is possible, but numerous small domains relax after enough time has passed. In the past, BNT_2p5 was considered an FE with one DPT [42], but a recent contribution suggests the occurrence of three PTs like in BT [106]. The SS-PFM experiments indicate the occurrence of more than one PT in this system as well. An initial steep decline of the Work of Switching parameter indicates a completed PT from orthorhombic to tetragonal crystal structure. Upon further heating, the Work of Switching parameter peaks at 90 °C, indicating the onset of the (diffusive) FE-PE PT. Summarized, BNT_2p5 can be considered an FE, with three (diffusive) PTs.

Raising the substitution amount to 5% Nb already causes a disruption of FE order in BNT comparable to BZT_20. No domain structure can be derived from the SF-PFM measurements, even though there is a locally enhanced amplitude in the vicinity of some grain boundaries and pores. Polarization switching results in the local accumulation of charge carriers, most likely Ba or Ti vacancies, accompanied by an irreversible change in topography in the poled area. Any induced PFM contrast vanishes completely after an extended period, indicating highly unstable or non-present switching of FE polarization. The evolution of the temperature-dependent Work of Switching parameter indicates the onset of a (diffuse) PT. However, the peak at 120 °C contradicts reported values which are considerably lower [42, 101, 106]. With this information, BNT_5 can be classified as being in the transition zone from an FE with DPT to an ER, with dynamic nano-sized domains smaller than the lateral resolution of PFM [55, 77].

At 7% of Nb substitution, no domain structure can be derived from the SF-PFM experiments and poling leads to the accumulation of charge carriers accompanied by an irreversible change in topography. BNT_7 exhibits a considerably higher Work of Switching parameter than BNT_5, which can be attributed to an increasingly dominant role of ESM contrast besides SS-PFM contrast. The evolution of the temperature-dependent Work of Switching parameter indicates a broad DPT at 90 °C. However, the obtained T_m is considerably higher than values reported elsewhere [42, 106]. Summarized, the findings and supporting literature [43, 101] suggest that this system is already in the RF state and is most likely behaving like an ER close to its T_m at RT.

The last two samples with the highest Nb substitution, BNT_10 and BNT_15, can be considered ERs in the measured temperature range. SF-PFM does not yield any domain structure in both samples, but they differ in their poling behaviour. The former exhibits a remanent, time-evolving change of response upon poling accompanied by an irreversible topography change, while the latter does not exhibit any significant change in PFM response or topography. Most likely, the difference in poling behaviour can be explained by the different concentrations of charge-balancing vacancies. In both samples, the temperature-dependent Work of Switching parameter declines upon heating, with the difference that all values of BNT_15 are significantly lower than the ones in BNT_10. As stated above, an explanation for that could be an impediment of charge carrier accumulation caused by the intrinsically high vacancy concentration in BNT_15 (i.e. leading to the attenuation of ESM contrast) or by the fact, that BNT_15 is well above its T_m in the measured temperature range (i.e. translating to increased instability of the PNRs). Other reports about these compositions [42, 43, 101, 106] agree well with the measured results and support the assumption that both can be considered RFs.

Co-substitution is an effective means of disrupting FE order in BT, thus inducing the RF state. This strong disruption is already present in the lowest co-substituted sample, BNZT_2p5_10. A time-evolving, unstable domain structure can be obtained by SF-PFM, which tends to exhibit declining PFM contrast over multiple consecutive scans. Furthermore, electrostatic artefacts emerging from charges appear to play a significant role during PFM image acquisition. The application of a high DC bias leads to the non-local disturbance of the domain structure, hence FE switching is not the right term for this behaviour. The non-local change of the acquired response can most probably be assigned to a mechanism emerging from FE screening charges on the surface [107]. The SS-PFM results indicate a high instability of the domains in the field-free case and the overall low Work of Switching parameter exhibits a broad peak at approximately 75 °C, indicating a DPT. Since these co-substituted systems are only sparsely investigated [47], an estimation of the FE state of this system is not straightforward. Nevertheless, the measurements suggest that BNZT_2p5_10 is on the verge of being an RF, since it behaves similarly to the single-substituted FE-RF transition systems with comparable substitution levels (BZT_20, BNT_5, and BNT_7) [42, 43, 91, 92, 101, 106]. Moreover, the SS-PFM experiments suggest that the domains of this system are significantly more unstable compared to BZT and BNT.

BNZT_2p5_20, BNZT_2p5_30, and BNZT_2p5_40 can all be considered RFs, being in the ER state at RT. No clear domain structure can be derived from these systems and poling shows decreasing efficacy with increasing substitution. The Work of Switching parameters are low and slowly declining upon heating, suggesting a completed DPT. These systems behave similarly to the single-substituted systems with the highest substitution (BZT_40 and BNT_15) [42, 43, 91, 92, 106], indicating that they are comprised of highly dynamic PNRs which only instantaneously react to an external field with an orientational alignment. No indicator of a remanent orientational stabilization of the PNRs could be obtained.

Sample	SF-PFM	PFM poling	SS-PFM
BT	Herringbone-type domain structure; bimodal PD	Polarization fully switched; partial relaxation after 117 h	Rising A_{fs} up to T_C , then steep decline due to PT
BZT_10	Intercepted lamellar domain structure; bimodal PD	Full switch of polarization; minor relaxation after 18 h	Rising A_{fs} in the probed temp. range; no indicator for completed DPT
BZT_20	Single domain grains; PFM contrast only at contact resonance	Temporary polarization switch possible, but highly unstable	Steeply declining A_{fs} in the probed temp. range; DPT likely completed
BZT_30	No detectable domain structure; broad monomodal PD	No detected change of PFM contrast, except minor charge effects	-
BZT_40	No detectable domain structure, monomodal PD	No detected change of PFM contrast; charge effects in some grains	Low and steadily declining A_{fs} , all data points are above T_m
BNT_2p5	Lamellar domain structure with 100 nm width; bimodal PD	Polarization switching successful; partial relaxation after 18 h	First falling, then raising A_{fs} ; PT at 90 °C with steadily declining A_{fs}
BNT_5	No detectable domain structure; locally enhanced amplitude	Unstable contrast from charges; irreversible topography change	Raising A_{fs} until broad peak at 120 °C; declining A_{fs} indicating DPT
BNT_7	No detectable domain structure; monomodal PD	Unstable contrast from charges; irreversible topography change	Probable high ESM contribution; A_{fs} peaks at 90 °C indicating a DPT
BNT_10	No detectable domain structure; monomodal PD	Stable contrast from charges; irreversible topography change	Steeply declining A_{fs} indicating completed DPT; high ESM contribution
BNT_15	No detectable domain structure; monomodal PD	Minor unstable contrast from charges; no topography change	Low and declining A_{fs} ; DPT completed; weak ESM contribution
BNZT_2p5_10	Unstable domain structure; vanishing contrast; bimodal PD	Poling disturbs domain structure non-locally; uniform response	Flat rise of overall low A_{fs} ; peak around 75 °C indicating DPT
BNZT_2p5_20	No detectable domain structure; monomodal PD	Inversion of response; no sign of switching except charge accumulation	Low and steady declining A_{fs} ; DPT completed
BNZT_2p5_30	No detectable domain structure; local contrast clusters; monomodal PD	Inversion of response outside of square first, later change inside	Low and steady declining A_{fs} ; DPT completed
BNZT_2p5_40	No detectable domain structure; monomodal PD	Negligible change of contrast; temporary response change by charges	-

Table 4.1: Summary of the experimental results of all samples. A_{fs} is the Work of Switching parameter.

5 Summary and outlook

In this work, B-site substituted barium titanate was investigated by Piezoresponse Force Microscopy (PFM) to uncover changes in ferroelectric behaviour upon transition from a ferroelectric to a relaxor ferroelectric, or short, relaxor. Single Frequency PFM was used to image the pristine domain structure of these systems and local poling of the domain structure was conducted to probe the reaction to a highly localized field. Furthermore, the local polarization switching dynamics were determined for the active-field and field-free case. Due to the great extent of generated data at various temperatures, a semi-automated algorithm was developed to correct, clean, and evaluate the data to derive conclusions about the temperature-dependent polarization switching dynamics in all compositions. The results confirm that the co-substitution of Nb and Zr is most effective in disrupting ferroelectric order and inducing the relaxor state, followed by heterovalent Nb substitution and homovalent Zr substitution as the least effective means.

Zr-substituted barium titanate exhibits its transition from the ferroelectric to the relaxor state between 20% and 30% of substitution, which is further confirmed by various reports in literature. Above 20% Zr substitution, no domain structure can be derived from the PFM measurements, and polarization switching is either highly unstable or not present. Still, hysteresis loops are detected in Switching Spectroscopy PFM even at the highest Zr substitution level, which indicates localized ferroelectricity on the nanoscale.

In Nb-substituted systems, a concentration between 5% Nb and 7% Nb is already sufficient to transform the ferroelectric into a relaxor, causing effects comparable to Zr-substituted barium titanate. Additional electrochemical contrast can also be detected upon higher Nb substitution, which leads to non-piezoelectric signal generation during the image acquisition and even irreversible material swelling from poling. Furthermore, the coexistence of contrast emerging from ferroelectricity and charge carriers like vacancies impedes the straightforward identification of phase transitions in the temperature-dependent PFM hysteresis loop measurements. Nevertheless, the measured systems qualitatively agree with the findings in literature. A newly discovered phase transition was identified in the system with the lowest Nb substitution.

Co-substituted barium titanate exhibits relaxor behaviour upon simultaneous substitution with 2.5% Nb and 20% Zr, even though it must be mentioned that there is only little published work on this material system, and further investigation with complementary methods is necessary to clarify open questions. It appears that the simultaneous incorporation of both substituents leads to the swift relaxation of newly formed domains, as this system exhibits the lowest number of proper PFM hysteresis loops throughout all concentrations. Hence, co-substituted barium titanate proves to be a promising material for high-energy and low-loss lead-free dielectrics, provided that further investigations on the composition-dependent properties are conducted in order to find the optimal composition for its application.

Even though relaxors have been investigated for more than half a century, there are still numerous open questions about the true nature behind their unique behaviour among dielectrics. Due to the variety of mechanisms that induce relaxor behaviour and their complexity, only incremental advances are made in deciphering these systems, thus keeping PFM and complementary methods highly relevant for future research on this topic.

A broad range of additional experiments is within possibility, as the AFM counts among the most versatile characterization instruments in material science. The three already conducted methods could be extended in their accuracy and lucidity by combining them with other AFM modes. By conducting Kelvin Probe Force Microscopy experiments, the local work function of the material can be obtained and used to correct the electrostatic contribution in succeeding PFM scans, thus reducing unwanted, non-piezoelectric contrast. The square-in-square poling experiment, a more sophisticated procedure where a smaller square is poled within a larger square of antiparallel vertical polarization, could be combined with numerous post-poling PFM scans to obtain information about the domain wall kinetics.

In addition, the Switching Spectroscopy PFM experiments can be improved as well, by acquiring the switching dynamics on a denser grid (64 x 64 or higher) before the temperature-dependent measurements. By that means, the Switching Spectroscopy PFM results can be correlated to the topography, thus facilitating a more straightforward evaluation by identifying the origin of heavily distorted hysteresis loops. Further, it is advisable to perform repeated PFM frequency tunes to effectively monitor changes in the tip surface contact parameters. The superposition of hysteresis-forming mechanisms with different origins (e.g. electromechanical contribution, electrochemical strain and joule heating) in Switching Spectroscopy PFM impedes straightforward evaluation of the hysteresis loops. A physics-informed machine learning approach [109, 110] could facilitate the data analysis of ambiguous Switching Spectroscopy PFM results.

PFM proves to be a reliable method to characterize ferroelectric and relaxor systems on the nanoscale, but the data interpretation must be conducted with caution to avoid wrong conclusions, as non-piezoelectric artefacts can contribute to the signal. Therefore, PFM as a standalone method is not sufficient to assert whether a material is ferroelectric or not.

References

- [1] V. Veerapandiyan, F. Benes, T. Gindel, and M. Deluca, “Strategies to improve the energy storage properties of perovskite lead-free relaxor ferroelectrics: A review,” *Materials*, vol. 13, no. 24, p. 5742, Jan. 2020, Number: 24 Publisher: Multidisciplinary Digital Publishing Institute. DOI: 10.3390/ma13245742.
- [2] M. S. Whittingham, “History, evolution, and future status of energy storage,” *Proceedings of the IEEE*, vol. 100, pp. 1518–1534, Special Centennial Issue May 2012, Conference Name: Proceedings of the IEEE. DOI: 10.1109/JPROC.2012.2190170.
- [3] M.-J. Pan and C. A. Randall, “A brief introduction to ceramic capacitors,” *IEEE Electrical Insulation Magazine*, vol. 26, no. 3, pp. 44–50, May 2010. DOI: 10.1109/MEI.2010.5482787.
- [4] T. Christen and M. W. Carlen, “Theory of ragone plots,” *Journal of Power Sources*, vol. 91, no. 2, pp. 210–216, Dec. 1, 2000. DOI: 10.1016/S0378-7753(00)00474-2.
- [5] N. H. Fletcher, A. D. Hilton, and B. W. Ricketts, “Optimization of energy storage density in ceramic capacitors,” *Journal of Physics D: Applied Physics*, vol. 29, no. 1, p. 253, Jan. 1996. DOI: 10.1088/0022-3727/29/1/037.
- [6] L. Dou, Y.-H. Lin, and C.-W. Nan, “An overview of linear dielectric polymers and their nanocomposites for energy storage,” *Molecules*, vol. 26, no. 20, p. 6148, Oct. 12, 2021. DOI: 10.3390/molecules26206148.
- [7] J. O. Gentner, P. Gerthsen, N. A. Schmidt, and R. E. Send, “Dielectric losses in ferroelectric ceramics produced by domain-wall motion,” *Journal of Applied Physics*, vol. 49, no. 8, pp. 4485–4489, Aug. 12, 2008. DOI: 10.1063/1.325453.
- [8] P. Zhao *et al.*, “High-performance relaxor ferroelectric materials for energy storage applications,” *Advanced Energy Materials*, vol. 9, no. 17, p. 1803048, 2019. DOI: 10.1002/aenm.201803048.
- [9] H. Pan *et al.*, “Ultrahigh energy storage in superparaelectric relaxor ferroelectrics,” *Science*, vol. 374, no. 6563, pp. 100–104, Oct. 2021. DOI: 10.1126/science.abi7687.
- [10] Y. Yamashita, K. Harada, and S. Saitoh, “Recent applications of relaxor materials,” *Ferroelectrics*, vol. 219, no. 1, pp. 29–36, Nov. 1, 1998, Publisher: Taylor & Francis. DOI: 10.1080/00150199808213495.
- [11] A. J. Bell and O. Deubzer, “Lead-free piezoelectrics—the environmental and regulatory issues,” *MRS Bulletin*, vol. 43, no. 8, pp. 581–587, Aug. 1, 2018. DOI: 10.1557/mrs.2018.154.
- [12] M. Stewart, M. Cain, and D. Hall, “Ferroelectric hysteresis measurement and analysis,” *Report CMMT (A)*, vol. 152, Jan. 1, 1999.
- [13] J. Yang, *An Introduction to the Theory of Piezoelectricity*. Kluwer Academic Publishers, 2005, Publication Title: An Introduction to the Theory of Piezoelectricity. DOI: 10.1007/b101799.

- [14] J. Curie and P. Curie, “Développement par compression de l’électricité polaire dans les cristaux hémihédres à faces inclinées,” *Bulletin de la Société minéralogique de France*, vol. 3, no. 4, pp. 90–93, 1880, Publisher: PERSEE Program. DOI: 10.3406/bulmi.1880.1564.
- [15] A. von Hippel, “Piezoelectricity, ferroelectricity, and crystal structure,” *Zeitschrift für Physik A Hadrons and nuclei*, vol. 133, no. 1, pp. 158–173, Sep. 1, 1952. DOI: 10.1007/BF01948692.
- [16] G. Lippmann, “Principe de conservation de l’électricité,” *Ann. Chim. Phys.*, vol. 24, pp. 145–178, 1881.
- [17] J. Curie and P. Curie, “Contractions et dilatations produites par des tensions dans les cristaux hémihédres à faces inclinées,” *C R Acad Sci Gen*, vol. 93, pp. 1137–1140, Jan. 1, 1881.
- [18] R. Gerhard, “Piezoelectricity and electrostriction,” in *Electromechanically Active Polymers: A Concise Reference*, ser. Polymers and Polymeric Composites: A Reference Series, F. Carpi, Ed., Cham: Springer International Publishing, 2016, pp. 489–507. DOI: 10.1007/978-3-319-31530-0_21.
- [19] R. E. Hummel, *Electronic Properties of Materials*. Springer New York, 2011, Publication Title: Electronic Properties of Materials. DOI: 10.1007/978-1-4419-8164-6.
- [20] J. Grindlay, “Electrostriction,” *Physical Review*, vol. 160, no. 3, pp. 698–701, Aug. 15, 1967. DOI: 10.1103/PhysRev.160.698.
- [21] R. E. Newnham, V. Sundar, R. Yimnirun, J. Su, and Q. M. Zhang, “Electrostriction: Nonlinear electromechanical coupling in solid dielectrics,” *The Journal of Physical Chemistry B*, vol. 101, no. 48, pp. 10 141–10 150, Nov. 1, 1997, Publisher: American Chemical Society. DOI: 10.1021/jp971522c.
- [22] R. E. Newnham, *Properties of Materials: Anisotropy, Symmetry, Structure*. Oxford University Press, Nov. 11, 2004. DOI: 10.1093/oso/9780198520757.001.0001.
- [23] A. J. Moulson and J. M. Herbert, *Electroceramics: Materials, Properties, Applications*, 1st ed. Wiley, Apr. 29, 2003. DOI: 10.1002/0470867965.
- [24] S. Krichen and P. Sharma, “Flexoelectricity: A perspective on an unusual electromechanical coupling,” *Journal of Applied Mechanics*, vol. 83, no. 3, p. 030 801, Mar. 1, 2016. DOI: 10.1115/1.4032378.
- [25] P. V. Yudin and A. K. Tagantsev, “Fundamentals of flexoelectricity in solids,” *Nanotechnology*, vol. 24, no. 43, p. 432 001, Nov. 1, 2013. DOI: 10.1088/0957-4484/24/43/432001.
- [26] V. Wadhawan, *Introduction to Ferroic Materials*, 0th ed. CRC Press, Dec. 21, 2000. DOI: 10.1201/9781482283051.
- [27] M. Fiebig, T. Lottermoser, D. Meier, and M. Trassin, “The evolution of multiferroics,” *Nature Reviews Materials*, vol. 1, no. 8, p. 16 046, Jul. 5, 2016. DOI: 10.1038/natrevmat.2016.46.
- [28] W. Känzig, “Ferroelectrics and antiferroelectrics,” *Solid State Physics - Advances in Research and Applications*, vol. 4, pp. 1–197, C Jan. 1957, Publisher: Academic Press. DOI: 10.1016/S0081-1947(08)60154-X.

- [29] N. Setter, “What is a ferroelectric—a materials designer perspective,” *Ferroelectrics*, vol. 500, no. 1, pp. 164–182, Aug. 8, 2016, Publisher: Taylor & Francis. DOI: 10.1080/00150193.2016.1232104.
- [30] A. Pramanick, A. D. Prewitt, J. S. Forrester, and J. L. Jones, “Domains, domain walls and defects in perovskite ferroelectric oxides: A review of present understanding and recent contributions,” *Critical Reviews in Solid State and Materials Sciences*, vol. 37, no. 4, pp. 243–275, Dec. 1, 2012, Publisher: Taylor & Francis. DOI: 10.1080/10408436.2012.686891.
- [31] G. Arlt, “Twinning in ferroelectric and ferroelastic ceramics: Stress relief,” *Journal of Materials Science*, vol. 25, no. 6, pp. 2655–2666, Jun. 1990. DOI: 10.1007/BF00584864.
- [32] G. Smolensky, “Ferroelectrics with diffuse phase transition,” *Ferroelectrics*, vol. 53, no. 1, pp. 129–135, Apr. 1, 1984, Publisher: Taylor & Francis. DOI: 10.1080/00150198408245041.
- [33] W. Kleemann, “Random fields in relaxor ferroelectrics — a jubilee review,” *Journal of Advanced Dielectrics*, vol. 02, no. 2, p. 1241001, Apr. 2012, Publisher: World Scientific Publishing Co. DOI: 10.1142/S2010135X12410019.
- [34] Z. G. Ye, “Relaxor ferroelectric complex perovskites: Structure, properties and phase transitions,” *Key Engineering Materials*, vol. 155-156, pp. 81–122, 1998, Publisher: Trans Tech Publications Ltd. DOI: 10.4028/www.scientific.net/KEM.155-156.81.
- [35] J. Hlinka, “Do we need the ether of polar nanoregions?” *Journal of Advanced Dielectrics*, vol. 02, no. 2, p. 1241006, Apr. 2012, Publisher: World Scientific Publishing Co. DOI: 10.1142/S2010135X12410068.
- [36] S. Kamba *et al.*, “Dielectric dispersion of the relaxor PLZT ceramics in the frequency range 20 Hz-100 THz,” *Journal of Physics: Condensed Matter*, vol. 12, no. 4, p. 497, 1999, ISSN: 0953-8984. [Online]. Available: https://www.academia.edu/16622539/Dielectric_dispersion_of_the_relaxor_PLZT_ceramics_in_the_frequency_range_20_Hz_100_THz (visited on 04/17/2023).
- [37] A. A. Bokov and Z.-G. Ye, “Recent progress in relaxor ferroelectrics with perovskite structure,” *Journal of Materials Science*, vol. 41, no. 1, pp. 31–52, Jan. 1, 2006. DOI: 10.1007/s10853-005-5915-7.
- [38] S. K. Meena, A. Dashora, N. L. Heda, and B. L. Ahuja, “Compton spectroscopy and electronic structure study for tetragonal barium titanate,” *Radiation Physics and Chemistry*, vol. 158, pp. 46–52, May 1, 2019. DOI: 10.1016/j.radphyschem.2019.01.007.
- [39] P. Moretti, G. Godefroy, and J. M. Billbault, “Optical and electrical properties of Nb doped BaTiO₃ single crystals grown either by the KF flux or the pulling method,” *Ferroelectrics*, vol. 37, no. 1, pp. 721–724, Oct. 1, 1981, Publisher: Taylor & Francis. DOI: 10.1080/00150198108223533.
- [40] V. Buscaglia and C. A. Randall, “Size and scaling effects in barium titanate. An overview,” *Journal of the European Ceramic Society*, 16th European Inter-Regional Conference on Ceramics (CIEC16), vol. 40, no. 11, pp. 3744–3758, Sep. 1, 2020. DOI: 10.1016/j.jeurceramsoc.2020.01.021.

- [41] R. Farhi, M. El Marssi, A. Simon, and J. Ravez, “A raman and dielectric study of ferroelectric ceramics,” *The European Physical Journal B - Condensed Matter and Complex Systems*, vol. 9, no. 4, pp. 599–604, Jun. 1, 1999. DOI: 10.1007/s100510050803.
- [42] R. Farhi, M. El Marssi, A. Simon, and J. Ravez, “Relaxor-like and spectroscopic properties of niobium modified barium titanate,” *The European Physical Journal B - Condensed Matter and Complex Systems*, vol. 18, no. 4, pp. 605–610, Dec. 1, 2000. DOI: 10.1007/s100510070008.
- [43] V. Veerapandiyani *et al.*, “Origin of relaxor behavior in barium-titanate-based lead-free perovskites,” *Advanced Electronic Materials*, vol. 8, no. 2, p. 2100812, 2022. DOI: 10.1002/aelm.202100812.
- [44] A. Pramanick *et al.*, “Stabilization of polar nanoregions in Pb-free ferroelectrics,” *Physical Review Letters*, vol. 120, no. 20, p. 207603, May 18, 2018, Publisher: American Physical Society. DOI: 10.1103/PhysRevLett.120.207603.
- [45] A. K. Kalyani, A. Senyshyn, and R. Ranjan, “Polymorphic phase boundaries and enhanced piezoelectric response in extended composition range in the lead free ferroelectric $\text{BaTi}_{1-x}\text{Zr}_x\text{O}_3$,” *Journal of Applied Physics*, vol. 114, no. 1, p. 014102, Jul. 1, 2013. DOI: 10.1063/1.4812472.
- [46] T.-B. Wu and J.-N. Lin, “Transition of compensating defect mode in niobium-doped barium titanate,” *Journal of the American Ceramic Society*, vol. 77, no. 3, pp. 759–764, 1994. DOI: 10.1111/j.1151-2916.1994.tb05362.x.
- [47] J. P. Jwala, O. Subohi, and M. M. Malik, “Influence of B-site modification by hetrovalent (Nb^{5+}) and isovalent (Zr^{4+}) dopants in BaTiO_3 on its dielectric and electrical properties synthesized by novel sol gel route,” *Materials Research Express*, vol. 6, no. 9, p. 096308, Jul. 2019, Publisher: IOP Publishing. DOI: 10.1088/2053-1591/ab2dee.
- [48] OverlordQ, *Atomic force microscope block diagram*, Publication Title: Wikimedia Commons, Apr. 2020. [Online]. Available: https://commons.wikimedia.org/wiki/File:Atomic_force_microscope_block_diagram.svg (visited on 02/05/2021).
- [49] G. Binnig and H. Rohrer, “Scanning tunneling microscopy,” *Surface Science*, vol. 126, no. 1, pp. 236–244, Mar. 1983, Publisher: North-Holland. DOI: 10.1016/0039-6028(83)90716-1.
- [50] G. Binnig, C. F. Quate, and C. Gerber, “Atomic force microscope,” *Physical Review Letters*, vol. 56, no. 9, pp. 930–933, Mar. 1986, Publisher: American Physical Society. DOI: 10.1103/PhysRevLett.56.930.
- [51] E. Meyer, H. J. Hug, and R. Bennewitz, *Scanning Probe Microscopy* (Advanced Texts in Physics). Berlin, Heidelberg: Springer Berlin Heidelberg, 2004. DOI: 10.1007/978-3-662-09801-1.
- [52] P. Güthner and K. Dransfeld, “Local poling of ferroelectric polymers by scanning force microscopy,” *Applied Physics Letters*, vol. 61, no. 9, pp. 1137–1139, Aug. 1992, Publisher: American Institute of PhysicsAIP. DOI: 10.1063/1.107693.

- [53] M. P. Murrell *et al.*, “Spatially resolved electrical measurements of SiO₂ gate oxides using atomic force microscopy,” *Applied Physics Letters*, vol. 62, no. 7, pp. 786–788, Feb. 15, 1993. DOI: 10.1063/1.108579.
- [54] Tertib64, *Piezoresponse of parallel and antiparallel domains*, Publication Title: Wikimedia Commons, Nov. 2009. [Online]. Available: https://commons.wikimedia.org/wiki/File:Piezoresponse_of_parallel_and_antiparallel_domains.png (visited on 02/05/2021).
- [55] N. Balke, I. Bdikin, S. V. Kalinin, and A. L. Kholkin, “Electromechanical imaging and spectroscopy of ferroelectric and piezoelectric materials: State of the art and prospects for the future,” *Journal of the American Ceramic Society*, vol. 92, no. 8, pp. 1629–1647, 2009. DOI: 10.1111/j.1551-2916.2009.03240.x.
- [56] S. V. Kalinin and D. A. Bonnell, “Imaging mechanism of piezoresponse force microscopy of ferroelectric surfaces,” *Physical Review B - Condensed Matter and Materials Physics*, vol. 65, no. 12, pp. 1–11, Mar. 2002, Publisher: American Physical Society. DOI: 10.1103/PhysRevB.65.125408.
- [57] S. V. Kalinin, A. Rar, and S. Jesse, “A decade of piezoresponse force microscopy: Progress, challenges, and opportunities,” *IEEE Transactions on Ultrasonics, Ferroelectrics, and Frequency Control*, vol. 53, no. 12, pp. 2226–2251, Dec. 2006. DOI: 10.1109/TUFFC.2006.169.
- [58] S. V. Kalinin *et al.*, “Vector piezoresponse force microscopy,” *Microscopy and Microanalysis*, vol. 12, no. 3, pp. 206–220, Jun. 2006. DOI: 10.1017/S1431927606060156.
- [59] M. Kratzer, M. Lasnik, S. Röhrig, C. Teichert, and M. Deluca, “Reconstruction of the domain orientation distribution function of polycrystalline PZT ceramics using vector piezoresponse force microscopy,” *Scientific Reports*, vol. 8, no. 1, p. 422, Jan. 11, 2018, Number: 1 Publisher: Nature Publishing Group. DOI: 10.1038/s41598-017-18843-4.
- [60] D. Seol, B. Kim, and Y. Kim, “Non-piezoelectric effects in piezoresponse force microscopy,” *Current Applied Physics*, Oxide Heterostructure Research in Korea, vol. 17, no. 5, pp. 661–674, May 1, 2017. DOI: 10.1016/j.cap.2016.12.012.
- [61] E. Soergel, “Piezoresponse force microscopy (PFM),” *Journal of Physics D: Applied Physics*, vol. 44, no. 46, p. 464003, Nov. 2011, Publisher: IOP Publishing. DOI: 10.1088/0022-3727/44/46/464003.
- [62] C. Harnagea, M. Alexe, D. Hesse, and A. Pignolet, “Contact resonances in voltage-modulated force microscopy,” *Applied Physics Letters*, vol. 83, no. 2, pp. 338–340, Jul. 14, 2003. DOI: 10.1063/1.1592307.
- [63] C. Harnagea, A. Pignolet, M. Alexe, and D. Hesse, “Higher-order electromechanical response of thin films by contact resonance piezoresponse force microscopy,” *IEEE Transactions on Ultrasonics, Ferroelectrics, and Frequency Control*, vol. 53, no. 12, pp. 2309–2322, Dec. 2006, Conference Name: IEEE Transactions on Ultrasonics, Ferroelectrics, and Frequency Control. DOI: 10.1109/TUFFC.2006.179.

- [64] S. Jesse, B. Mirman, and S. V. Kalinin, “Resonance enhancement in piezoresponse force microscopy: Mapping electromechanical activity, contact stiffness, and Q factor,” *Applied Physics Letters*, vol. 89, no. 2, p. 022 906, Jul. 2006, Publisher: American Institute of PhysicsAIP. DOI: 10.1063/1.2221496.
- [65] R. García and R. Pérez, “Dynamic atomic force microscopy methods,” *Surface Science Reports*, vol. 47, no. 6, pp. 197–301, Sep. 2002, Publisher: Elsevier. DOI: 10.1016/s0167-5729(02)00077-8.
- [66] S. Hong, “Single frequency vertical piezoresponse force microscopy,” *Journal of Applied Physics*, vol. 129, no. 5, p. 051 101, Feb. 2, 2021. DOI: 10.1063/5.0038744.
- [67] B. J. Rodriguez, C. Callahan, S. V. Kalinin, and R. Proksch, “Dual-frequency resonance-tracking atomic force microscopy,” *Nanotechnology*, vol. 18, no. 47, p. 475 504, Oct. 2007, Publisher: IOP Publishing. DOI: 10.1088/0957-4484/18/47/475504.
- [68] I. Spasojevic, A. Verdaguer, G. Catalan, and N. Domingo, “Effect of humidity on the writing speed and domain wall dynamics of ferroelectric domains,” *Advanced Electronic Materials*, vol. 8, no. 6, p. 2 100 650, 2022. DOI: 10.1002/aelm.202100650.
- [69] R. K. Vasudevan, N. Balke, P. Maksymovych, S. Jesse, and S. V. Kalinin, “Ferroelectric or non-ferroelectric: Why so many materials exhibit “ferroelectricity” on the nanoscale,” *Applied Physics Reviews*, vol. 4, no. 2, p. 021 302, Jun. 2017, Publisher: American Institute of Physics. DOI: 10.1063/1.4979015.
- [70] S. Jesse, A. P. Baddorf, and S. V. Kalinin, “Switching spectroscopy piezoresponse force microscopy of ferroelectric materials,” *Applied Physics Letters*, vol. 88, no. 6, p. 062 908, Feb. 6, 2006, Publisher: American Institute of Physics. DOI: 10.1063/1.2172216.
- [71] P. Bintachitt, S. Trolrier-McKinstry, K. Seal, S. Jesse, and S. V. Kalinin, “Switching spectroscopy piezoresponse force microscopy of polycrystalline capacitor structures,” *Applied Physics Letters*, vol. 94, no. 4, p. 042 906, Jan. 26, 2009, Publisher: American Institute of Physics. DOI: 10.1063/1.3070543.
- [72] N. Balke *et al.*, “Decoupling electrochemical reaction and diffusion processes in ionically-conductive solids on the nanometer scale,” *ACS Nano*, vol. 4, no. 12, pp. 7349–7357, Dec. 28, 2010. DOI: 10.1021/nn101502x.
- [73] C. Maier, “Synthesis and characterization of perovskite relaxor materials,” Master’s thesis, Graz University of Technology, Mar. 4, 2022.
- [74] “Metallographic oxide polishing suspensions — struers.com.” (), [Online]. Available: <https://www.struers.com/en/Products/Grinding-and-Polishing/Grinding-and-polishing-consumables/Oxide-Polishing#> (visited on 05/10/2023).
- [75] M. Lasnik, “Determination of the orientation distribution function of PZT ceramics by Piezoresponse Force Microscopy,” Diploma Thesis, Montanuniversity Leoben, 2016.
- [76] Asylum Research, *Imaging and spectroscopy applications guide - version 13, revision: 1578*, Aug. 29, 2013. [Online]. Available: <https://smif.pratt.duke.edu/sites/smif.pratt.duke.edu/files/operating/ARApplicationsGuide.pdf>.

- [77] A. Gruverman, M. Alexe, and D. Meier, “Piezoresponse force microscopy and nanoferroic phenomena,” *Nature Communications*, vol. 10, no. 1, p. 1661, Apr. 10, 2019, Number: 1 Publisher: Nature Publishing Group. DOI: 10.1038/s41467-019-09650-8.
- [78] D. Nečas and P. Klapetek, “Gwyddion: An open-source software for SPM data analysis,” *Central European Journal of Physics*, vol. 10, no. 1, pp. 181–188, Feb. 1, 2012. DOI: 10.2478/s11534-011-0096-2.
- [79] G. Van Rossum and F. L. Drake Jr, *Python tutorial*. Centrum voor Wiskunde en Informatica Amsterdam, The Netherlands, 1995.
- [80] RStudio Team, *RStudio: Integrated Development Environment for R*. Boston, MA: RStudio, Inc., 2015. [Online]. Available: <http://www.rstudio.com/>.
- [81] C. R. Harris *et al.*, “Array programming with NumPy,” *Nature*, vol. 585, no. 7825, pp. 357–362, Sep. 2020, Publisher: Springer Science and Business Media LLC. DOI: 10.1038/s41586-020-2649-2.
- [82] S. Jesse, H. N. Lee, and S. V. Kalinin, “Quantitative mapping of switching behavior in piezoresponse force microscopy,” *Review of Scientific Instruments*, vol. 77, no. 7, p. 073 702, Jul. 2006, Publisher: American Institute of Physics. DOI: 10.1063/1.2214699.
- [83] S. A. Glantz, B. K. Slinker, and T. B. Neilands, *Primer of applied regression & analysis of variance*, Third edition. New York: McGraw-Hill Education, 2016, 1183 pp., ISBN: 978-0-07-182411-8.
- [84] P. Virtanen *et al.*, “SciPy 1.0: Fundamental algorithms for scientific computing in Python,” *Nature Methods*, vol. 17, pp. 261–272, 2020. DOI: 10.1038/s41592-019-0686-2.
- [85] P. Potnis, N.-T. Tsou, and J. Huber, “A review of domain modelling and domain imaging techniques in ferroelectric crystals,” *Materials*, vol. 4, no. 2, pp. 417–447, Feb. 16, 2011. DOI: 10.3390/ma4020417.
- [86] F. Peter, A. Rüdiger, and R. Waser, “Mechanical crosstalk between vertical and lateral piezoresponse force microscopy,” *Review of Scientific Instruments*, vol. 77, no. 3, p. 036 103, Mar. 2006. DOI: 10.1063/1.2176081.
- [87] D. Alikin, L. Gimadeeva, A. Ankudinov, Q. Hu, V. Shur, and A. Kholkin, “In-plane polarization contribution to the vertical piezoresponse force microscopy signal mediated by the cantilever “buckling”,” *Applied Surface Science*, vol. 543, p. 148 808, Mar. 2021. DOI: 10.1016/j.apsusc.2020.148808.
- [88] A. S. Abramov, L. V. Gimadeeva, D. O. Alikin, Q. Hu, X. Wei, and V. Y. Shur, “Local polarization reversal in barium titanate single crystals and ceramics,” *Ferroelectrics*, vol. 574, no. 1, pp. 1–7, Apr. 4, 2021. DOI: 10.1080/00150193.2021.1888042.
- [89] B. Bhatia, J. Karthik, D. G. Cahill, L. W. Martin, and W. P. King, “High-temperature piezoresponse force microscopy,” *Applied Physics Letters*, vol. 99, no. 17, p. 173 103, Oct. 24, 2011, Publisher: American Institute of Physics. DOI: 10.1063/1.3652771.
- [90] T. Yamada, H. Iwasaki, and N. Niizeki, “Piezoelectric and elastic properties of LiTaO₃ : Temperature characteristics,” *Japanese Journal of Applied Physics*, vol. 8, no. 9, p. 1127, Sep. 1, 1969. DOI: 10.1143/JJAP.8.1127.

- [91] V. Buscaglia *et al.*, “Average and local atomic-scale structure in $\text{BaZr}_x\text{Ti}_{1-x}\text{O}_3$ ($x = 0.10, 0.20, 0.40$) ceramics by high-energy x-ray diffraction and raman spectroscopy,” *Journal of Physics: Condensed Matter*, vol. 26, no. 6, p. 065 901, Jan. 2014, Publisher: IOP Publishing. DOI: 10.1088/0953-8984/26/6/065901.
- [92] M. Deluca *et al.*, “Investigation of the composition-dependent properties of $\text{BaTi}_{1-x}\text{Zr}_x\text{O}_3$ ceramics prepared by the modified pechini method,” *Journal of the European Ceramic Society*, vol. 32, no. 13, pp. 3551–3566, Oct. 1, 2012. DOI: 10.1016/j.jeurceramsoc.2012.05.007.
- [93] S. Kim, D. Seol, X. Lu, M. Alexe, and Y. Kim, “Electrostatic-free piezoresponse force microscopy,” *Scientific Reports*, vol. 7, no. 1, p. 41 657, Jan. 31, 2017, Number: 1 Publisher: Nature Publishing Group. DOI: 10.1038/srep41657.
- [94] A. Labuda and R. Proksch, “Quantitative measurements of electromechanical response with a combined optical beam and interferometric atomic force microscope,” *Applied Physics Letters*, vol. 106, no. 25, p. 253 103, Jun. 22, 2015. DOI: 10.1063/1.4922210.
- [95] L. Collins, Y. Liu, O. S. Ovchinnikova, and R. Proksch, “Quantitative electromechanical atomic force microscopy,” *ACS Nano*, vol. 13, no. 7, pp. 8055–8066, Jul. 23, 2019, Publisher: American Chemical Society. DOI: 10.1021/acsnano.9b02883.
- [96] V. V. Shvartsman and D. C. Lupascu, “Lead-free relaxor ferroelectrics,” *Journal of the American Ceramic Society*, vol. 95, no. 1, pp. 1–26, 2012. DOI: 10.1111/j.1551-2916.2011.04952.x.
- [97] X. Leng, H. Zeng, X. Li, Y. He, K. Zhao, and W. Wang, “Unusual piezoresponse behavior across the grain boundary of $\text{PbMg}_{1/3}\text{Nb}_{2/3}\text{O}_3-0.33\text{PbTiO}_3$ thin films,” *Applied Surface Science*, vol. 257, no. 18, pp. 8085–8088, Jul. 2011. DOI: 10.1016/j.apsusc.2011.04.109.
- [98] Kell, R.C. and Hellicar, N.J., “Structural transitions in barium titanate-zirconate transducer materials,” *Acta Acustica united with Acustica*, vol. 6, no. 2, pp. 235–245(11), Jan. 1, 1956.
- [99] A. N. Salak, V. V. Shvartsman, M. P. Seabra, A. L. Kholkin, and V. M. Ferreira, “Ferroelectric-to-relaxor transition behaviour of BaTiO_3 ceramics doped with $\text{La}(\text{Mg}_{1/2}\text{Ti}_{1/2})\text{O}_3$,” *Journal of Physics: Condensed Matter*, vol. 16, no. 16, pp. 2785–2794, Apr. 28, 2004. DOI: 10.1088/0953-8984/16/16/003.
- [100] T. Dechakupt, J. Tangsritrakul, P. Ketsuwan, and R. Yimnirun, “Microstructure and electrical properties of niobium doped barium titanate ceramics,” *Ferroelectrics*, vol. 415, no. 1, pp. 141–148, Jan. 2011. DOI: 10.1080/00150193.2011.577386.
- [101] R. Zhang, J. F. Li, and D. Viehland, “Effect of aliovalent substituents on the ferroelectric properties of modified barium titanate ceramics - relaxor ferroelectric behavior,” *Journal of the American Ceramic Society*, vol. 87, no. 5, pp. 864–870, May 2004. DOI: 10.1111/j.1551-2916.2004.00864.x.
- [102] J. Nowotny and M. Rekas, “Defect structure, electrical properties and transport in barium titanate. VII. chemical diffusion in Nb-doped BaTiO_3 ,” *Ceramics International*, vol. 20, no. 4, pp. 265–275, Jan. 1994. DOI: 10.1016/0272-8842(94)90061-2.

- [103] E. Brzozowski, M. Castro, C. Foschini, and B. Stojanovic, “Secondary phases in Nb-doped BaTiO₃ ceramics,” *Ceramics International*, vol. 28, no. 7, pp. 773–777, Jan. 2002. DOI: 10.1016/S0272-8842(02)00042-1.
- [104] V. K. Veerapandiyan *et al.*, “B-site vacancy induced raman scattering in BaTiO₃-based ferroelectric ceramics,” *Journal of the European Ceramic Society*, vol. 40, no. 13, pp. 4684–4688, Oct. 1, 2020. DOI: 10.1016/j.jeurceramsoc.2020.05.051.
- [105] M. Vijatović Petrović *et al.*, “Donor–acceptor joint effect in barium titanate systems,” *Ceramics International*, vol. 41, no. 9, pp. 11 365–11 371, Nov. 2015. DOI: 10.1016/j.ceramint.2015.05.096.
- [106] F. Mayer, M. N. Popov, P. Ondrejko, J. Hlinka, J. Spitaler, and M. Deluca, “Finite-temperature investigation of homovalent and heterovalent substituted BaTiO₃ from first principles,” *Physical Review B*, vol. 106, no. 22, p. 224 109, Dec. 23, 2022. DOI: 10.1103/PhysRevB.106.224109.
- [107] T. Yamada *et al.*, “Charge screening strategy for domain pattern control in nano-scale ferroelectric systems,” *Scientific Reports*, vol. 7, no. 1, p. 5236, Jul. 12, 2017. DOI: 10.1038/s41598-017-05475-x.
- [108] A. Bencan *et al.*, “Atomic scale symmetry and polar nanoclusters in the paraelectric phase of ferroelectric materials,” *Nature Communications*, vol. 12, no. 1, p. 3509, Jun. 9, 2021. DOI: 10.1038/s41467-021-23600-3.
- [109] G. E. Karniadakis, I. G. Kevrekidis, L. Lu, P. Perdikaris, S. Wang, and L. Yang, “Physics-informed machine learning,” *Nature Reviews Physics*, vol. 3, no. 6, pp. 422–440, May 24, 2021. DOI: 10.1038/s42254-021-00314-5.
- [110] Y. Liu, K. P. Kelley, R. K. Vasudevan, H. Funakubo, M. A. Ziatdinov, and S. V. Kalinin, “Experimental discovery of structure–property relationships in ferroelectric materials via active learning,” *Nature Machine Intelligence*, vol. 4, no. 4, pp. 341–350, Apr. 4, 2022. DOI: 10.1038/s42256-022-00460-0.